University of Cincinnati

Date: 6/26/2019

I, Kris G Alavattam, hereby submit this original work as part of the requirements for the degree of Doctor of Philosophy in Cancer and Cell Biology.

It is entitled:

Epigenetic regulation of the sex chromosomes and 3D chromatin organization in male germ cells

Student's name: **Kris G Alavattam**

This work and its defense approved by:

Committee chair: Satoshi Namekawa, Ph.D.

Committee member: Paul Andreassen, Ph.D.

Committee member: Artem Barski, Ph.D.

Committee member: Chunying Du, Ph.D.

Committee member: Carolyn Price, Ph.D.

33142

Epigenetic regulation of the sex chromosomes and 3D chromatin organization in male germ cells

A dissertation submitted to
the Graduate School of the University of Cincinnati
in partial fulfillment of the requirements to the degree of

Doctor of Philosophy (Ph.D.)

in the Department of Cancer Biology
of the College of Medicine
July 2019

by

Kris G. Alavattam

B.Sc. Kettering College, 2013

Dissertation Committee:
Satoshi H. Namekawa, Ph.D. (Committee Chair)
Paul R. Andreassen, Ph.D.
Artem Barski, Ph.D.
Chunying Du, Ph.D.
Carolyn Price, Ph.D.

Abstract

Germ cell development is a remarkable story. Developing germ cells undergo large-scale, dynamic programs of gene expression that are essential for fertility, unlike any found in somatic cells. The rewiring of transcription networks takes place when germ cells enter meiosis, a critical period for preparing the gamete genome and the acquisition of totipotency following fertilization. In meiosis, it is thought that dynamic forms of germline chromatin organization support diverse forms of epigenetic programming and gene regulation, yet it is poorly understood how the spatiotemporal organization of germ cell chromatin facilitates the epigenomes and transcriptomes necessary for the next generation of life.

To address this, I undertook two major research projects: The first seeks to understand the molecular mechanisms of meiotic sex chromosome inactivation, an essential event in male germ cell development, through genetic analyses of a protein network that directs epigenetic regulation of the sex chromosomes. The second project employs Next-Generation Sequencing technologies to understand how the spatiotemporal organization of male germ cell chromatin facilitates and relates to vitally important transcriptomes and epigenomes.

In the first project, first published in 2016 (PMID: 27760317), I and a small team analyze meiosis in eight mouse models deficient for various DNA damage response (DDR) factors, including Fanconi anemia (FA) proteins. We reveal a network of FA and DDR proteins in which FA core factors FANCA, FANCB, and FANCC are essential for FANCD2 foci formation, whereas BRCA1 (FANCS), MDC1, and RNF8 are required for BRCA2 (FANCD1) and SLX4 (FANCP) accumulation on the sex chromosomes during meiosis. Furthermore, FA proteins modulate distinct histone marks on the sex chromosomes. Our data suggest that RNF8 integrates the FA-BRCA pathway. We reveal distinct functions for FA proteins and illuminate the male sex chromosomes as a model to dissect the function of the FA-BRCA pathway.

In the second project, first published in 2019 (PMID: 30778237), our team performs Hi-C analyses to examine 3D chromatin organization in male germ cells. We show that the highly compartmentalized 3D chromatin organization characteristic of interphase nuclei is attenuated in meiotic prophase I. Meiotic prophase I is predominated by short-range intrachromosomal interactions that represent a condensed form akin to that of mitotic chromosomes. Unlike mitotic chromosomes, meiotic chromosomes display weak genomic compartmentalization, weak topologically associating domains, and localized point interactions. Genomic compartmentalization increases in sperm development. The X chromosome lacks domain organization during meiotic sex chromosome inactivation. We propose that male meiosis occurs amid the global reprogramming of 3D chromatin organization and that strengthening of chromatin compartmentalization takes place in spermiogenesis to prepare the next generation of life.

Our Hi-C study was published amid two related manuscripts on the functional significance of chromatin organization in male germ cells; I conclude with a discussion of findings, both overlapping and distinct, from these three reports. Also, in considering the mechanistic relationships between DDR pathways and the high-order chromatin organization of the sex chromosomes, I integrate and reflect on findings from my two projects. I consider all of these studies and put forward ideas and questions.

Preface

The work presented in this dissertation is published in the following peer-reviewed publications:

> Elucidation of the Fanconi anemia protein network in meiosis and its function in the regulation of histone modifications.
>
> **Kris G. Alavattam**, Yasuko Kato, Ho-Su Sin, So Maezawa, Ian J. Kowalski, Fan Zhang, Qishen Pang, Paul R. Andreassen, and Satoshi H. Namekawa.
>
> *Cell Rep*. 2016 Oct 18;17(4):1141-1157.
>
> doi: 10.1016/j.celrep.2016.09.073
>
> PMID: 27760317; see reference[1].

> Attenuated chromatin compartmentalization in meiosis and its maturation in sperm development.
>
> **Kris G. Alavattam**, So Maezawa, Akihiko Sakashita, Haia Khoury, Artem Barski, Noam Kaplan, and Satoshi H. Namekawa.
>
> *Nat Struct Mol Biol*. 2019 Mar;26(3):175-184.
>
> doi: 10.1038/s41594-019-0189-y
>
> PMID: 30778237; see reference[2].

Acknowledgments

To some specific and special people who have lived through a long and often terrible situation: Here’s to making it through and still loving life, even though it can be baffling and sad. Our stories aren’t over; here’s to new chapters. (This dissertation caps one of mine.)

And to some of us who didn’t get new chapters, I remember you and, actually, I can’t forget you. You made an impression in ways you didn’t know.

Table of Contents

Chapter 1

Chapter 2

Chapter 3

Chapter 4

Chapter 1

Male germ cell development and epigenetics: A multifaceted story

Kris G. Alavattam[1,2,3]

[1]Graduate Program in Cancer and Cell Biology, Department of Cancer Biology, University of Cincinnati College of Medicine, Cincinnati, OH, USA

[2]Division of Reproductive Sciences, Division of Developmental Biology, Perinatal Institute, Cincinnati Children's Hospital Medical Center, Cincinnati, OH, USA

[3]Department of Pediatrics, University of Cincinnati College of Medicine, Cincinnati, OH, USA

Introduction

Germ cell development is a remarkable, multifaceted story. Developing germ cells undergo large-scale, dynamic, and protracted programs of gene expression that are essential for fertility—and unlike any found in somatic cells[3-6]. The rewiring of transcription networks results from—and influences—epigenetic programming, which is, in turn, critical for the acquisition of totipotency following fertilization[4,5,7-11]. Dynamic forms of chromatin organization in the germline support diverse forms of gene regulation and epigenetic programming—but how? There is a rift in our collective knowledge of mammalian gametogenesis: How does the spatiotemporal organization of germ cell chromatin facilitate the gene expression programs and epigenetic states necessary for the next generation of life?

Research Overview

To answer this question, I embarked on two projects over the course of my graduate training in the lab of Satoshi Namekawa. Both projects used mice as model organisms. The first sought to understand the molecular mechanisms of "meiotic sex chromosome inactivation" (MSCI), an essential event in male germ cells and, thus, the propagation of life, through genetic analyses of a protein network that directs epigenetic regulation of the X and Y chromosomes. The second project employed Next-Generation Sequencing technologies, including high-throughput chromosome conformation capture (Hi-C), to understand how the spatiotemporal organization of male germ cell chromatin facilitates and otherwise relates to gene expression programs and epigenetic states—which are essential to the function of male germ cells and, following fertilization, embryogenesis[4,5,7-18].

The results of these research projects have been published in two manuscripts, one in *Cell Reports* (October, 2016)[1] and the other in *Nature Structural and Molecular Biology* (March, 2019)[2]. In this dissertation, I include versions of these two studies that have been edited for grammar, style, and format. The 2016 publication comprises **Chapter 2**, and the 2019 publication comprises **Chapter 3**. In **Chapter 4**, I conclude the dissertation with an essay that contextualizes the findings from **Chapter 3** amid two closely related publications on the functional significance of higher-order chromatin organization in male germ cells[19,20]. Then, I ruminate on several findings from these studies and, in considering the relationship between MSCI and higher-order chromatin organization, I attempt to integrate findings from **Chapter 2** and **Chapter 3**. In attempting to establish a foundation for future research, I reflect on the ideas and questions these studies evoke.

To frame and contextualize the stories told in these chapters, the remainder of **Chapter 1** expands on subjects foundational to the upcoming research. These subjects are (1) a combined overview of fertilization, epigenetics, and the transmission of epigenetic information from parental gametes to offspring; (2) the development of germ cells and spermatogenesis; (3) a DNA damage response checkpoint in meiosis; and (4) epigenetic programming, transcription, and chromatin organization in late spermatogenesis.

Fertilization and epigenetics. Fertilization is a hallmark of sexual reproduction, when the genetic information from two differentiated, sexually heteromorphic gametes combines to form a zygote. Being totipotent, this zygote is capable of developing into all of the cells of an offspring organism[21]. However, in addition to genetic information, it is strongly suspected that another form of nuclear information is transmitted from parental gametes to offspring: epigenetic information. Epigenetic information is, in brief, information encoded not by genomic DNA but instead by chemical modifications upon the DNA; what's more, these chemical modifications extend beyond DNA to the proteins in complex with the DNA, which together comprise a polymer termed "chromatin;" an important consideration—still the subject of some debate—is that these modifications are maintained through DNA replications and cell divisions[22-26]. Taking into account their presumed effects, the transmission of epigenetic information is often categorized in two ways: (1)

“transgenerational” or (2) “parental” or “intergenerational;” a recent review parses the two categories[27]:

> Transgenerational effects refer exclusively to phenomena that could not be ascribed to direct effects of a particular trigger on the affected organism. For instance, an environmental stimulus can directly affect a gestating embryo (and the already-formed oocytes within a female embryo in mammals[24,28]). As such, only altered phenotypes occurring in the second (in the case of male transmission) or third (in the case of female transmission) generation after a trigger can truly be described as transgenerational inheritance. Effects spanning shorter timescales are described as parental or intergenerational.

More specifically, epigenetic information includes (1) the methylation of cytosine nucleotides; (2) the composition and (3) post-translational modifications of proteins called histones, which package DNA into variously open or compact configurations; and (4) the storage and transmission of RNA molecules of various lengths and compositions, often complexed with chromatin.

In mammals, a host of epidemiological, environmental, nutritional, and toxicant studies suggest that epigenetic alterations to germ cells condition progeny over multiple generations[18,28,29]. But empirical support for causative means—i.e., supporting mechanisms—are tenuous. The mechanisms underlying the transmission of epigenetic information, while defined in a number of specific instances[26,30-39], are not well understood. Moreover, the functional significance of heritable epigenetic information is otherwise undefined or unclear. Put succinctly, it is largely unknown how and to what extent epigenetic information inherited from parents directs the development of offspring and/or regulates the phenotypic traits of progeny.

In early embryonic development, cell fate changes are concomitant with the translation and degradation of RNA transcripts provided by the maternal gamete, as well as the initiation of embryonic transcription in a process termed “zygotic genome activation”[40,41]. As well, chromatin states, including histone post-translational modifications and DNA methylation, inherited from the paternal and maternal germlines undergo a form of “epigenetic reprogramming,” wherein epigenetic modifications are reestablished and/or otherwise altered to promote an embryonic chromatin state distinct from those of the gametic forebears[42,43]. These early embryonic events are vital for the establishment of totipotency, post-implantation development, and the overall fitness of offspring. However, the extent and relevance of epigenetic inheritance versus early embryonic reprogramming events, along with their underlying molecular mechanisms, are not well understood.

Nonetheless, there is mounting evidence that embryogenesis is affected by the transmission of altered and/or improper parental chromatin states. For example, in mice, the maternal transmission of a histone H3 post-translational modification associated with the dense compaction of chromatin, trimethylation of lysine 9 (H3K9me3), defines the organization of maternally derived centromeres in early embryonic development[44]. Likewise, the proper deposition of another histone H3 post-translational modification, trimethylation of lysine 27 (H3K27me3), is necessary to establish a maternal chromatin state that, in the embryo, facilitates the transcriptional silencing of certain genes, including *Xist*, which encodes a long non-coding RNA vital for proper X chromosome gene dosage in X chromosome inactivation[45,46].

The inheritance of a proper paternal chromatin state is of vital importance too. For example, an improper paternal chromatin state has been shown to inhibit embryogenesis resulting from assisted reproduction technologies: In humans and mice, female gametes fertilized with spermatids—sperm precursor cells that contain far more histones than sperm—significantly reduced the success rates for pregnancy and embryonic and/or fetal development[47,48]. These studies reveal the importance of chromatin remodeling during the later stages of spermatogenesis, indicating that the paternal transmission of immature or improper chromatin states has negative effects on embryonic or fetal development. Studies of misprogrammed paternal chromatin have revealed not only development defects but far-reaching effects[12,14,17,18,49], both intergenerational and transgenerational, including an inherited susceptibility to cancer[49]: In male mice, the genetic loss of *Kdm6a*, an X chromosome-linked lysine demethylase, altered the distribution of H3K27me3 in sperm; the transmission of this improperly programmed—or "epimutated"—genome to offspring appeared to make certain portions of the genome more sensitive to further epigenetic changes; ultimately, the offspring evinced increased cancer susceptibility, even though they inherited an X chromosome bearing an intact *Kdm6a* from their mothers. In another example[18], the overexpression of *Kdm1a*, a lysine demethylase that acts on trimethylation of lysine 4 (H3K4me3), resulted in the redistribution of H3K4me3 in sperm, which impaired the development and survivability of the next generation; these defects persisted to the next generation in the absence of *Kdm1a* germline expression, implicating the improper distribution of methylated histones in an apparent transgenerational epigenetic effect.

The development of germ cells and spermatogenesis. The development of germ cells begins in embryos. In mice, precursors to male and female gametes are specified as early as day ~6-6.5 of embryonic development (E6-6.5) in the epiblast, where they comprise a small group of cells[50,51]. These precursor germ cells, termed "primordial germ cells" (PGCs), number ~40–50 when they begin to proliferate and migrate to the primitive gonads. By the time they arrive, at E10.5, the PGCs have undergone numerous divisions—having come to number ~3,000—as well as extensive epigenetic reprogramming[52]. In the primitive gonads, the PGCs continue to proliferate as the gonads differentiate into either primitive ovaries or testes[53]. By E13.5, the PGCs number ~25,000 and, depending on the sex of the organism, proceed to enter into markedly different developmental pathways. In brief, the female-specific pathway sees germ cells enter into meiosis, while male germ cells, now termed prospermatogonia, enter into a state of arrest.

Shortly after birth, prospermatogonia exit their arrested state and proliferate to populate the testes with germ cells, including a minutely small population of spermatogonial stem cells as well as spermatogonia in various states of differentiation. (It is important to note that, while this event takes place shortly after birth in male mice, the timing is different in many other mammals;

for example, in humans, the mitotic arrest persists until puberty.) For the remaining life of male mice, groups of spermatogonia undergo ~10 mitotic divisions followed by an additional round of DNA replication prior to entering meiosis. Meiosis is a special cell division process that sees these germ cells—now termed spermatocytes and containing two complements of the diploid genome—undergo homologous recombination between maternal and paternal alleles. The first phase of meiosis, prophase I, is the longest, at nearly two weeks in duration, and is quickly followed by two meiotic divisions that result in four haploid round spermatids, each genetically distinct from each other and the parent spermatocyte. These spermatids differentiate into sperm in another lengthy development period called spermiogenesis. In mice, the duration of spermatogenesis, from spermatogonial stem cell to mature sperm, takes ~34.5 days.

The meiotic DNA damage response checkpoint. Meiotic prophase I marks the beginning of what is termed "late spermatogenesis," and it is, in its own way, a remarkable time in the life of germ cells. For one, spermatocytes undergo programmed induction of DNA double-strand breaks (DSBs) to stimulate repair via homologous recombination[54]. DSBs are formed through the activity of SPO11, a topoisomerase II-like enzyme; this activity is essential for homologous recombination repair, which promotes the proper pairing of homologous chromosomes and the shuffling of genetic material between maternal and paternal alleles, a systematized fostering of genetic diversity in offspring that is a hallmark of sexual reproduction[55,56]. A small number of homologous recombination repair events results in genetic crossovers that, at the first meiotic division, ensure the proper segregation of homologs to daughter cells. In mice, ~200–300 DSBs are generated in prophase I, and these must undergo efficient repair to ensure the proper genome-wide distribution and frequency of crossovers[54-57]. Failure to repair DSBs in a timely or otherwise efficient manner activates checkpoint mechanisms that trigger the developmental arrest and death of spermatocytes[58,59]. In another form of genetic quality control, homologous chromosomes must properly pair and synapse prior to the first meiotic division, lest the improper pairing and synapsis trigger spermatocyte arrest and death too[59-61]. Together, these phenomena comprise a greater "meiotic checkpoint"—also called the "pachytene checkpoint," so named for the substage of prophase I in which it is commonly observed.

Because the sex chromosomes in pachytene spermatocytes undergo MSCI, their regulation is distinct from that of autosomes, albeit no less essential to the meiotic checkpoint. In normal prophase I, MSCI sees the X and Y chromosomes undergo transcriptional silencing prior to their sequestration away from recombining, transcriptionally active autosomes, compartmentalized in a nuclear body termed the "XY body" (also known as the "sex body"). MSCI, which is essential to the viability of germ cells and thus male fertility[62-66], induces the epigenetic programming and chromatin remodeling of the sex chromosomes, including the deposition of various repressive and active histone post-translational modifications as well as other modifications to chromatin[3,67-75]. Unlike X chromosome inactivation in females, which hinges on the activity of *Xist* non-coding RNA, MSCI is directed by DNA damage response (DDR) signaling[64], which catalyzes the phosphorylation of histone variant H2AX (γH2AX). The establishment of MSCI requires γH2AX to spread through the combined chromatin domain of the X and Y chromosomes[62,63]. This spreading is directed by MDC1, a DDR factor and γH2AX-binding partner, as part of an expansive feed-forward mechanism[63]. Other DDR factors, including BRCA1 and ATR, are implicated in the initiation of MSCI and its subsequent feed-forward mechanism[64,76].

However, it was unknown whether a DDR protein network functions in concert, as it does in somatic DDR signaling, to govern the X and Y chromosomes in meiosis. We inferred that this is the case for several reasons. For one, MSCI is sensitive to DNA damage and/or altered DSB-processing on the autosomes[60,77]; this, in turn, triggers apoptosis associated with, presumably, the ectopic, toxic expression of Y-linked genes such as *Zfy1* and *Zfy2*[71]. As well, MSCI is considered to be a manifestation of meiotic silencing of unsynapsed chromatin (MSUC), a general mechanism for transcriptional repression in which gene expression is suppressed when homologous chromatin is not synapsed[78-81]. With this in mind, a prominent hypothesis in the field posits that certain silencing proteins, comprising, in part, a greater protein network, are available in limiting quantities such that autosomal defects draw away MSCI proteins, thereby disrupting MSCI; that, in turn, results in the ectopic expression of deleterious sex-linked genes.

The research described in **Chapter 2** reveals that a network of DDR proteins functions in the epigenetic programming of the X and Y chromosomes, including the proper, precise deposition of histone post-translational modifications associated with the repression and subsequent selective activation of sex chromosome-linked genes[1]. Our findings yield important insights into the functions of DDR pathways, lending insight into their roles in the somatic DDR. This raises the possibility that common pathways underlie both the regulation of sex chromosomes in meiosis and the somatic DDR. Thus, given that it facilitates the dissection of roles of individual nodes in protein networks, MSCI has emerged as a model system for DDR signaling and epigenetic programming, and for understanding how DDR proteins are regulated and interrelated.

Epigenetic programming in late spermatogenesis. In meiosis, the precise epigenetic programming of the sex chromosomes occurs against a backdrop of genome-wide bursts in transcription[3,69,82,83]. These bursts accompany the large-scale rewiring of germline transcription networks: During the transition from mitotic spermatogonia to meiotic spermatocytes, several thousand genes expressed in somatic cell types and spermatogenic progenitor cells undergo repression; at the same time, several thousand genes associated with late spermatogenesis are activated[3]. This gene expression program persists beyond the two meiotic divisions into the spermiogenesis phase. Another lengthy phase of mouse spermatogenesis, spermiogenesis is approximately two weeks in duration and sees haploid round spermatids remodel their chromatin structure and cellular morphology to generate highly compacted, motile sperm. In the nuclear compaction process, most histones are progressively evicted and replaced by protamines—small, highly basic proteins that are essential for the structural stabilization of sperm as well as the intranuclear stabilization of DNA. Those histones that remain—~3% in mice and ~10-15% in humans[14,84,85]—are increasingly replaced by histone variants, including variants expressed only in the testis[86-89], and/or modified with post-translational modifications.

Nucleosomes retained in mouse and human sperm are predominantly found at genomic regions characterized by a high frequency of unmethylated cytosine-guanine, or “CpG,” dinucleotides, which, in turn, are frequently located in gene promoters[14,84,85]. Furthermore, in mouse sperm, the nucleosomes associated with such CpG-rich regions contain the histone H3 in concert with various post-translational modifications, including trimethylation of H3 lysine 4 (H3K4me3), H3K27me3, or “bivalent domains” containing both modifications[85]. Bivalent domains are thought to poise embryonic gene expression after fertilization[90]; thus, in mature sperm, the retention of nucleosomes and their post-translational modifications may provide a means for the paternal transmission of epigenetic information across generations.

Indeed, as described in **Chapter 3**, we propose that the large-scale, genome-wide chromatin organization that takes place beginning in meiosis is, itself, a form of epigenetic reprogramming that facilitates spermatogenic gene expression and, later, embryonic competency. The various features of 3D chromatin organization in male germ cells corroborate features of the transition from mitotically proliferating spermatogonia to meiotic spermatocytes, including (1) the switch from a somatic/progenitor gene expression program to a late spermatogenesis gene expression program[3], (2) genome-wide changes in chromatin accessibility[82], and (3) the genome-wide establishment of bivalent domains[4,5]. Our results reveal that the paternal chromatin state is associated with unique and diverse transcriptomes. We propose that, beginning as early as meiosis, genome-wide organization, followed by the subsequent maturation of germline chromatin to a highly compartmentalized state in mature sperm, prepares the next generation of life.

Chapter 2

Elucidation of the Fanconi anemia protein network in meiosis and its function in the regulation of histone modifications

Kris G. Alavattam[1,2,3], Yasuko Kato[2,3,4], Ho-Su Sin[2,3,5], So Maezawa[2,3,6], Ian J. Kowalski[2,3,7], Fan Zhang[3,8], Qishen Pang[3,8], Paul R. Andreassen[3,8], and Satoshi H. Namekawa[2,3,9,*]

[1]Graduate Program in Cancer and Cell Biology, Department of Cancer Biology, University of Cincinnati College of Medicine, Cincinnati, OH, USA

[2]Division of Reproductive Sciences, Division of Developmental Biology, Perinatal Institute, Cincinnati Children's Hospital Medical Center, Cincinnati, OH, USA

[3]Department of Pediatrics, University of Cincinnati College of Medicine, Cincinnati, OH, USA

[4]Present address: Department of Applied Biology, Institute for the Promotion of University Strategy, Kyoto Institute of Technology, Kyoto, Japan

[5]Present address: Department of Developmental Biology and Department of Genetics, Stanford University School of Medicine, Stanford, CA, USA

[6]Present address: Department of Animal Science and Biotechnology, School of Veterinary Medicine, Azabu University, Sagamihara, Kanagawa, Japan

[7]Present address: University of Toledo College of Medicine, Toledo, OH, USA

[8]Division of Experimental Hematology and Cancer Biology, Cincinnati Children's Hospital Medical Center, Cincinnati, OH, USA

[9]This author supervised this work: Satoshi H. Namekawa

[*]Correspondence: satoshi.namekawa@cchmc.org

Published in *Cell Rep*. 2016 Oct 18;17(4):1141-1157.

https://doi:10.1016/j.celrep.2016.09.073

(See reference[1].)

Abstract

Precise epigenetic regulation of the sex chromosomes is vital for the male germline. Here, we analyze meiosis in eight mouse models deficient for various DNA damage response (DDR) factors, including Fanconi anemia (FA) proteins. We reveal a network of FA and DDR proteins in which FA core factors FANCA, FANCB, and FANCC are essential for FANCD2 foci formation, whereas BRCA1 (FANCS), MDC1, and RNF8 are required for BRCA2 (FANCD1) and SLX4 (FANCP) accumulation on the sex chromosomes during meiosis. In addition, FA proteins modulate distinct histone marks on the sex chromosomes: FA core proteins and FANCD2 regulate H3K9 methylation, while FANCD2 and RNF8 function together to regulate H3K4 methylation independently of FA core proteins. Our data suggest that RNF8 integrates the FA-BRCA pathway. Taken together, our study reveals distinct functions for FA proteins and illuminates the male sex chromosomes as a model to dissect the function of the FA-BRCA pathway.

Introduction

In meiosis, homologous chromosomes undergo synapsis and recombination to promote genetic diversity in offspring. However, in male mammals, the sex chromosomes—X and Y—have vastly different morphologies and genetic content, and are thus largely unsynapsed during meiosis. Instead, the sex chromosomes are transcriptionally silenced in a process known as "meiotic sex chromosome inactivation" (MSCI)[64,65]. In MSCI, the sex chromosomes are compartmentalized together to form an "XY body" (also known as a "sex body") and sequestered away from recombining, transcriptionally active autosomes. MSCI is initiated with the phosphorylation of histone variant H2AX at serine 139 (γH2AX)[62] and the near-simultaneous recruitment of binding partner MDC1[63], a signaling mechanism that plays a crucial role in the DNA damage response (DDR) in somatic cells[91,92]. Following the initiation of MSCI, extensive chromatin remodeling occurs on the sex chromosomes. This includes nucleosome remodeling, including H3.3 incorporation[75]; establishment of epigenetic modifications; and maintenance of chromosome-wide silencing through meiosis into post-meiotic stages[67,69,74]. Some DDR factors, such as BRCA1 and ATR, have been implicated in the initiation of MSCI[62,63,71,73,76]. However, it remains unknown whether a DDR protein network functions in concert, as it does in the somatic DDR, to govern the sex chromosomes.

Fanconi anemia (FA) is a genetic disease associated with bone marrow failure, increased cancer susceptibility, and severe germline defects. Patients are said to have FA if they are deficient for any one of a growing number of FA proteins that function in a biochemical pathway known as the FA-BRCA pathway. The FA-BRCA pathway is known to function in the resolution of a particularly harmful form of DNA damage, DNA interstrand crosslinks, in which the Watson and Crick strands become covalently linked[93,94]. At the time of this chapter's initial publication, in October of 2016, 21 FA proteins had been identified[94-98], comprising a network of proteins with distinct functions and properties. These include the FA core complex—FANCA, B, C, E, F, G, L, and M—which catalyzes the monoubiquitination of FANCD2 and FANCI in a sub-pathway termed the FA pathway[99-102]. Also included in the FA-BRCA pathway are breast cancer susceptibility proteins, such as BRCA1 (FANCS) and BRCA2 (FANCD1)[97,103,104], and SLX4 (FANCP), a scaffold for endonucleases such as XPF (FANCQ)[105,106]. It remains largely unknown how all of these diverse proteins relate to each other to function within the broad FA-BRCA pathway, and how proteins in this pathway relate to proteins in other DDR pathways. In this context, we previously demonstrated that a member of the FA core complex, FANCB, accumulates on the XY body and regulates H3K9 methylation[68]. Because of the involvement of FANCB in the regulation of the sex chromosomes[68], we reasoned that the FA-BRCA pathway may regulate the meiotic sex chromosomes too.

To evaluate the regulation of MSCI by the FA-BRCA pathway, we determined that FA proteins accumulate on the sex chromosomes in coordinated temporal and spatial arrangements, and we demonstrated that the FA pathway is activated during meiosis as shown by the monoubiquitination of FANCD2. To determine the functions of the broader FA-BRCA pathway in meiosis, and to identify epistatic relationships between different FA proteins, we systematically analyzed eight mouse models deficient for various DDR factors, including several FA proteins. Our findings reveal that a network of FA-BRCA proteins and related DDR proteins, MDC1 and RNF8, functions in the epigenetic programming of the sex chromosomes. We term this network the FA-DDR network. Our work provides several mechanistic insights into how this network is regulated. Based upon our findings, the meiotic sex chromosomes have emerged as a model that yields important insights into the functions of the FA-BRCA pathway, with important implications for its roles in the somatic DDR.

Results

Fanconi anemia proteins accumulate on the sex chromosomes in coordinated temporal and spatial arrangements. To determine the relationship of the FA pathway to the sex chromosomes during meiosis, we performed immunofluorescence microscopy of meiotic chromosome spreads, analyzing the localization of FA proteins. We judged each stage of meiotic prophase I based on the precise appearance of chromosome axes (summarized in **Supplementary Figure 2.1**). We tested various antibodies against proteins that are components of the FA core complex (**Figure 2.1a**). At the onset of the pachytene stage, MSCI and meiotic recombination are subject to distinct regulation (**Figure 2.1b**). Among the FA core proteins, we found the partial accumulation of FANCM on the axes of the sex chromosomes (termed XY axes hereafter) during meiosis (**Figure 2.1c**). FANCM, a helicase that binds single-strand DNA, is thought to be recruited to replication forks stalled by DNA interstrand crosslinks in the somatic DDR[107]. The specificity of the anti-FANCM antibody (FARF D3823) was confirmed with a competition experiment using a FANCM peptide that matches the epitope region (**Supplementary Figure 2.2**). FANCM accumulation on the sex chromosome axes begins in the early pachytene stage and spreads onto the entire domain of the X and Y chromosomes (termed "XY chromatin" hereafter) through the early diplotene stage (**Figure 2.1c**; **Supplementary Figure 2.3**). As spermatocytes progress through the remainder of prophase I, FANCM is gradually lost from the XY chromatin (**Supplementary Figure 2.3**). In accord with this finding, our previous study demonstrated that FANCB, another FA core complex protein, accumulated on the sex chromosomes beginning in the early pachytene stage[68]. Although we could not detect immunofluorescence signals for other core proteins during meiosis, our observations of FANCM and FANCB raised the possibility that the FA core complex is involved in the regulation of the sex chromosomes during meiosis.

Next, we examined the activation of the FA pathway on the sex chromosomes. In somatic cells, activation of the FA pathway is measured by core complex-mediated monoubiquitination of FANCD2 (**Figure 2.1a**), which is followed by foci formation on chromatin[99,108]. Consistent with previous reports[99,109], FANCD2 foci localized on both autosome and sex chromosome axes during meiosis (**Figure 2.1d**). During the transition from the leptotene to zygotene stages, FANCD2 foci accumulated on the synapsed axes of autosomes and gradually decreased on autosomes through the remainder of meiotic prophase I (**Figure 2.1d**, arrowheads; **2.1e**). On the other hand, we found that FANCD2 foci on the XY axes are regulated apart from those on autosomes. A small number of FANCD2 foci accumulated on the XY axes in the early pachytene stage and were amplified along the XY axes through the late pachytene stage before decreasing through the remainder of prophase I (**Figure 2.1d**, **2.1e**). Consistent with the appearance of FANCD2 foci, we detected monoubiquitinated FANCD2 by western blotting using the crude extract of wild-type mouse testes with three independent anti-FANCD2 antibodies (**Figure 2.1f**). We validated the presence of monoubiquitination by comparison with the somatic DDR. In brief, we blotted lysate from PD20 cells—a human lymphoblast cell line derived from an FA patient deficient for *FANCD2*[110]—that were reconstituted with different forms of FANCD2. Before producing the lysates, the PD20 variants were treated with hydroxyurea to induce stalled replication forks, leading to DNA damage and thus activation of the FA pathway. Monoubiquitination was observed in PD20 cells reconstituted with wild-type FANCD2 but not those that contained a non-ubiquitinable form of FANCD2, K561R (**Figure 2.1f**). Mono- and non-ubiquitinated FANCD2 bands from wild-type whole testis lysate co-migrated with those in reconstituted PD20 cells (**Figure 2.1f**). Although testes also contain cells that are not in meiosis—and since it has been demonstrated, using the K561R mutant, that monoubiquitination is required for FANCD2 foci formation in somatic cells[99]—we infer that FANCD2 is monoubiquitinated in meiosis. In support of our conclusion, a previous study also detected monoubiquitinated FANCD2 in testis lysate[111]. Together, these results suggest that the FA pathway is activated during normal meiosis, and its manifestation is distinct between autosomes and the sex chromosomes.

To further examine the involvement of FA proteins on the sex chromosomes during meiosis, we reinvestigated the localization of two additional FA proteins reported to localize on the sex chromosomes during meiosis: BRCA2 (FANCD1) and SLX4 (FANCP)[112,113]. In the somatic DDR, BRCA2 is involved in the maintenance of genome stability via the homologous recombination repair pathway for DNA double-strand break repair[114]. A previous study reported that BRCA2 is restricted to the XY axes during meiosis[112], but we found that BRCA2 localized on XY chromatin in the late pachytene stage, after progressive accumulation on the X chromatin beginning in the mid pachytene stage (**Figure 2.1g**). Although we used a different anti-BRCA2 antibody than that reported previously[112], we confirmed the specificity of our anti-BRCA2 antibody through immunoblots[115]. It is interesting that FANCD2 and BRCA2 have distinct localization patterns on the meiotic sex chromosomes, given that these proteins strongly colocalize in somatic cells exposed to exogenous DNA damage[116]. SLX4, a structure-specific endonuclease involved in the repair of various DNA lesions[94,117], also localized on the XY chromatin in the late pachytene stage, consistent with a previous study[113]. SLX4 progressively increased in intensity as it spread through the XY chromatin during the pachytene stages (**Figure 2.1h**). The coordinated spatial and temporal localization of FANCM, FANCB, FANCD2, BRCA2, and SLX4 on the XY chromatin beginning in the early and mid pachytene stages (summarized in **Figure 2.1i**; **Supplementary Figure 2.3**) suggests that the FA-BRCA pathway is activated on the sex chromosomes.

Fanconi anemia core factors are essential for FANCD2 foci on the sex chromosomes during meiosis. Next, we sought to dissect the interrelationship of FA proteins on the sex chromosomes during meiosis. To evaluate the necessity of FA core complex members (FANCA and FANCC) and FANCD2 in the recruitment of other FA proteins, we analyzed mutant mice deficient for FANCA ($Fanca^{-/-}$), FANCC ($Fancc^{-/-}$), and FANCD2 ($Fancd2^{-/-}$). The accumulation of FANCD2 foci was abolished on XY axes in *Fanca* and *Fancc* mutants (**Figure 2.2a**; **Supplementary Figure 2.4a**). Autosomal FANCD2 foci were also absent from *Fanca* and *Fancc* mutants (**Figure 2.2a**; **Supplementary Figure 2.4a**). This appears to parallel the role of the FA core complex in regulating FANCD2 recruitment to foci in somatic cells[99,108]. FANCD2 foci were absent from autosome and XY axes in meiotic cells from *Fancd2* mutants (**Figure 2.2b**), demonstrating the specificity of the antibody used.

In contrast to FANCD2, the accumulation of BRCA2 on XY chromatin was unaffected in *Fanca*, *Fancc*, and *Fancd2* mutants (**Figure 2.2c**, **2.2d**; **Supplementary Figure 2.4b**). This is distinct from a previous report in which the assembly of BRCA2 foci into DNA damage foci induced by ionizing radiation depends on FANCD2 monoubiquitination in somatic cells[116]. Furthermore, SLX4 accumulation was unaffected in *Fanca*, *Fancc*, and *Fancd2* mutants (**Figure 2.2e**, **2.2f**; **Supplementary Figure 2.4c**). These data indicate that the accumulation of BRCA2 and SLX4 on sex chromosomes in meiosis is independent of the FA core complex and FANCD2 (**Figure 2.2g**; **Supplementary Figure 2.4d**). This is in contrast to a reported finding that the FA core complex and FANCD2 regulate SLX4 in the somatic DDR[117]. It should be noted that our previous study demonstrated that FANCB is essential for FANCD2 foci formation during meiosis but is dispensable for SLX4 localization on the sex chromosomes during meiosis[68]. Therefore, the core factors FANCA, FANCB, and FANCC appear to have common functions on the sex chromosomes.

BRCA1 and MDC1 are required for the accumulation of BRCA2 and SLX4 on the sex chromosomes during meiosis. At the onset of MSCI, BRCA1 is a critical regulator of the DDR that recruits ATR [73] and establishes DDR signals along the unsynapsed axes[76]. In somatic cells, BRCA1 is functionally linked to FA proteins[99,118,119], and, indeed, *BRCA1* has been identified as an FA gene and designated *FANCS*[97]. BRCA1 is required for the recruitment of FANCD2 to DNA interstrand crosslinks and other types of DNA damage in the somatic DDR[99,119,120]. To investigate the functional relevance of BRCA1 in regulating FA proteins in meiosis, we examined mutants with *Brca1* conditional deletions established in our previous study[76]. Since deletion of *Brca1* exon 11 has an embryonic lethal phenotype, *Brca1* exon 11 was conditionally deleted (*Brca1*cKO) using the germline-specific *Ddx4*-Cre (also known as *Vasa-Cre*)[121]. FANCD2 foci were present, but not amplified, on the XY axes, and foci persisted on autosome axes while their numbers decreased in control samples (**Figure 2.3a**, **2.3b**). Thus, these data indicate a role for BRCA1 in the amplification of FANCD2 foci on the XY axes and the progressive resolution of FANCD2 foci on autosomes. On the other hand, the accumulation of BRCA2 on XY chromatin was abolished in the *Brca1*cKO (**Figure 2.3c**), consistent with the requirement of BRCA1 for BRCA2 foci formation in the somatic DDR[112,122,123]. Furthermore, in the *Brca1*cKO, accumulation of SLX4 on XY chromatin was abolished (**Figure 2.3d**), indicating that BRCA1 is required for SLX4 recruitment to XY chromatin. Although it has been reported that BRCA1 is not necessary for the recruitment of SLX4 to interstrand crosslinks in somatic cells[124], these data indicate that BRCA1 regulates SLX4 on the sex chromosomes. *Brca1*cKO spermatocytes undergo meiotic arrest at the mid pachytene stage and are eliminated soon afterward[76,125], but we conclude that the abrogation of BRCA2 and SLX4 localization is not due to meiotic arrest since, in wild-type spermatocytes, we observed the beginnings of BRCA2 accumulation in the mid pachytene stage and the beginnings of SLX4 accumulation in the early pachytene stage (**Figure 2.1g**, **2.1h**; **Supplementary Figure 2.3**). Thus, BRCA1 regulates the amplification of FANCD2 foci on the XY axes and is required for the accumulation of BRCA2 and SLX4 on the XY chromatin (**Figure 2.3e**). Therefore, while FANCD2, BRCA2, and SLX4 are each regulated by BRCA1, examination of meiotic cells shows that BRCA1 has distinct roles in the recruitment of FANCD2 versus BRCA2 and SLX4. In particular, BRCA1 may be more important for the recruitment of BRCA2 and SLX4 than for the recruitment of FANCD2.

After the BRCA1-mediated establishment of DDR signaling on the unsynapsed XY axes[76], MDC1 is essential for the initiation of MSCI[63]. MDC1 plays a crucial role in the somatic DDR[126-128] and works in a feedback loop with the TOPBP1-ATR network to spread γH2AX throughout XY chromatin in the early pachytene stage[63]. Because MDC1 recognizes XY chromatin at the onset of MSCI, we sought to determine the role of MDC1 in the recruitment of FA proteins. Similar to *Brca1*cKO cells, FANCD2 foci were present in spermatocytes deficient for MDC1 (*Mdc1*$^{-/-}$), unamplified on the XY axes, and persistent on autosome axes as spermatocytes progressed into the mid pachytene stage (**Figure 2.3f**, **2.3g**). Thus, MDC1, like BRCA1, regulates amplification of

FANCD2 foci on XY axes and the resolution of FANCD2 foci from autosome axes. Additionally, the accumulation of both BRCA2 and SLX4 on XY chromatin was abolished in *Mdc1*$^{-/-}$ cells at meiosis (**Figure 2.3h**, **2.3i**). Because *Mdc1*$^{-/-}$ spermatocytes undergo meiotic arrest at the mid pachytene stage, we conclude that the abolishment of BRCA2 and SLX4 accumulation is not due to meiotic arrest given that we observed neither the accumulation of BRCA2 in the mid pachytene stage nor the accumulation of SLX4 in the early pachytene stage. And because BRCA1 localization was not disturbed in *Mdc1*$^{-/-}$ spermatocytes[63], BRCA1 is upstream of MDC1 in meiosis. Taken together, BRCA1 and MDC1 cooperate in the same pathway in the regulation of FANCD2 foci on chromosomes axes, as well as in the accumulation of BRCA2 and SLX4 on XY chromatin (**Figure 2.3j**). Because BRCA2 and SLX4 are not regulated by the FA core complex and FANCD2 (**Figure 2.2**; **Supplementary Figure 2.4**), these results demonstrate that the functions of BRCA1 and MDC1 are uncoupled from those of the FA core complex and FANCD2.

RNF8 regulates the maintenance of FANCD2 and BRCA2 and is required for SLX4 accumulation. On the sex chromosomes, the E3 ubiquitin ligase RNF8 works downstream of MDC1 and is required for ubiquitination of the XY chromatin. RNF8 is also required for subsequent active epigenetic modifications on the XY chromatin during meiosis and for gene activation in postmeiotic round spermatids[72]. However, in the somatic DDR, MDC1 recruits and interacts with RNF8 to facilitate the recruitment of various downstream DDR factors[129-132]. Although RNF8 partially regulates the FA-BRCA pathway in the context of interstrand crosslink repair[132-134], the RNF8-mediated regulation of FA proteins in meiosis remains unknown. To investigate this possibility, we analyzed the recruitment of FA proteins in male mutant mice deficient for RNF8 (*Rnf8*$^{-/-}$). The accumulation of FANCD2 foci on XY axes was undisturbed in the early pachytene stage of *Rnf8*$^{-/-}$ spermatocytes (**Figure 2.4a**, **2.4b**). A reduced number of foci appeared on chromosome axes in the midst of condensation and synapsis in the leptotene/zygotene stages (**Figure 2.4b**). Strikingly, as *Rnf8*$^{-/-}$ spermatocytes progressed through the three pachytene stages, FANCD2 foci were not amplified along the XY axes through the late pachytene stage (**Figure 2.4a**, **2.4b**), in contrast to the FANCD2 foci dynamics of wild-type late pachytene spermatocytes (**Figure 2.1d**, **2.1e**). Thus, these data suggest that RNF8 is required for the amplification of FANCD2 foci on the XY axes. This is in contrast to the absence of FANCD2 foci on the XY axes in *Fanca* and *Fancc* mutants (**Figure 2.2a**; **Supplementary Figure 2.4a**).

Interestingly, we also observed severe impairment of BRCA2 accumulation in *Rnf8*$^{-/-}$ spermatocytes. In contrast to wild-type spermatocytes (**Figure 2.1g**; **Supplementary Figure 2.3**), the initial accumulation of BRCA2 was abrogated in most *Rnf8*$^{-/-}$ samples (**Figure 2.4c**, **2.4d**). However, as the late pachytene stage transitioned into the early diplotene stage, BRCA2 accumulated and spread over portions of the XY chromatin in *Rnf8*$^{-/-}$ spermatocytes with decreased efficiency compared to wild-type controls (**Figure 2.4c**, **2.4d**). SLX4 was more severely affected in *Rnf8*$^{-/-}$ cells: It did not accumulate on XY chromatin at all (**Figure 2.4e**). Thus, in addition to the RNF8-dependent amplification of FANCD2 foci on XY axes, RNF8 modulates the accumulation and maintenance of BRCA2 and is essential for the accumulation of SLX4 on the XY chromatin (**Figure 2.4f**). Because RNF8 works downstream of BRCA1 and MDC1 on the sex chromosomes[72,135], these results suggest that RNF8 is a key DDR factor regulating FANCD2. Furthermore, our data indicate a two-step mechanism for the formation of FANCD2 foci (**Figure 2.4g**): The first step is dependent on the FA core and regulates the initial accumulation of FANCD2 foci that begins in the leptotene stage; the second step regulates the amplification of FANCD2 foci on the XY axes through the BRCA1-MDC1-RNF8 signaling axis.

The initial accumulation of FANCD2 foci on XY axes likely represents persistent DNA double-strand breaks. In considering these findings, we sought to address the following question: Does the initial accumulation of FANCD2 foci on XY axes represent persistent DNA double-strand breaks (DSBs)? Persistent DSBs may serve as landmarks to target meiotic silencing to the sex chromosomes[76,136,137]. Given the possible recruitment of RAD51 to sites of unrepaired DSBs on the XY axes[137], we examined the extent to which FANCD2 foci overlapped with that of RAD51, which repairs DSBs by homologous recombination. In normal early pachytene spermatocytes, the initial accumulation of FANCD2 foci on XY axes largely overlapped that of RAD51 foci (**Figure 2.5a**), raising the possibility that FANCD2 foci on XY axes are at sites of unrepaired DSBs. FANCD2 colocalizes with RAD51 in spermatocytes transitioning from the mid to late pachytene stages as well (**Figure 2.5b**).

To further elaborate on the conclusion that FANCD2 foci occupy sites of unrepaired DSBs on XY axes, we performed immunofluorescence colocalization experiments using spermatocytes from the *Spo11* knockout model (*Spo11*$^{-/-}$), which is defective for SPO11-dependent DSBs[138,139]. SPO11 is responsible for generating programmed DSBs for meiotic recombination and is thus required for proper chromosome synapsis. Interestingly, a small number of RAD51 foci were reported in *Spo11*$^{-/-}$ spermatocytes, and these presumably represent SPO11-independent DNA repair foci[136]. We found that a reduced number of FANCD2 foci tend to colocalize with RAD51 foci in *Spo11*$^{-/-}$ spermatocytes (**Figure 2.5c**), suggesting that FANCD2 accumulates at SPO11-independent DNA repair foci.

SPO11-independent DNA repair foci were proposed to be the cause of the ectopic meiotic silencing that occurs in *Spo11*$^{-/-}$ spermatocytes[136]. Sites of ectopic meiotic silencing are referred to as pseudo-sex bodies since they are known to cover autosome chromatin[58,140]. In support of this notion, we found that the majority of observed FANCD2 foci colocalized with MDC1 domains: XY chromatin in control *Spo11*$^{+/-}$ spermatocytes (**Supplementary Figure 2.5a**) and pseudo-sex bodies in *Spo11*$^{-/-}$ spermatocytes (**Supplementary Figure 2.5b**). Together, these data support the possibility that the initial accumulation of FANCD2 foci represents persistent DSBs, which function to target the silencing machinery to unsynapsed chromatin, including the sex chromosomes, in meiotic prophase I.

FANCD2 cooperates with the BRCA1-MDC1-RNF8 axis for the accumulation of FANCM. In the course of our analyses of the sex chromosomes, we observed a dynamic temporal and spatial accumulation pattern for FANCM (**Figure 2.1c**; **Supplementary Figure 2.3**), an FA protein associated with the FA core complex. To further define the epistatic relationships of FA proteins, we designed experiments to examine the regulation of FANCM by proteins in a broad FA-DDR network composed of the FA core complex, FANCD2, and the BRCA1-MDC1-RNF8 signaling axis. We scored the accumulation patterns of FANCM in spermatocytes at different time points of meiotic prophase I and ran Pearson's chi-square test to identify categorical differences in accumulation between control and mutant samples. While FANCA, FANCB, and FANCC are dispensable for FANCM accumulation and maintenance (**Supplementary Figure 2.6a–d**; data not shown), FANCD2 is necessary for the proper accumulation and maintenance of FANCM signals on the sex chromosomes (**Figure 2.6a**, **2.6b**). Beginning in the early pachytene stage, FANCM accumulates on the sex chromosomes of *Fancd2*$^{-/-}$ spermatocytes with reduced efficiency (**Figure 2.6b**). As prophase progresses, FANCM fails to spread through the XY chromatin domain and, instead, is progressively lost from the XY chromatin and axes (**Figure 2.6b**). Given the normal accumulation and spreading of FANCM in the *Fanca*, *Fancb*, and *Fancc* knockout models (**Supplementary Figure 2.6a–d**; data not shown), these data indicate a function for FANCD2 that is independent of the FA core complex. Strikingly, we observed a more severe phenotype in the *Brca1*cKO and *Mdc1*$^{-/-}$ models: Our analyses revealed a drastic reduction of FANCM accumulation and spreading over the XY chromatin when compared to controls (**Figure 2.6c–f**). Our analyses also implicated RNF8 in the accumulation and maintenance of FANCM on the sex chromosomes: Although the phenotype was not as severe as those of *Brca1*cKO and *Mdc1*$^{-/-}$ spermatocytes, FANCM accumulation and maintenance was disrupted in *Rnf8*$^{-/-}$ samples (**Figure 2.6g**, **2.6h**). The extent of this disruption was similar to that observed in *Fancd2*$^{-/-}$ spermatocytes. Together, these data suggest that FANCD2, independent of the FA core complex, cooperates with the BRCA1-MDC1-RNF8 axis to regulate the accumulation and maintenance of FANCM on the sex chromosomes.

The FA core complex and FANCD2 are nonessential for upstream DDR events in MSCI and meiotic recombination. Given the possibility that FANCD2 functions independently of the FA core complex on the sex chromosomes, we evaluated the regulation of early DDR events in MSCI by the core complex-FANCD2 axis—also known as the FA pathway. For these experiments, we used the *Fancd2*$^{-/-}$ model as a proxy for loss of function of the FA pathway. We found that FANCD2 does not regulate the accumulation of early DDR factors that are crucial for the initiation of MSCI, including BRCA1, ATR, TOPBP1, γH2AX, and MDC1 (**Supplementary Figure 2.7a–e**). In our previous publication[68], we established that the FA core protein FANCB is also dispensable for the accumulation of these DDR factors. Consistent with our FANCB report, upstream DDR events occurred normally in *Fanca*$^{-/-}$ and *Fancc*$^{-/-}$ spermatocytes (data not shown). Together, these results indicate that the FA core complex and FANCD2 are dispensable for upstream DDR events on the sex chromosomes. Furthermore, these results explain why meiotic arrest is not induced in FA mutant mice: We infer that the FA pathway works downstream of γH2AX signaling and the initiation of MSCI, so FA deficiencies bypass meiotic arrest.

Because of the accumulation of FANCD2 foci on autosomes, we evaluated the role of the FA pathway in resolving DSBs via meiotic recombination. We examined two factors involved in DSB resolution: RAD51, an upstream recombinase in the DSB repair pathway, and MLH1, a downstream mismatch repair protein that catalyzes crossover recombination. We found the unperturbed formation of RAD51 and MLH1 foci in *Fancd2*$^{-/-}$ and control spermatocytes (**Supplementary Figure 2.75f–h**). Consistent with the normal formation of RAD51 and MLH1 foci, we detected normal chromosome synapsis in *Fancd2*$^{-/-}$ spermatocytes, as detected by double immunostaining for SYCP3 and SYCP1, a factor present at synapsed meiotic axes

(**Supplementary Figure 2.7i**). Combined, these data indicate a nonessential role for the FA pathway in meiotic recombination and chromosome synapsis.

FA core-dependent regulation of H3K9 methylation and FA core-independent regulation of H3K4 methylation. Because the FA pathway is not required for upstream DDR events, we sought to investigate possible downstream steps. Following the accumulation of DDR factors, epigenetic modifiers are recruited and histone post-translational modifications (hereafter "histone modifications") associated with the regulation of transcription are established on the XY chromatin during meiosis[64]. Our previous studies demonstrated that DDR factors regulate histone modifications on the XY chromatin: FANCB regulates H3K9 methylation[68], and RNF8 regulates H3K4 methylation and other active epigenetic modifications[72]. To determine a general role for the FA pathway in epigenetic programming, we tested the localization of several histone modifications on XY chromatin by immunostaining *Fanca*$^{-/-}$, *Fancc*$^{-/-}$, and *Fancd2*$^{-/-}$ spermatocytes. Because of the relationship between the FA proteins and RNF8, we investigated the possibility that the FA pathway is functionally linked to RNF8 by testing the RNF8-dependent active epigenetic modification H3K4me2[72]. In *Fanca*$^{-/-}$ and *Fancc*$^{-/-}$ spermatocytes, H3K4me2 accumulation on XY chromatin during the pachytene-to-diplotene transition was not affected (**Figure 2.7a**, **2.7b**; **Supplementary Figure 2.8a**, **2.6b**). However, in *Fancd2*$^{-/-}$ cells, accumulation of H3K4me2 was decreased on XY chromatin during the pachytene-to-diplotene transition (**Figure 2.7c**, **2.7d**). These results were confirmed through the quantification of relative mean fluorescence intensity (RMFI) from n = 3 sets of independent samples for *Fanca*, *Fancc*, and *Fancd2* mutants and littermate controls (**Materials & Methods**). Thus, FANCD2 regulates H3K4me2 accumulation on the XY chromatin, whereas the FA core factors do not. Since RNF8 is involved in the amplification of FANCD2 on sex chromosomes (**Figure 2.4a**, **2.4b**), FANCD2 may act downstream to mediate RNF8-dependent H3K4me2 accumulation. Together, these results suggest that RNF8 is a central factor that integrates the broader FA-BRCA pathway.

Next, we examined the regulation of H3K9me2 by the FA pathway; a silent epigenetic modification, H3K9me2 accumulates on XY chromatin in the transition from the pachytene to diplotene stages[69,141]. During this transition, in *Fanca*$^{-/-}$, *Fancc*$^{-/-}$, and *Fancd2*$^{-/-}$ spermatocytes, H3K9me2 was diminished on the sex chromosomes in comparison to wild-type sex chromosomes (**Figure 2.7e–h**; **Supplementary Figure 2.8c**, **2.6d**). Together with our previous study demonstrating that FANCB regulates H3K9me2 on XY chromatin[68], these results suggest that the FA core complex and FANCD2 are required for the regulation of H3K9me2 on XY chromatin during the pachytene-to-diplotene transition.

Because we previously found that FANCB negatively regulates H3K9me3[68], we investigated the regulation of H3K9me3 by the FA pathway. In wild-type spermatocytes, H3K9me3 initially accumulates on XY chromatin in the early pachytene stage and disappears in the mid pachytene stage due to histone H3 replacement[75]; then, in the late diplotene stage, H3K9me3 reaccumulates on the XY chromatin[75]. In *Fanca*$^{-/-}$, *Fancc*$^{-/-}$, and *Fancd2*$^{-/-}$ spermatocytes, H3K9me3 intensity was increased on both early pachytene and late diplotene sex chromosomes in comparison to wild-type sex chromosomes (**Figure 2.7i–l**; **Supplementary Figure 2.8e**, **2.6f**). These results suggest that the FA pathway negatively regulates H3K9me3 both at the early pachytene and late diplotene stages. Taken together, we conclude that the FA pathway positively regulates H3K9me2 and negatively regulates H3K9me3 on XY chromatin. Therefore, the FA core complex is required for the regulation of H3K9 methylation, while the regulation of H3K4me2 is independent of the FA core complex.

These findings led us to examine the transcriptional status of the meiotic sex chromosomes in *Fancd2*$^{-/-}$ spermatocytes—which, in these experiments, serve as proxies for loss of function of the FA pathway. First, we performed RNA fluorescence in situ hybridization (FISH) using Cot-1 DNA probes. Cot-1 DNA probes consist of repetitive elements that can hybridize nascent transcripts, enabling the visualization of transcriptionally active regions[69,142,143]. Our data revealed no obvious changes in the visualization of Cot-1 between control *Fancd2*$^{+/+}$ and experimental *Fancd2*$^{-/-}$ spermatocytes (**Supplementary Figure 2.9a**): Cot-1 was largely excluded from the XY chromatin in both control and *Fancd2*$^{-/-}$ spermatocytes, suggesting that the global transcription level is comparable between the control and mutant spermatocytes. As a complementary approach to visualizing the transcriptional status of the sex chromosomes, we performed immunolocalization experiments for RNA Polymerase II (RNAPII) in control *Fancd2*$^{+/+}$ and experimental *Fancd2*$^{-/-}$ spermatocytes. Similar to Cot-1, RNAPII was largely excluded from the XY chromatin in both the control and mutant spermatocytes (**Supplementary Figure 2.9b**). These data suggest that the initiation of MSCI is not perturbed in mutants deficient for FANCD2, although we were not able to define the transcriptional status of individual genes due to the limited numbers of *Fancd2*$^{-/-}$ spermatocytes.

As a whole, our findings define the FA-DDR network in meiosis, yield insights into the recruitment of FA proteins, and illuminate the male sex chromosomes as a model to dissect the broad FA-BRCA pathway.

Discussion

In this study, we have defined how the FA-DDR network is coordinated during meiosis. By comparing mutants for FA core proteins and FANCD2, we revealed core-dependent and core-independent functions of the FA pathway on the meiotic sex chromosomes. In particular, we uncovered a role for the FA core complex in the accumulation of FANCD2 foci during meiosis. This is parallel to the role of the FA pathway in regulating FANCD2 foci in the somatic DDR[99,108]. However, the FA core complex is dispensable for the recruitment of BRCA2 and SLX4 to the sex chromosomes, so FA proteins do not appear to be recruited to sex chromosomes in meiosis through a simple linear pathway. And although a previous report demonstrated the necessity for FANCD2 in the recruitment of SLX4 to DNA interstrand crosslinks in somatic cells[117], our results reveal the FANCD2-independent recruitment of SLX4 to XY chromatin in meiosis. Although there may be distinct mechanisms in somatic cells versus the meiotic sex chromosomes, one notable feature of the sex chromosome DDR is that upstream factors tend to present on axes and downstream factors tend to present on XY chromatin. In this regard, the differential localization of RAD51 and BRCA2—two factors reported to associate with each other in the canonical somatic DDR—suggests the distinct regulation of each factor. In accord with this notion, in somatic cells, there is evidence for BRCA2-independent, non-canonical regulation of RAD51 recruitment to damaged chromatin[144].

Previously, we found that the focal accumulation of FANCB, an FA core protein, on the XY chromosomes is dependent on MDC1[68]. Interestingly, while we find that initial FANCD2 foci are present in *Mdc1*$^{-/-}$ spermatocytes, MDC1 is required for the subsequent amplification of FANCD2 foci. Thus, focal accumulation of FANCB may not be required for initial FANCD2 foci formation. In this context, it should be noted that there may be some independence in the recruitment of FA core complex proteins since they can form distinct subcomplexes[145].

Our data indicate that FANCM accumulation on the sex chromosomes is independent of FA core complex proteins. Yet strikingly, we report that FANCM accumulation and maintenance on the sex chromosomes is dependent on FANCD2 and the BRCA1-MDC1-RNF8 signaling axis. FANCM is an evolutionarily conserved helicase and mammalian ortholog of the archaeal DDR factor Hef[146], and indeed, FANCM, but not the other FA core factors, has an evolutionarily conserved role in suppressing meiotic crossover recombination, and FANCM directs non-crossover recombination[147,148]. Therefore, these reports underscore an essential and ancient function of FANCM in meiosis that is likely to be independent of the FA core complex. While FANCM has a role in promoting FANCD2 monoubiquitination and localization in the somatic DDR[149], we expect that FANCM functions with the BRCA1-MDC1-RNF8 axis independent of the FA core complex to regulate the broad FA-DDR network in meiosis.

By using mutants from the BRCA1-MDC1-RNF8 signaling axis, we show that BRCA1, MDC1, and RNF8 regulate the recruitment of BRCA2 and SLX4. Rather than having a role in the recruitment of FANCD2 to the XY axes, BRCA1, MDC1, and RNF8 are involved in the amplification of FANCD2 signals on the sex chromosomes. Notably, we previously observed a BRCA1-dependent signal amplification of RAD51 foci[76] that is similar to the amplification of FANCD2 foci found in this study. This suggests that FANCD2 and RAD51 foci may be amplified similarly along the XY axes. Consistent with this possibility, a study identified *Rad51* as the FA gene *Fancr*[98]. Given the possible recruitment of RAD51 to sites of unrepaired double-strand breaks (DSBs) on the XY axes[137], initial signals of FANCD2 and RAD51 may represent sites of unrepaired DSBs. Indeed, our results demonstrate that the initial signals for FANCD2 foci colocalize with RAD51 foci on XY axes in normal meiosis. Our analyses of *Spo11*$^{-/-}$ spermatocytes further support this assertion since FANCD2 colocalizes with RAD51 at SPO11-independent DNA repair foci.

FANCD2 and RAD51 signals may be amplified at undetermined sites regulated by BRCA1-MDC1-RNF8 signaling along the XY axes. These data suggest that BRCA1, MDC1, and RNF8 work as a single pathway in the regulation of FA proteins (**Figure 2.7m**). A clue to understand these undetermined sites may be inferred by studies of somatic cells; for example, a proteomics analysis identified the recruitment of DDR proteins to DNA interstrand crosslinks[150]. Because the proteins in the FA-DDR network are crucial for the repair of DNA interstrand crosslinks, it would be intriguing to compare the factors present both at meiotic sex chromosomes and DNA interstrand crosslinks in somatic cells.

Here, by investigating meiosis, we demonstrate a critical role for RNF8 in the regulation of four different FA proteins: FANCM, FANCD2, BRCA2, and SLX4 (**Figure 2.7m**). One possible mechanism by which RNF8 regulates FA proteins is RNF8-mediated ubiquitination established on the XY chromatin for subsequent epigenetic programming[72]. In support of this possibility, SLX4 binds ubiquitinated substrates[117]. This may help to explain our finding that SLX4 recruitment to XY chromatin is dependent on RNF8. In turn, we demonstrate here that FANCD2, but not FA core proteins, modulates H3K4me2, an RNF8-dependent modification, suggesting a possible role for

FANCD2 in RNF8-dependent epigenetic programming. The functional link between FANCD2 and RNF8 is further supported by the fact that both factors regulate FANCM. Based on these results, we propose a model in which FANCD2 and RNF8 function together, serving as a central link between the FA pathway and the BRCA1-MDC1-RNF8 signaling axis to integrate the FA-DDR network (**Figure 2.7m**).

Unlike H3K4me2, H3K9 methylation is regulated by FA core factors. Thus, there are both core-dependent and core-independent roles for FANCD2 in meiotic prophase I. A previous report showed that germ cells and testicular size were severely compromised in *Fancd2*$^{-/-}$ mice[111] as compared with other mutants for FA core subunits (including *Fanca*$^{-/-}$ and *Fancc*$^{-/-}$) that display subfertility[151,152]. The severe germline phenotype of *Fancd2*$^{-/-}$ mice could indicate additional roles for FANCD2 beyond its canonical function in the FA pathway downstream of the FA core complex. The different roles for FANCD2 and the FA core complex in epigenetic regulation could be related to the fact that the localization of FANCD2 is regulated by both the FA core complex and by RNF8. FANCD2 foci require the FA core complex, and the FA pathway may, therefore, be involved in the regulation of H3K9 methylation.

In contrast, the role of FANCD2 in the regulation of H3K4me2 levels does not appear to depend on its monoubiquitination, since the FA core complex is not involved in regulating H3K4me2. But RNF8 also has some control over FANCD2 foci, which could be related to FA core-independent regulation of H3K4me2 levels. To clarify the molecular mechanisms that underlie these differences, it will be important to dissect the molecular link between FA proteins and epigenetic programming in future studies. We demonstrated that the substrate of RNF8-mediated ubiquitination on XY chromatin is an unknown target that is not histone H2A[3]. While this ubiquitin substrate of RNF8 had a different size and, therefore, is not likely to be FANCD2, it will be important to identify this substrate, and it will be interesting to evaluate its regulation by FANCD2. Intriguingly, the function of FANCD2 in epigenetic programming of the sex chromosomes concurs with the finding that FANCD2 has histone chaperone activity in DNA crosslink repair[153]. Because the initiation of MSCI is followed by the replacement of histone H3.3[75], it is conceivable that FANCD2 is involved in this step to regulate epigenetic programming.

Taken together, these results demonstrate that the FA proteins, together with MDC1 and RNF8, comprise the FA-DDR network, which governs the sex chromosomes during meiosis (**Figure 2.7m**). This raises the possibility that common pathways underlie the regulation of the sex chromosomes during meiosis and the somatic DDR. Therefore, MSCI has emerged as a model system to dissect the roles of different FA proteins in the DDR and in epigenetic programming, and for understanding how FA proteins are both regulated and interrelated. In future studies, the coordinated spatial and temporal localization of FA proteins on the meiotic sex chromosomes will enable the use of FA genetic models to dissect, in high resolution, the details of the FA-BRCA pathway and subsequent epigenetic programming. Furthermore, the functional consequence of histone modification changes observed in FA mutant mice has emerged as another important area of investigation. Because RNF8 is required for establishing active histone modifications on the sex chromosomes, as well as the selective activation of male reproduction genes from the inactive sex chromosomes in spermatids[72], it is possible that the changes in histone modifications may alter the expression of individual genes from the silent sex chromosomes in FA mutant mice. Understanding the roles of FA proteins in epigenetic programming may also be important for understanding fertility defects associated with FA and for elucidating the roles and regulation of FA proteins in DNA repair.

Statistical Analyses

Means were compared using unpaired two-tailed Student's t tests for experiments involving two groups. Two-tailed one-way ANOVA was used when comparisons were made across more than two groups, and Tukey's method was performed as a posttest for pairwise comparisons. Pearson's chi-square test was used to identify categorical differences in the accumulation of BRCA2 (**Figure 2.4**) and FANCM (**Figure 2.6**; **Supplementary Figure 2.6**) between two groups. Unless specified, P values are indicated with text or asterisks as follows: n.s., not significant, $P > 0.05$; * $P \leq 0.05$; ** $P \leq 0.01$; *** $P \leq 0.001$.

Materials & Methods

Animals. *Fanca*$^{-/-}$, *Fancb*$^{-/Y}$, *Fancc*$^{-/-}$, *Fancd2*$^{-/-}$, *Mdc1*$^{-/-}$, *Rnf8*$^{-/-}$, and *Spo11*$^{-/-}$ mouse models are described in the literature[68,111,139,154-157]. Mice with a conditional deletion of *Brca1* exon 11 using *Ddx4*-Cre are also described in the literature[76]. *Rnf8*$^{-/-}$, *Mdc1*$^{-/-}$, *Fancb*$^{-/Y}$, and *Spo11*$^{-/-}$ mouse models were on C57Bl/6 backgrounds; *Fanca*$^{-/-}$, *Fancc*$^{-/-}$, *Fancd2*$^{-/-}$, and *Brca1*cKO mouse models were on mixed backgrounds. This work was approved by Institutional Animal Care and Use Committee protocol no. IACUC2015-0032.

Here, we provide details on the generation of the *Brca1*cKO model: Mice with floxed alleles for *Brca1* exon 11[158] were obtained from the National Cancer Institute mouse repository. *Ddx4*-Cre (also known as *Vasa*-Cre) transgenic mice[121] were obtained from the Jackson Laboratory. Because the *Ddx4*-Cre allele needs to be transmitted from the paternal allele to generate mice with a germline-specific conditional deletion, males with *Brca1*$^{F/+}$ *Ddx4*-Cre were mated with females homozygous for the floxed allele of *Brca1* exon 11 (*Brca1*$^{F/F}$). The conditional deletion model *Brca1*$^{F/\Delta}$ *Ddx4*-Cre (*Brca1*cKO) was obtained from such pairings; we used *Brca1*$^{F/+}$ *Ddx4*-Cre littermates as controls.

Preparation of surface spreads of meiotic chromosomes. Meiotic chromosomes were analyzed with surface spreads prepared via hypotonic treatment, modified from an established protocol[159]. Briefly, testes were excised and placed in PBS after removing extratesticular tissues. Seminiferous tubules—approximately one-quarter of an adult wild-type or heterozygous testis, or approximately one-half of an adult mutant testis—were transferred to a four-well dish (e.g., Thermo Scientific Nunc 4-Well Dishes, 144444) on ice. Three of the four wells contained 1 mL PBS; the fourth well contained 1 mL hypotonic extraction buffer (HEB; prepared as described[159]). In the first well containing 1 mL PBS, seminiferous tubules were gently unraveled into small clumps with fine-point tweezers, and care was taken not to tear or mince the seminiferous tubules. The clumps of seminiferous tubules were transferred to the second and third wells of 1 mL PBS for additional unraveling before transfer to the fourth well containing 1 mL HEB. Once in the fourth well, fine-point tweezers were used to carefully expose tubule surface area to HEB. The seminiferous tubules were incubated in HEB on ice for approximately three hours with gentle stirring every 30–45 minutes.

After incubation, a small clump of seminiferous tubules—approximately four-to-six seminiferous tubules—was gently pulled and mashed between the tips of tweezers in 30 µL of sucrose (100 mM, pH 8.2) on a plain, uncharged microscope slide (e.g., Thermo Scientific Gold Seal, 3010-002). After approximately 15–25 mashes, a semi-translucent cell suspension was formed. An additional 30 µL of sucrose was mixed with the suspension, gently pipetted up and down to mix and dilute the cell suspension. 30 µL volumes of the diluted cell suspension were applied to a positively charged slide (e.g., Thermo Scientific Probe On Plus, 22-230-900) that was incubated in chilled fixation solution (2% paraformaldehyde, 0.05% Triton X-100, and 0.02% sodium monododecyl sulfate, adjusted to pH 9.2 with sodium borate buffer, prepared as described[159]) for a minimum of two minutes. After applying the cell suspension/sucrose mixture, the slide was slowly, gently tilted up and down at slight angles to mix the cell suspension/sucrose mixture with remaining fixation solution. The previous steps were repeated until a desired number of slides were created.

The slides were placed in closed humid chambers at room temperature for a minimum of one hour (maximum timespan of overnight, i.e., ~12–16 hours) before opening the humid chamber lid to facilitate drying of the slides (approximately two hours). Once dry, the slides were washed in a low-concentration surfactant, 0.4% Photo-Flo 200 (Kodak, 146-4510), at room temperature two times for two minutes each. Slides were dried completely at room temperature (approximately 30 minutes) before staining or storage in slide boxes at -80°C.

Immunofluorescence staining of surface spreads of meiotic chromosomes. For immunostaining experiments, surface spreads were incubated in PBS-Tween 20 (PBST; 0.1% Tween 20 in 1×PBS) for 5-30 minutes before blocking in antibody dilution buffer (0.15% BSA, 0.1% Tween 20 in 1×PBS), or 1% BSA dissolved in autoclaved deionized H_2O, for an additional 30–60 minutes. Primary antibodies were diluted in antibody dilution buffer, forming an antibody solution. Then, surface spreads were coated with 100 µL of the antibody solution, gently covered with Parafilm, and stored for a minimum of six hours (maximum timespan of overnight, i.e., ~12–16 hours) in a humid chamber at room temperature or 4°C. The following antibodies, at the following dilutions, were used in this study:

- rabbit polyclonal anti-ATR (Cell Signaling, 2790), 1:50
- rabbit polyclonal anti-BRCA1 (generated in the Namekawa lab[63]), 1:1,500
- rabbit polyclonal anti-BRCA2 (generated in the Andreassen lab in rabbits by fusing the 2800-3000 amino acid-fragment of human BRCA2 to GST), 1:100
- rabbit polyclonal anti-FANCB (generated in the Namekawa lab[68]), 1:100
- rabbit polyclonal anti-FANCD2 (E35), 1:200
- rabbit polyclonal anti-FANCD2 (Novus, NB100-182), 1:200
- rabbit polyclonal anti-FANCM (Fanconi Anemia Research Foundation, D3823), 1:100

- rabbit polyclonal anti-H3K4me2 (EMD Millipore, 07-030), 1:500
- mouse monoclonal anti-H3K9me2 (Abcam, ab1220), 1:200
- rabbit polyclonal anti-H3K9me3 (EMD Millipore, 07-442), 1:250
- rabbit polyclonal anti-RAD51 (Santa Cruz Biotechnology, sc-8349), 1:50
- sheep polyclonal anti-MDC1 (Bio-Rad Antibodies, AHP799), 1:500
- rabbit polyclonal anti-MLH1 (Santa Cruz Biotechnology, sc-11442), 1:100
- mouse monoclonal anti-RNAPII (EMD Millipore, 05-952), 1:100
- rabbit polyclonal anti-SLX4 (gift from the Cohen lab[113]), 1:100
- rabbit polyclonal anti-SYCP1 (Abcam, ab15090), 1:1,500
- mouse monoclonal anti-SYCP3 (Abcam, ab97642), 1:5,000
- rabbit polyclonal anti-SYCP3 (Novus, NB300-231), 1:500
- rabbit polyclonal anti-TOPBP1 (gift from the Chen lab[160]), 1:500

After incubation of the primary antibodies, slides were washed three times for approximately five minutes each in PBST. Then, the slides were incubated with secondary antibodies conjugated to fluorophores (Thermo Fisher, Biotium, or Jackson ImmunoResearch). All secondary antibodies were diluted 1:500 in antibody dilution buffer. Slides were coated with 100 µL of antibody solution and then gently covered with Parafilm for approximately 30 minutes in humid chambers in darkness. Finally, slides were washed in PBST three times for five minutes each in darkness, then mounted in Vectashield (Vector Laboratories) containing 0.15% DAPI. Slides were either imaged immediately or stored at 4°C in darkness. For long-term storage, stained slides were kept at 4°C in darkness.

For double immunostaining using two primary antibodies from the same host species, rabbit polyclonal anti-FANCD2 antibody and rabbit polyclonal anti-RAD51 antibody, secondary $F(ab)_2$-fragment antibodies conjugated to fluorophores were used as suggested by the manufacturers. Briefly, we performed immunostaining of anti-RAD51 antibody (six hours-to-overnight; dilution described above) and detected with $F(ab)_2$ goat anti-rabbit IgG conjugated with

Alexa Fluor 555 (Thermo Fisher; dilution described above). Then, slides were fixed in 1 mL of fresh, chilled 4% paraformaldehyde/1×PBS solution at room temperature for 10 minutes in a humid chamber. After briefly washing the fixed slides in PBST, we performed a second round of immunostaining with anti-FANCD2 antibody (six hours-to-overnight; dilution described above) followed by detection with $F(ab)_2$ donkey anti-rabbit IgG conjugated with Alexa Fluor 647 (Thermo Fisher; dilution described above).

3D slide preparation and FISH. To conserve the morphology of meiotic chromatin, specialized slides that preserve the 3D nuclear organization of testicular germ cells were prepared as described[69,161,162]. Briefly, seminiferous tubules underwent permeabilization, fixation, and then mechanical dissociation with fine-point tweezers before being cytospun onto positively-charged slides (e.g., Thermo Superfrost Plus, 12-550-15). Cot-1 RNA FISH was performed as described[161].

Microscopy and image analyses. All images of germ cells were acquired with an ECLIPSE Ti-E microscope (Nikon) and Zyla 5.5 sCMOS camera (Andor Technology), with 60× and 100× CFI Apochromat TIRF oil immersion lenses (Nikon), numerical apertures 1.40. Photoshop and Illustrator (CS6, Adobe) were used for composing figures. Primary spermatocytes were staged by assessing immunostains against SYCP3 (described in detail in **Supplementary Figure 2.1**). For data analyses, matched substages of meiotic prophase I were analyzed in controls and mutants. All data were confirmed with at least three independent control-mutant littermate pairs of mice.

Sample images of spermatocytes stained with anti-FANCD2, anti-BRCA2, anti-FANCM, and anti-MLH1 antibodies were blinded and manually scored with the ImageJ[163] processing package Fiji[164]. Sample images were blinded, scored, unblinded, and sorted through the following workflow:

1. Images were batch converted from the Nikon file format, `.nd2`, to the `.tif` file format with ImageJ.
2. Composite `.tif` files were batch blinded with ImageJ.
3. After counts of foci were determined and recorded in Excel (Microsoft), the composite `.tif` filenames were unblinded and sorted by genotypes and stages of meiotic prophase I.
4. Data were imported to Prism 6 (GraphPad) for statistical analyses. Graphs of counts of foci (e.g., FANCD2 and MLH1) were composed with Prism 6 and Illustrator; graphs of percentage accumulation (BRCA2 and FANCM) were composed with Excel and Illustrator.

H3K4me2, H3K9me2, and H3K9me3 signals were quantified with NIS-Elements Basic Research software (Nikon). Briefly, regions of interest (ROIs) were drawn around XY bodies, denoted as XY in **Figure 2.7** and **Supplementary Figure 2.6**, and prophase nuclei excluding the XY body, denoted as $\mathrm{Au.}$ (for "autosome region") in **Figure 2.7** and **Supplementary Figure 2.6**. XY and $\mathrm{Au.}$ ROIs were normalized to image background ROIs. For normalization of signals on a relative scale (0 to 1.5 for H3K4me2 and H3K9me2 analyses, 0 to 2 for H3K9me3 analyses), we calculated the mean of all diplotene XY body ROI signals, $\mathrm{XY}_{\mathrm{diplotene\ mean}}$, and then divided each XY and $\mathrm{Au.}$ ROI signal value by the $\mathrm{XY}_{\mathrm{diplotene\ mean}}$ value. This provided a value for ROI signals termed the "relative mean fluorescence intensity" (RMFI). The independent samples were combined and statistical analyses were run through Excel and Prism 6. RMFI graphs were composed with Prism 6 and Illustrator.

Cell culture. A human lymphoblast cell line deficient for FANCD2, PD20[110], was stably transduced with WT-FANCD2; FANCD2 in which lysine 561 has been mutated to arginine (K561R), making the protein non-ubiquitinable; or an empty pMMP retroviral vector[165]. Cells were cultured in 10% fetal bovine serum RPMI 1640 medium containing 1 µg/mL puromycin. To induce monoubiquitination of FANCD2 in PD20 cells, DNA replication was arrested by treatment with 2 mM hydroxyurea, added from 200 mM stock in growth medium kept at -20°C.

Western blotting. Whole testes and hydroxyurea-treated PD20 cells were dounce-homogenized with RIPA buffer (10 mM Tris-HCl pH 7.5, 150 mM NaCl, 1 mM EDTA, 0.1% SDS, 0.1% NaDOC, 1% Triton X-100) containing protease inhibitor cOmplete (Roche). After the measurement of protein concentrations via the Bradford assay, lysates were mixed with an equal volume of 2× Laemmli sample buffer (prepared and stored at 4× concentration: 2% sodium dodecyl sulfate, 10% glycerol, 60 mM Tris-HCl pH 6.8, 1% v/v β-mercaptoethanol, and bromophenol blue), mixed with Benzonase (0.5 μL/100 μL lysate), and then incubated on ice for approximately 30 minutes, with gentle mixing every 10 minutes. If still viscous, the lysates were briefly sonicated on ice. Otherwise, the lysates were immediately boiled for 10 minutes. Using gels with 4% stacking and 6% running concentrations, SDS-PAGE was performed as follows: 80 V in the stacking portion and 150 V in the running portion. Semi-dry transfer was performed with the Trans-Blot Turbo Transfer System (Bio-Rad, 1704155) by following the transfer method used by R&D Systems (Bio-Techne), described at the following URL:

- https://www.rndsystems.com/resources/protocols/western-blot-qc-protocol#Transfer

Using a PVDF membrane wetted in 100% methanol, semi-dry transfer was run for one hour with a constant current of 200 mA (15 V maximum). Afterwards, the membrane was blocked in StartingBlock Blocking Buffer (Thermo Scientific, 37538) for approximately 25 minutes, washed for 10 minutes in TBS-Tween 20 (TBST; 0.1% Tween 20 in 1×PBS) two times, and then incubated with primary antibody. The following primary antibodies were diluted in TBST and then coated on the membrane for approximately one hour at room temperature:

- rabbit polyclonal anti-FANCD2 antibody (G33), 1:1,000
- rabbit polyclonal anti-FANCD2 antibody (E35), 1:1,000
- rabbit polyclonal anti-FANCD2 antibody (Novus NB100-182), 1:1,000

Then, the membrane was washed for 10 minutes in TBST three times, incubated in HRP-labeled anti-rabbit IgG diluted in TBST (1:5,000), and incubated for one hour. After washing for 10 minutes in TBST four times, the membrane was visualized using Pierce ECL Western Blotting Substrate (Thermo Scientific, 32106) per the manufacturer's instructions.

FANCM peptide competition. The specificity of FANCM antibody was confirmed with peptide competition experiments using a FANCM peptide (CFDIQMLPNDLNQDRLKSDI) according to instructions at the Abcam website:

- http://www.abcam.com/protocols/blocking-with-immunizing-peptide-protocol-peptide-competition

Acknowledgments

For discussion and/or helpful comments regarding the manuscript, we thank past and present members of the Namekawa Lab, Andreassen Lab, and the Division of Reproductive Sciences, Cincinnati Children's Hospital Medical Center. We also thank the following researchers and organizations: For providing *Fanca*$^{+/-}$ mice, Madeleine Carreau, Laval University; for providing *Fancc*$^{+/-}$ mice, Manuel Buchwald, Hospital for Sick Children; for providing *Fancd2*$^{+/-}$ mice, Markus Grompe, Oregon Health Sciences University; for providing *Mdc1*$^{+/-}$ and *Rnf8*$^{+/-}$ mice, Junjie Chen, MD Anderson Cancer Center; for *Spo11*$^{+/-}$ mice, R. Daniel Camerini-Otero, National Institute of Diabetes and Digestive and Kidney Diseases; for the FANCM antibody, the Fanconi Anemia Research Fund; for answering questions related to Fanconi anemia antibodies, Ray Monnat, University of Washington; for FANCD2 antibodies (G33, E35), Alan D'Andrea, Dana-Farber Cancer Institute; and for the SLX4 antibody, Paula E. Cohen, Cornell University. Funding sources: Research Grant (FY13-510) from the March of Dimes Foundation to Satoshi H. Namekawa; National Institutes of Health (NIH) R01 HL085587 to Paul R. Andreassen; NIH R01 GM098605 to Satoshi H. Namekawa.

Author Contributions

Kris G. Alavattam, Paul R. Andreassen, and Satoshi H. Namekawa wrote the manuscript with all other authors. Kris G. Alavattam, Paul R. Andreassen, and Satoshi H. Namekawa designed the experiments. Kris G. Alavattam performed and interpreted most of the experiments. Yasuko Kato, Ho-Su Sin, So Maezawa, Ian J. Kowalski, Fan Zhang, and Satoshi H. Namekawa contributed experiments. Qishen Pang and Paul R. Andreassen provided materials. Satoshi H. Namekawa was the supervisor of this work.

Competing Interests

The authors declare no competing interests.

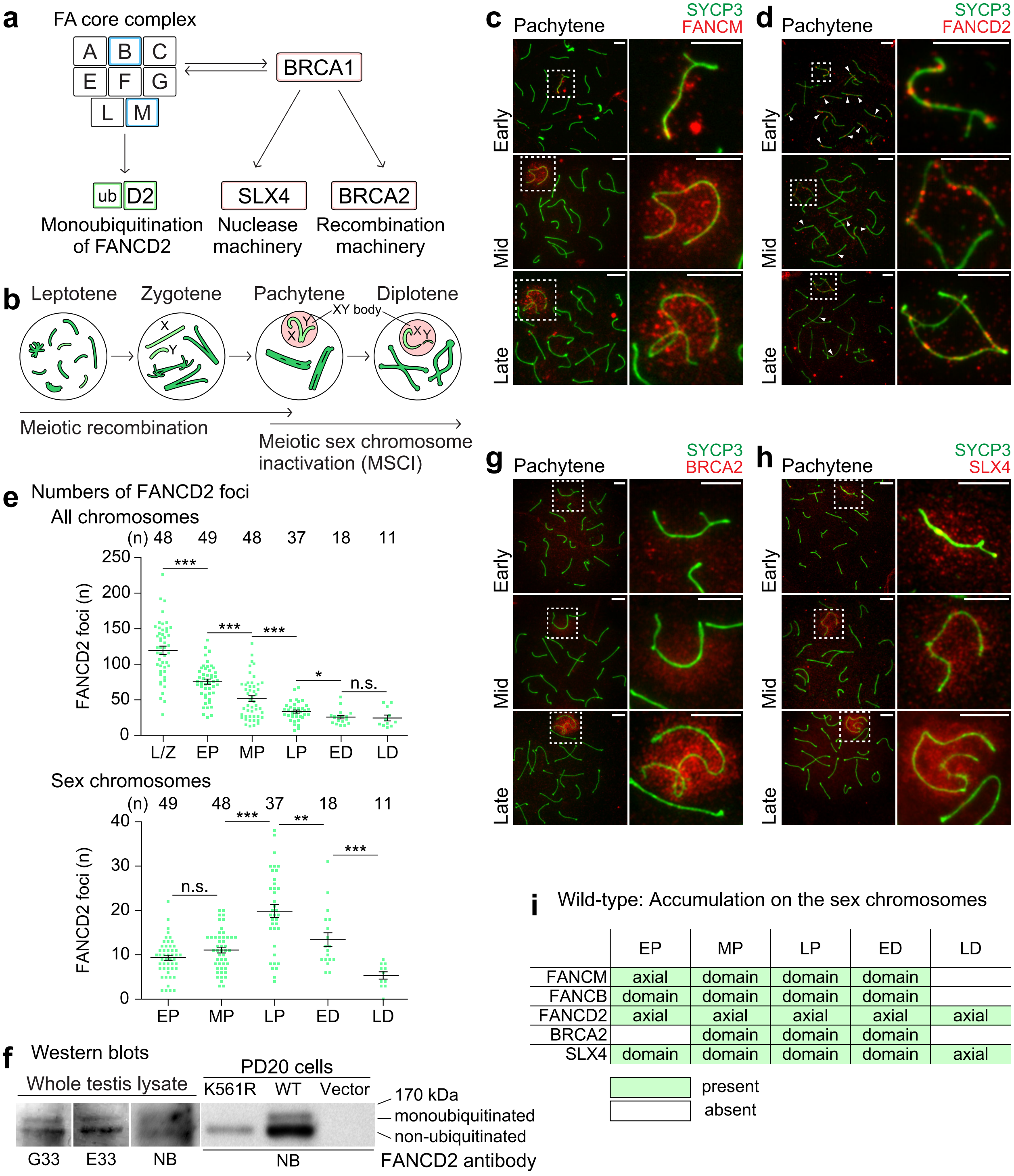

Wild-type: Accumulation on the sex chromosomes

	EP	MP	LP	ED	LD
FANCM	axial	domain	domain	domain	
FANCB	domain	domain	domain	domain	
FANCD2	axial	axial	axial	axial	axial
BRCA2		domain	domain	domain	
SLX4	domain	domain	domain	domain	axial

🟩 present
⬜ absent

Figure 2.1: The FA-BRCA pathway is activated on the sex chromosomes during meiosis.

Figure 2.1: The FA-BRCA pathway is activated on the sex chromosomes during meiosis.

a, Schematic of the FA-BRCA pathway. FA proteins analyzed in this study are shown in color.

b, Schematic of stages of meiotic prophase.

c, **d**, **g**, **h**, Immunostains using antibodies against the indicated proteins in meiotic chromosome spreads from wild-type mice. SYCP3 is a marker for meiotic chromosome axes. Substages are labeled to the left. Dashed squares border sex chromosomes and are magnified to the right. Arrowheads: selected FANCD2 foci present on synapsed autosomes. Consistent results were obtained with n = 3 independent mice. Scale bars, 5 μm.

e, Total numbers of FANCD2 foci on all chromosome axes (top) and on the sex chromosome axes (bottom) per spermatocyte for stages of meiotic prophase. Numbers of spermatocytes analyzed are noted above each graph. Bars represent means and standard errors. Data are aggregated from n = 6 wild-type adult mice. *P* values are derived from unpaired, two-tailed Student's t tests: n.s., not significant; $P > 0.05$; * $P \leq 0.05$; ** $P \leq 0.01$; *** $P \leq 0.001$. Prophase spermatocyte stage abbreviations: L/Z, leptotene and zygotene; EP, early pachytene; MP, mid pachytene; LP, late pachytene; ED, early diplotene; LD, late diplotene.

f, Western blot analyses with three independent anti-FANCD2 antibodies (G33, E33, and Novus NB100-182 antibody: NB). K561R, PD20 cells expressing a mutated form of FANCD2 incapable of being monoubiquitinated; WT, PD20 cells complemented with wild-type *FANCD2*; Vector, PD20 cells complemented with an empty vector.

i, Summary of spatial and temporal staining patterns for anti-FA protein antibodies on the sex chromosomes of wild-type mice. Axial, FA factors spread along XY axes. Domain, FA factors spread along XY axes and through XY chromatin. For comparison, FANCB results from our previous study[68] are summarized here.

See also **Supplementary Figures 2.1–2.3**.

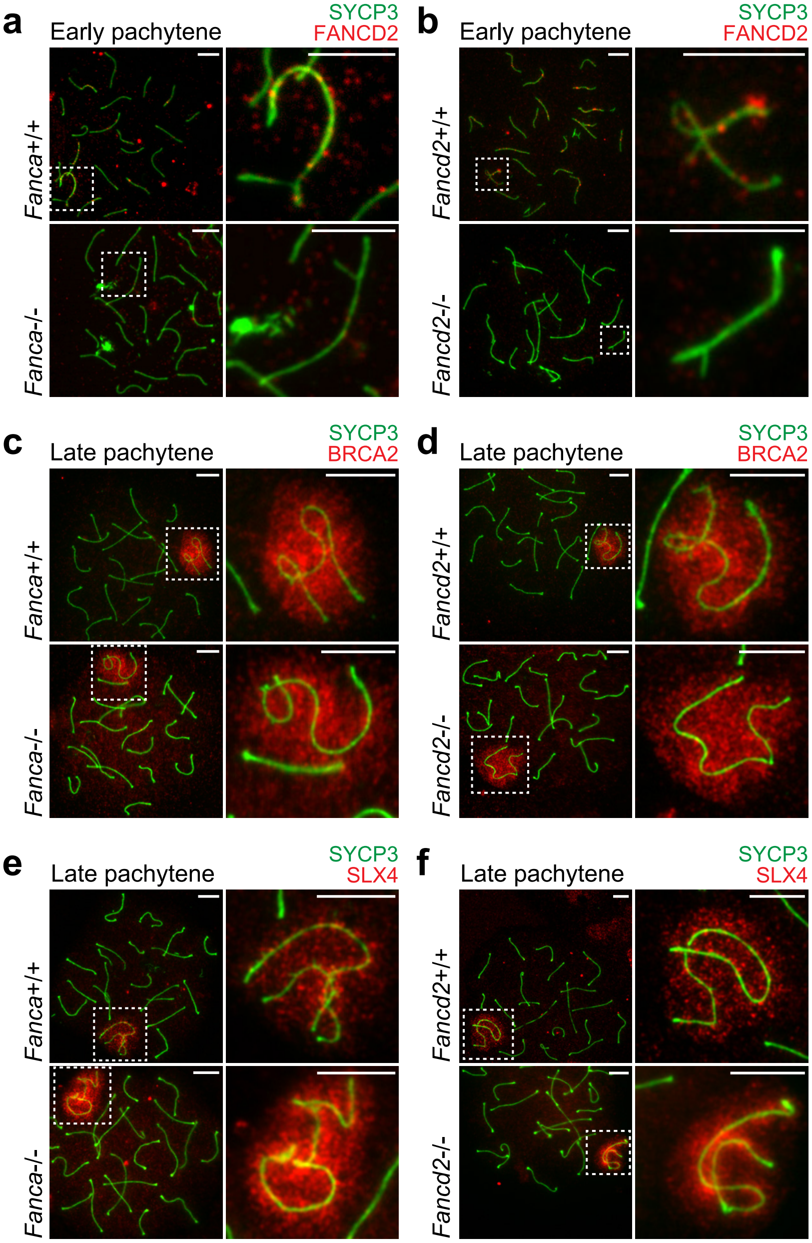

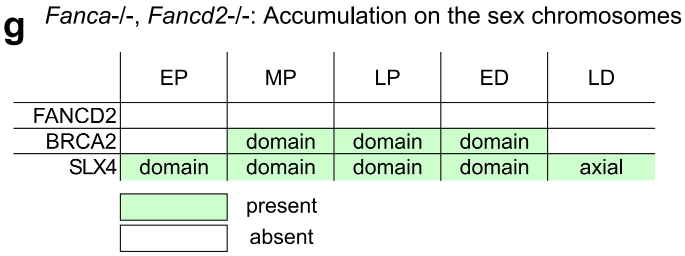

g *Fanca*-/-, *Fancd2*-/-: Accumulation on the sex chromosomes

	EP	MP	LP	ED	LD
FANCD2					
BRCA2		domain	domain	domain	
SLX4	domain	domain	domain	domain	axial

🟩 present
☐ absent

Figure 2.2: FA core-dependent and FA core-independent functions of the FA pathway.

Figure 2.2: FA core-dependent and FA core-independent functions of the FA pathway.

a–f, Immunostains using antibodies against the indicated proteins in meiotic chromosome spreads from *Fanca*$^{-/-}$ mice, *Fancd2*$^{-/-}$ mice, and wild-type littermate controls. Stages are labeled above, genotypes are labeled to the left. Dashed squares border sex chromosomes and are magnified to the right. Consistent results were obtained with n = 3 independent littermate pairs for each mouse model. Scale bars, 5 μm.

g, Summary of spatial and temporal localization of anti-FA protein antibodies on the sex chromosomes in *Fanca*$^{-/-}$ and *Fancd2*$^{-/-}$ mice; summaries of localization in wild-type mice are shown in **Figure 2.1i** and **Supplementary Figure 2.3**.

See also **Supplementary Figure 2.4**.

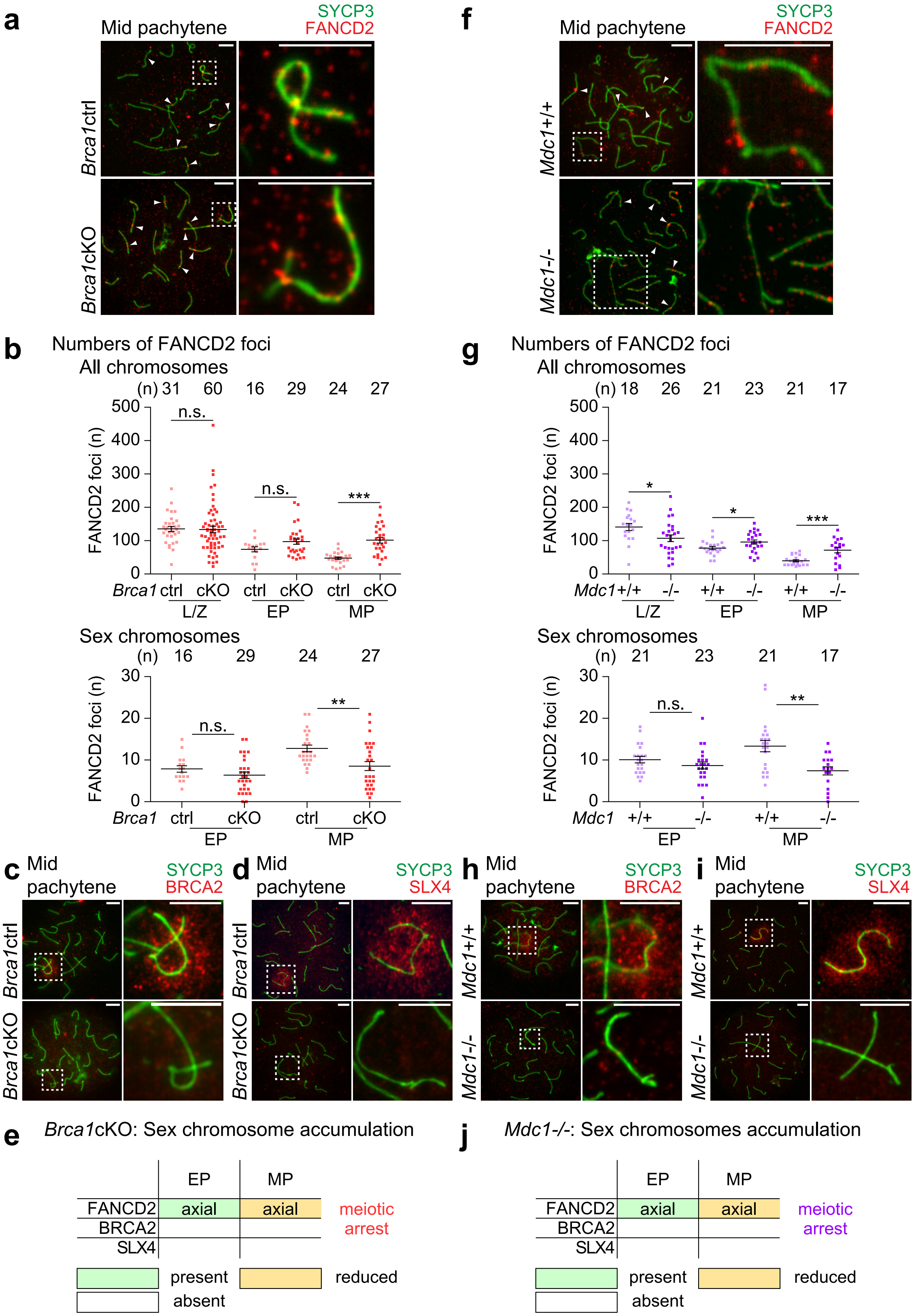

Figure 2.3: BRCA1 and MDC1 regulate the localization of FA proteins in meiosis.

Figure 2.3: BRCA1 and MDC1 regulate the localization of FA proteins in meiosis.

a, **c**, **d**, **f**, **h**, **i**, Immunostains using antibodies against the indicated proteins in meiotic chromosome spreads from *Brca1*cKO mice, *Mdc1*$^{-/-}$ mice, and wild-type or heterozygous littermate controls. Stages are labeled above; genotypes are labeled to the left. Dashed squares border sex chromosomes and are magnified to the right. Arrowheads: selected FANCD2 foci present on synapsed autosomes. Consistent results were obtained with n = 3 independent littermate pairs for each mouse model. Scale bars, 5 μm.

b, **g**, Total numbers of FANCD2 foci on all chromosome axes (top) and on the sex chromosome axes (bottom) per spermatocyte for stages of meiotic prophase. Numbers of spermatocytes analyzed are noted above each graph. Bars represent means and standard errors. Data are aggregated from n = 4 littermate pairs of *Brca1* mice, n = 3 littermate pairs of *Mdc1* mice. *P* values are derived from unpaired, two-tailed Student's t tests: n.s., not significant; $P > 0.05$; * $P \leq 0.05$; ** $P \leq 0.01$; *** $P \leq 0.001$. L/Z, leptotene and zygotene; EP, early pachytene; MP, mid pachytene.

e, **j**, Summaries of spatial and temporal localization of anti-FA protein antibodies on the sex chromosomes in *Brca1*cKO and *Mdc1*$^{-/-}$ mice; summaries of localization in wild-type mice are shown in **Figure 2.1i** and **Supplementary Figure 2.3**. Spermatocytes from the *Brca1*cKO and *Mdc1*$^{-/-}$ models undergo meiotic arrest and apoptosis after the mid pachytene stage, designated by "meiotic arrest."

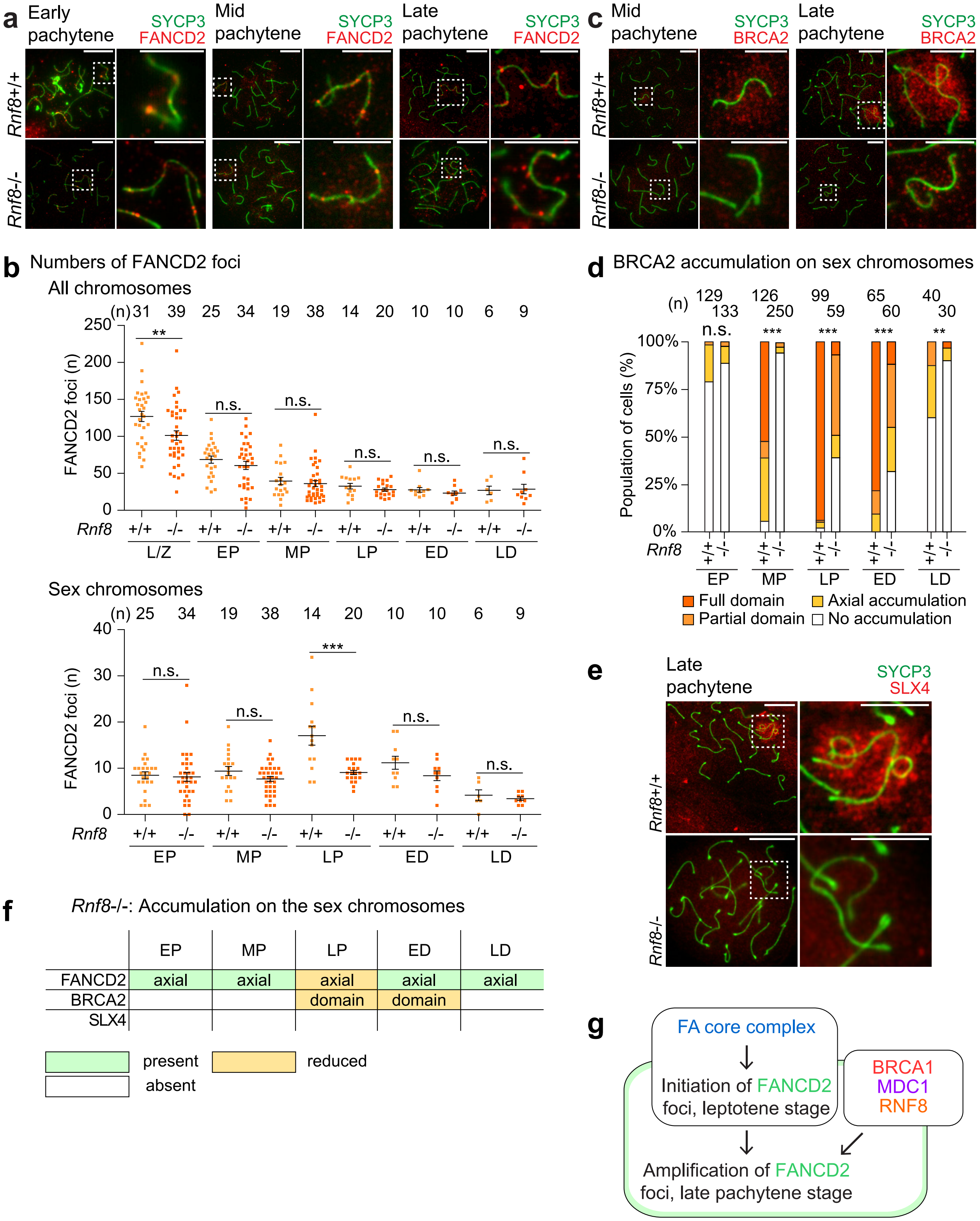

	EP	MP	LP	ED	LD
FANCD2	axial	axial	axial	axial	axial
BRCA2			domain	domain	
SLX4					

🟩 present
🟨 reduced
☐ absent

Figure 2.4: RNF8 regulates the FA-BRCA pathway.

Figure 2.4: RNF8 regulates the FA-BRCA pathway.

a, **c**, **e**, Immunostains using antibodies against the indicated proteins in meiotic chromosome spreads from *Rnf8*$^{-/-}$ mice and wild-type littermate controls. Stages are labeled above, genotypes are labeled to the left. Dashed squares border sex chromosomes and are magnified to the right. Consistent results were obtained with n = 9 independent littermate pairs. Scale bars, 5 µm.

b, Total numbers of FANCD2 foci on all chromosome axes (top) and on the sex chromosome axes (bottom) per spermatocyte for stages of meiotic prophase. Numbers of spermatocytes analyzed are noted above each graph. Bars represent means and standard errors. Data are aggregated from n = 4 littermate pairs. *P* values are derived from unpaired, two-tailed Student's t tests: n.s., not significant; $P > 0.05$; * $P \leq 0.05$; ** $P \leq 0.01$; *** $P \leq 0.001$. L/Z, leptotene and zygotene; EP, early pachytene; MP, mid pachytene; LP, late pachytene; ED, early diplotene; LD, late diplotene.

d, Categorical staining patterns for BRCA2 accumulation on sex chromosomes in pachytene and diplotene spermatocytes. Numbers of spermatocytes analyzed are noted above each graph. Accumulation patterns: Full domain, covers entirety of XY axes and chromatin; Partial domain, covers XY axes and portions of XY chromatin; Axial accumulation, covers XY axes; No accumulation, depletion from XY axes and chromatin. Data are aggregated from n = 6 littermate pairs. *P* values are derived from Pearson's chi-square test: n.s., not significant; $P > 0.05$; * $P \leq 0.05$; ** $P \leq 0.01$; *** $P \leq 0.001$.

f, Summary of spatial and temporal localization of anti-FA protein antibodies on the sex chromosomes in *Rnf8*$^{-/-}$ mice; summaries of localization in wild-type mice are shown in **Figure 2.1i** and **Supplementary Figure 2.3**.

g, Model of two-step amplification of FANCD2 foci on the sex chromosomes.

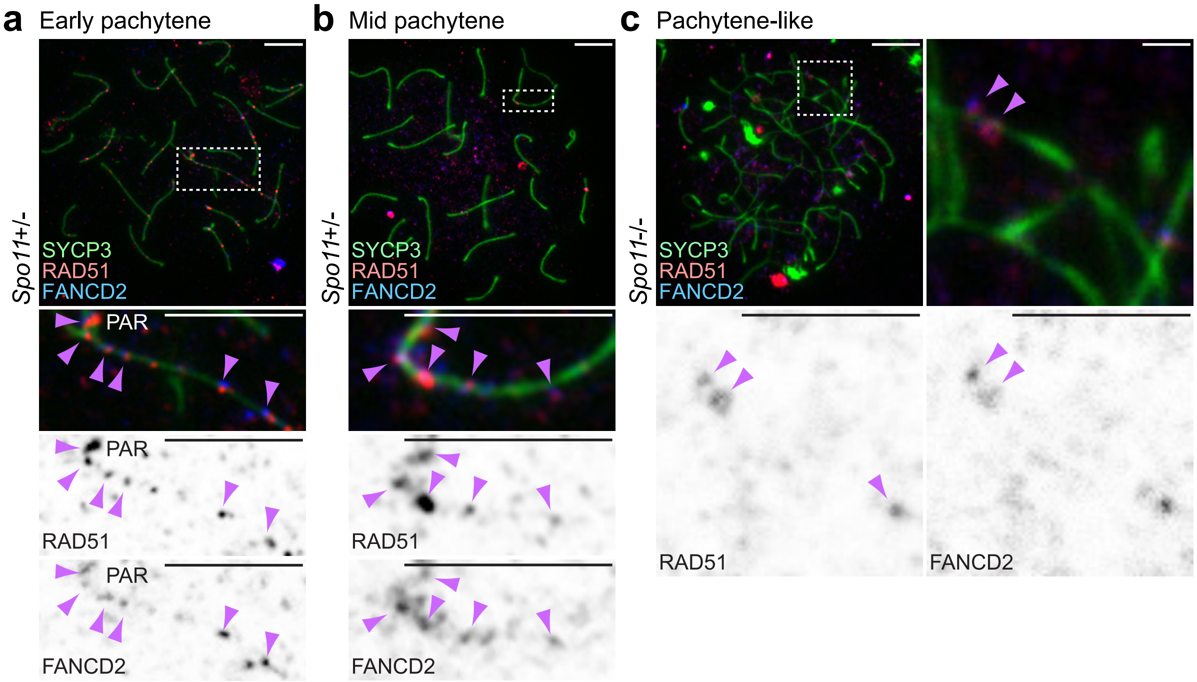

Figure 2.5: FANCD2 colocalizes with RAD51 at sites of persistent DNA double-strand breaks.

Figure 2.5: FANCD2 colocalizes with RAD51 at sites of persistent DNA double-strand breaks.

a–c, Immunostains using antibodies against the indicated proteins in meiotic chromosome spreads from *Spo11*$^{-/-}$ mice and control littermates. Stages of meiotic prophase I are labeled above images; genotypes are labeled to the left of images. Dashed boxes border selected nuclear regions and are magnified below. Arrowheads: colocalization of FANCD2 and RAD51. Consistent results were obtained with n = 3 independent littermate pairs. PAR, pseudoautosomal region. Scale bars, 5 μm.

See also **Supplementary Figure 2.5**.

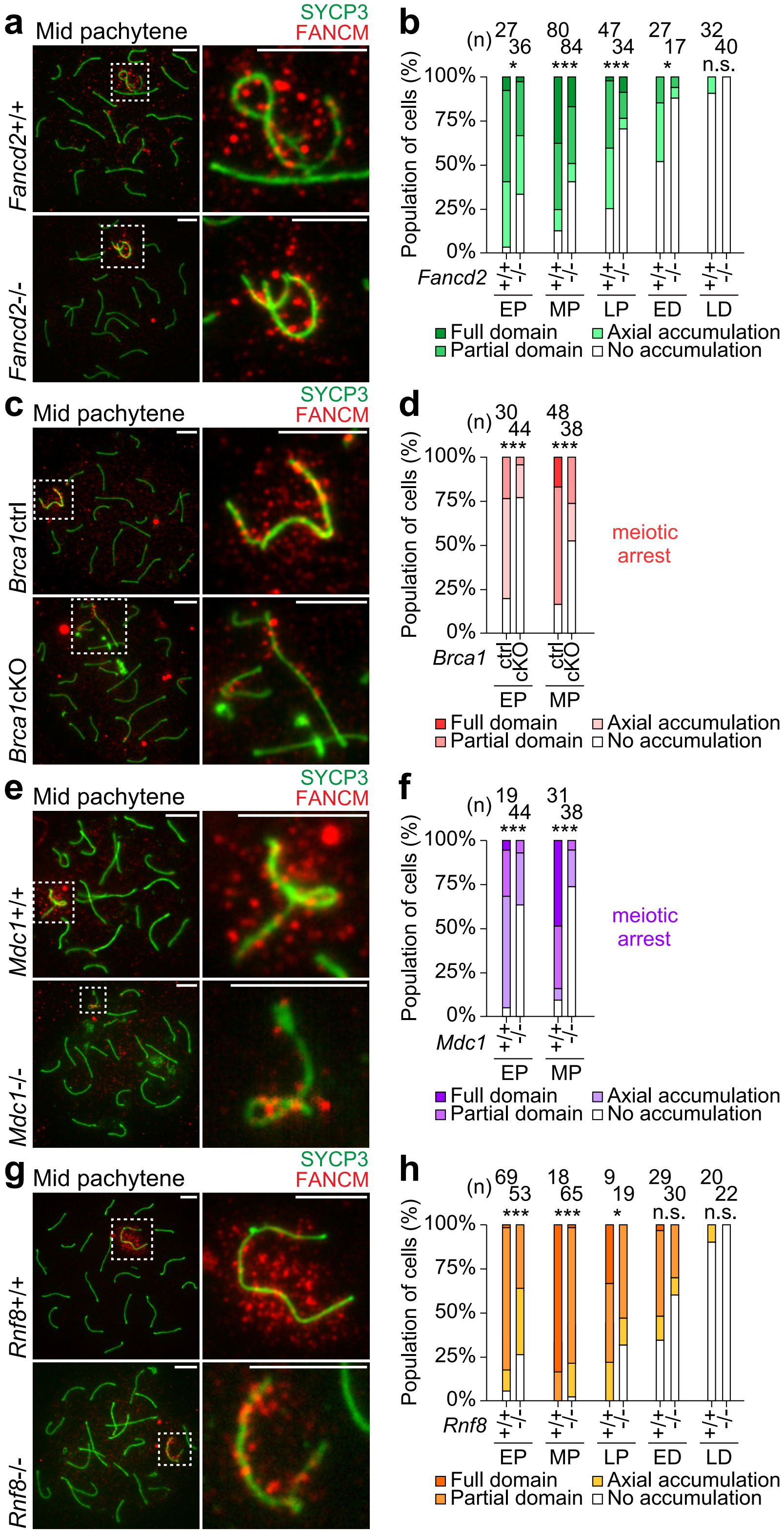

Figure 2.6: FANCD2 cooperates with the BRCA1-MDC1-RNF8 axis to regulate FANCM on the sex chromosomes.

Figure 2.6: FANCD2 cooperates with the BRCA1-MDC1-RNF8 axis to regulate FANCM on the sex chromosomes.

a, **c**, **e**, **g**, Immunostains using antibodies against the indicated proteins in meiotic chromosome from *Fancd2*$^{-/-}$ (**a**), *Brca1*cKO (**c**), *Mdc1*$^{-/-}$ (**e**), and *Rnf8*$^{-/-}$ mice (**g**), and corresponding wild-type littermate controls. Stages are labeled above; genotypes are labeled to the left. Dashed squares border sex chromosomes and are magnified to the right. Consistent results were obtained with n = 5 *Fancd2*, n = 4 *Brca1*, n = 4 *Mdc1*, and n = 4 *Rnf8* littermate pairs. Scale bars, 5 μm.

b, **d**, **f**, **h**, Categorical staining patterns for FANCM accumulation on sex chromosomes of *Fancd2* (**b**), *Brca1* (**d**), *Mdc1* (**f**), and *Rnf8* (**h**) control and mutant spermatocytes. Numbers of spermatocytes analyzed are noted above each graph. Accumulation scored according to criteria described in the legend for **Figure 2.4d**. Data are aggregated from n = 5 *Fancd2*, n = 4 *Brca1*, n = 4 *Mdc1*, and n = 4 *Rnf8* littermate pairs. *P* values are derived from Pearson's chi-square tests: n.s., not significant; $P > 0.05$; * $P \leq 0.05$; ** $P \leq 0.01$; *** $P \leq 0.001$.

See also **Supplementary Figures 2.6**, **2.7**.

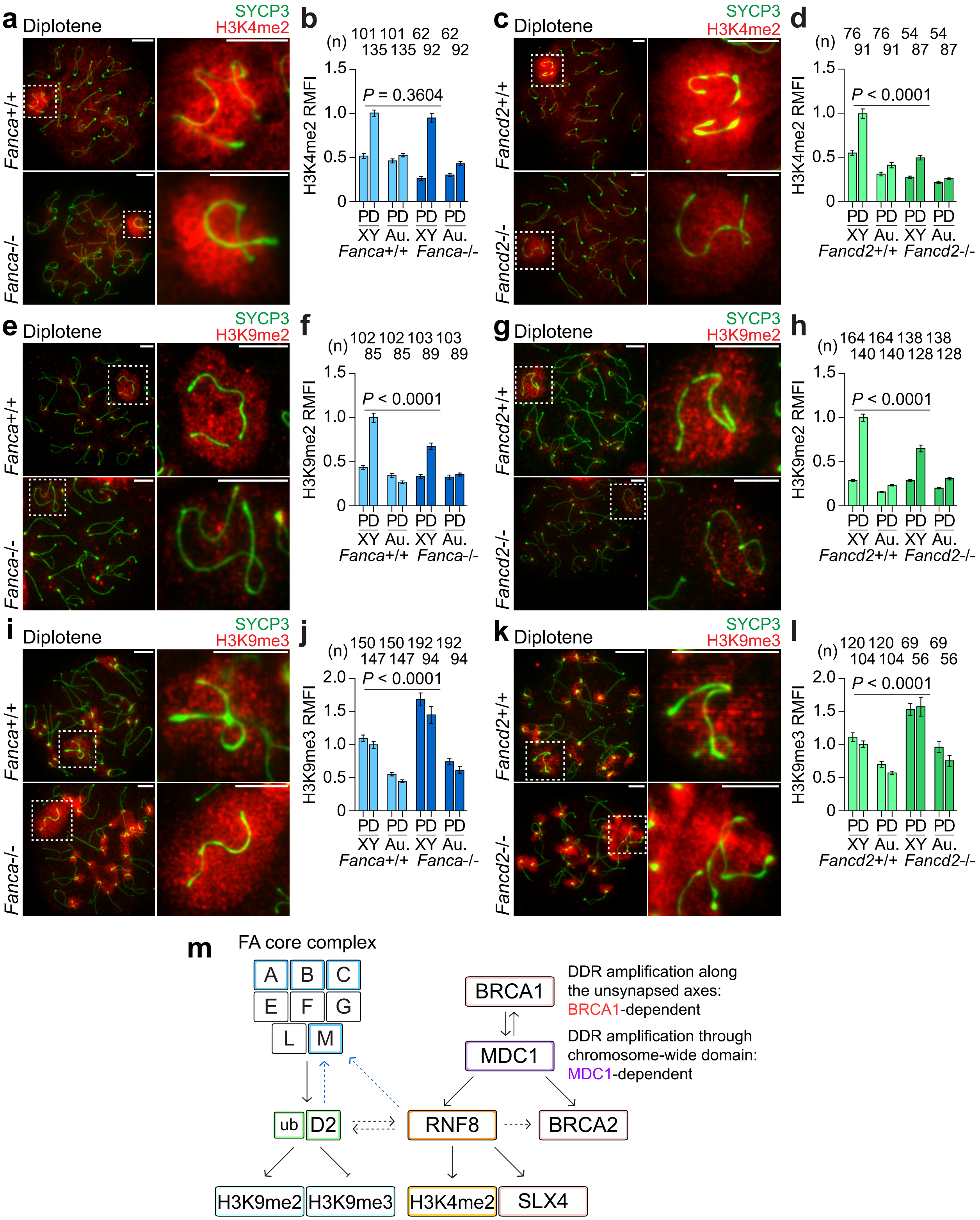

Figure 2.7: FANCD2 regulates H3K4me2 independent of FA core factors, whereas FA core factors and FANCD2 cooperate to regulate H3K9 methylation.

Figure 2.7: FANCD2 regulates H3K4me2 independent of FA core factors, whereas FA core factors and FANCD2 cooperate to regulate H3K9 methylation.

a, **c**, **e**, **g**, **i**, **k**, Immunostains using antibodies against the indicated proteins in meiotic chromosome spreads from *Fanca*$^{-/-}$ mice, *Fancd2*$^{-/-}$ mice, and corresponding wild-type littermate controls. Stages are labeled above, genotypes are labeled to the left. Dashed squares border sex chromosomes and are magnified to the right. Scale bars, 5 μm.

b, **d**, **f**, **h**, **j**, **l**, Quantifications of H3K4me2 (**b**, **d**), H3K9me2 (**f**, **h**), and H3K9me3 (**j**, **l**) relative mean fluorescence intensity (RMFI) on sex chromosomes (XY) and autosome regions (Au.) in pachytene (P) and diplotene (D) spermatocytes. Numbers of spermatocytes analyzed are noted above each graph. Bars represent means and standard errors. Data are aggregated from n = 4 *Fanca* littermate pairs (**b**, **f**, **j**), and n = 3 *Fancd2* littermate pairs (**d**, **h**, **l**). *P* values, indicated in the panels, are derived from one-way ANOVA and Tukey's method posttest.

m, Model of the FA-DDR network acting on the sex chromosomes. See the text for details.

See also **Supplementary Figures 2.8**, **2.9**.

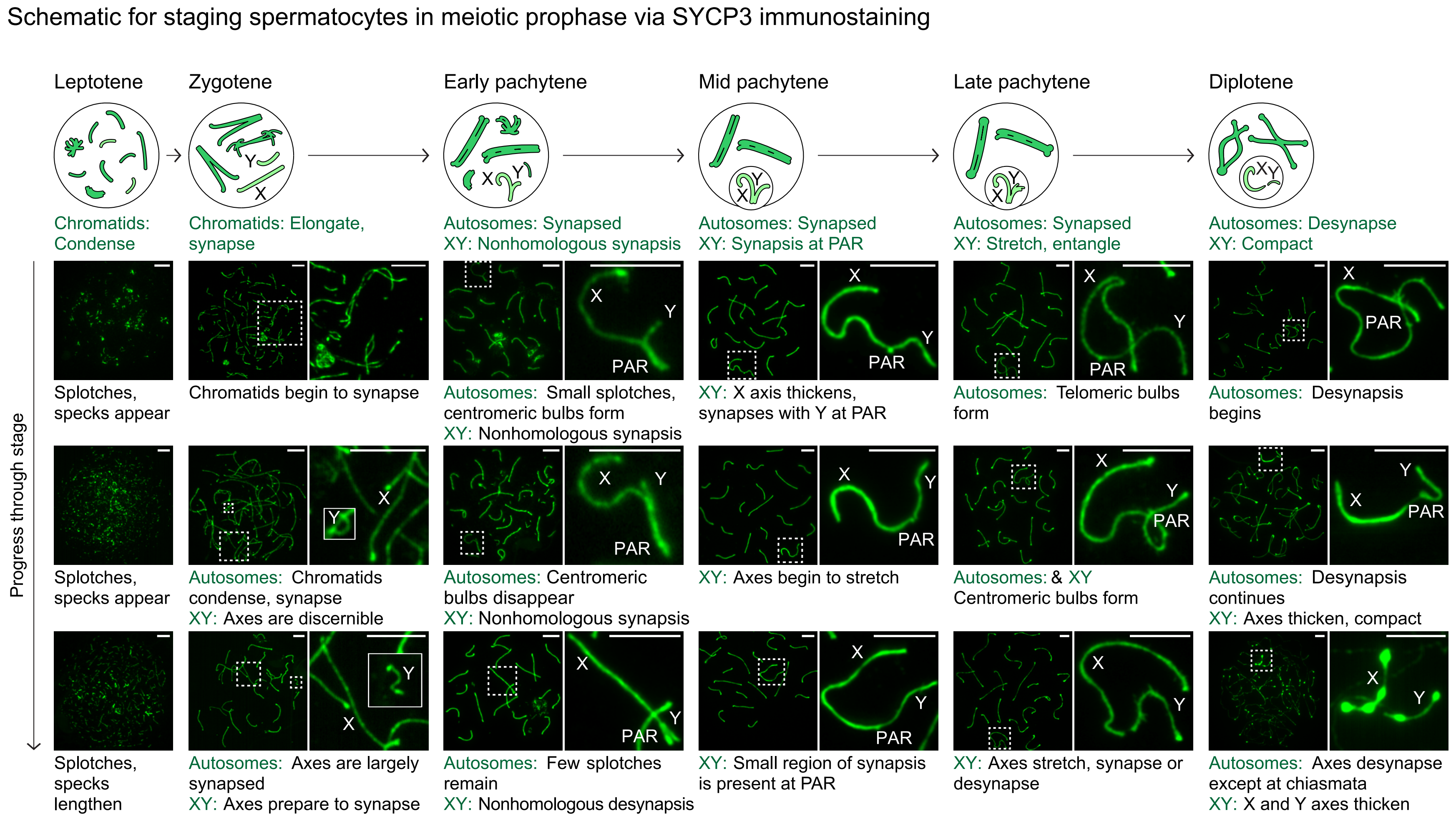

Supplementary Figure 2.1: Cytology and criteria for staging spermatocytes in meiotic prophase I via SYCP3 staining, related to Figure 2.1.

Supplementary Figure 2.1: Cytology and criteria for staging spermatocytes in meiotic prophase I via SYCP3 staining, related to Figure 2.1.

Meiotic prophase I is divided into four stages based on the presentation and synapsis of paternal and maternal chromatids, i.e., non-sister chromatids. Chromatids are the threadlike strands that chromosomes condense into during cell division. SYCP3 (shown in green), a component of the synaptonemal complex protein polymer, is essential to condensation and synapsis. Through immunofluorescent microscopy of chromosome spreads stained with anti-SYCP3 antibody, it is possible to stage spermatocytes in meiotic prophase I with a high degree of accuracy. The first stage of meiotic prophase I, the leptotene stage, sees maternal and paternal chromatids begin to condense and elongate. In the following stage, the zygotene stage, the chromatids continue to elongate and begin to synapse. The subsequent pachytene stage lasts the longest and is subdivided into three stages to account for its many appearances: the early, mid, and late pachytene stages. In the early pachytene stage, all autosomes have synapsed, and the male sex chromosomes, X and Y, undergo partial synapsis at a small region known as the pseudoautosomal region (PAR). During the early pachytene stage, XY synapsis increases until most of the Y axis is nonhomologously synapsed to X; then, as spermatocytes progress through the mid and late pachytene stages, X and Y desynapse. In the next stage of meiotic prophase I, the diplotene stage, X and Y compact while the autosomes desynapse except at specialized regions of contact known as chiasmata, where the recombination of genetic material occurs between non-sister chromatids. In the panel, the progression through stages is indicated by an arrow from top to bottom: In each column, top images represent early examples of each stage, middle images intermediate, and bottom images late. The sex chromosomes are indicated by dashed squares, and these squares are magnified in panels to the right. In the sample cytology for the zygotene stage, magnified images are inlaid. X, X chromosome; Y, Y chromosome; PAR, pseudoautosomal region. Scale bars, 5 µm.

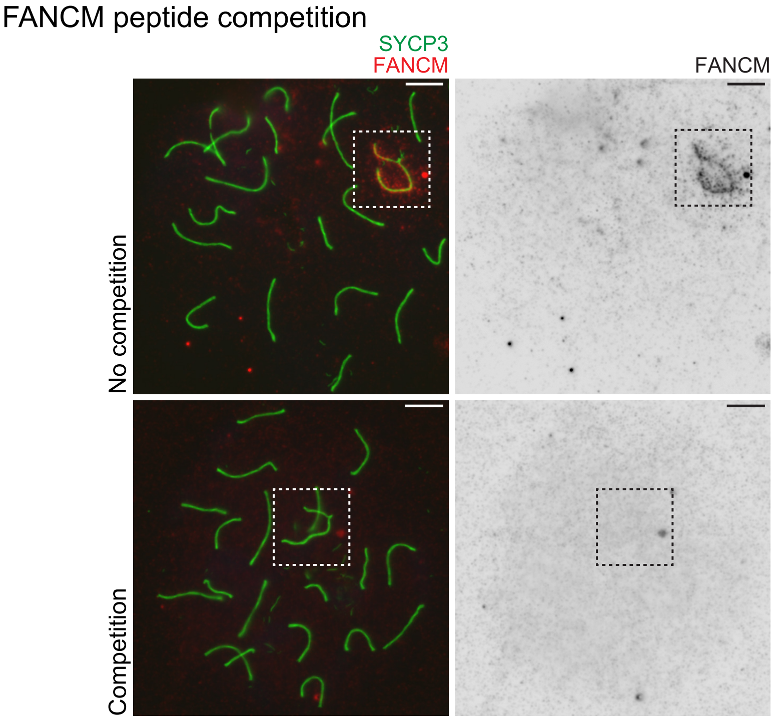

Supplementary Figure 2.2: Confirmation of anti-FANCM antibody specificity through FANCM peptide competition, related to Figure 2.1.

Supplementary Figure 2.2: Confirmation of anti-FANCM antibody specificity through FANCM peptide competition, related to Figure 2.1.

Immunostains using anti-FANCM and anti-SYCP3 antibodies in meiotic chromosome spreads from wild-type mice with and without FANCM peptide competition. Sex chromosomes are indicated by dashed squares. Consistent results were obtained with n = 3 independent wild-type mice. Scale bars, 5 μm.

Visual reference for **Figure 2.1i**, “Wild-type: Accumulation on the sex chromosomes”

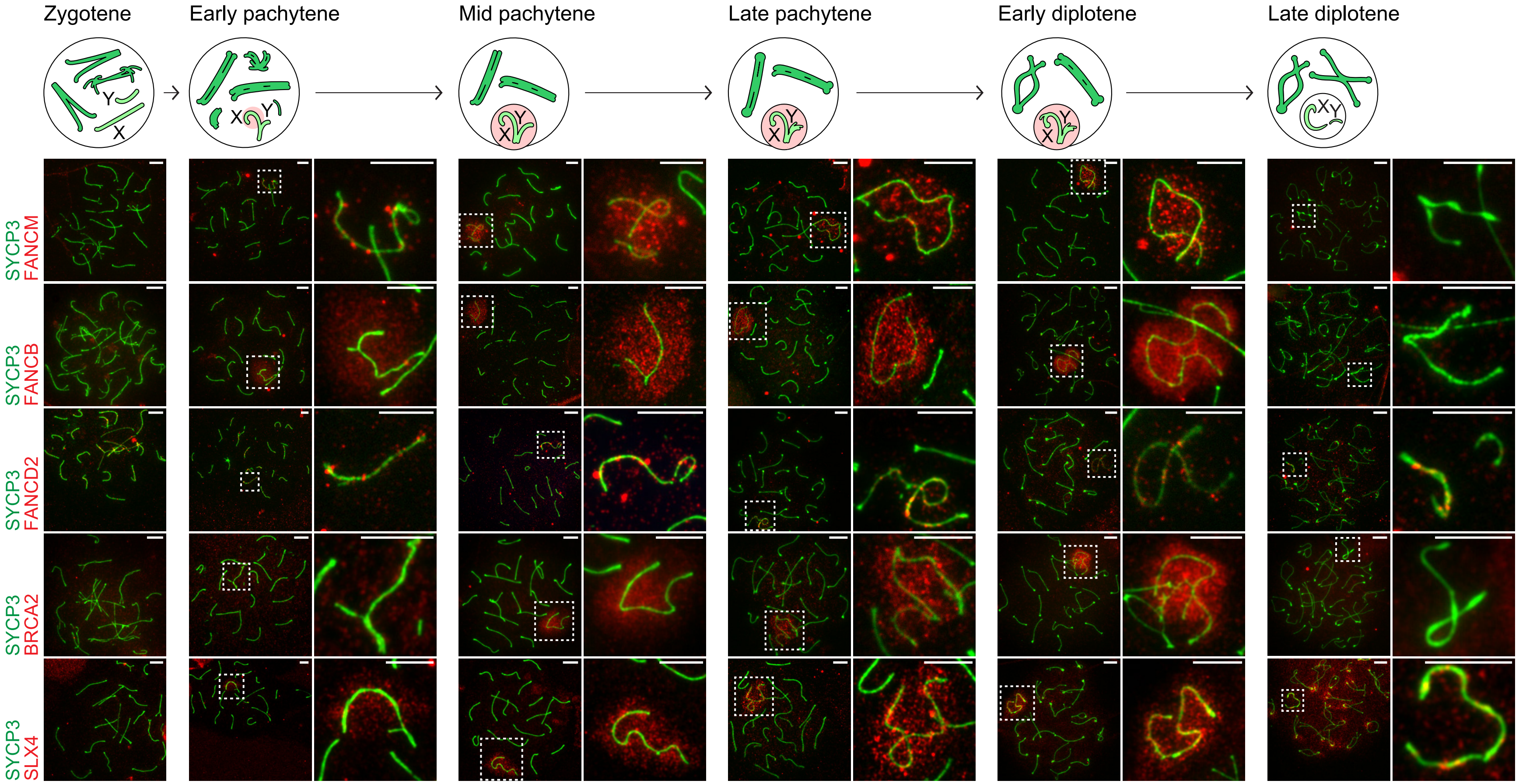

Supplementary Figure 2.3: Coordinated spatial and temporal localization of FA proteins on XY chromatin during meiotic prophase I, related to Figure 2.1.

Supplementary Figure 2.3: Coordinated spatial and temporal localization of FA proteins on XY chromatin during meiotic prophase I, related to Figure 2.1.

Representative immunostains of meiotic chromosome spreads in different stages of meiotic prophase I using anti-FANCM, anti-FANCB, anti-FANCD2, anti-BRCA2, and anti-SLX4 antibodies as designated to the left of rows. Stages of meiotic prophase I are labeled above columns. Scale bars, 5 µm.

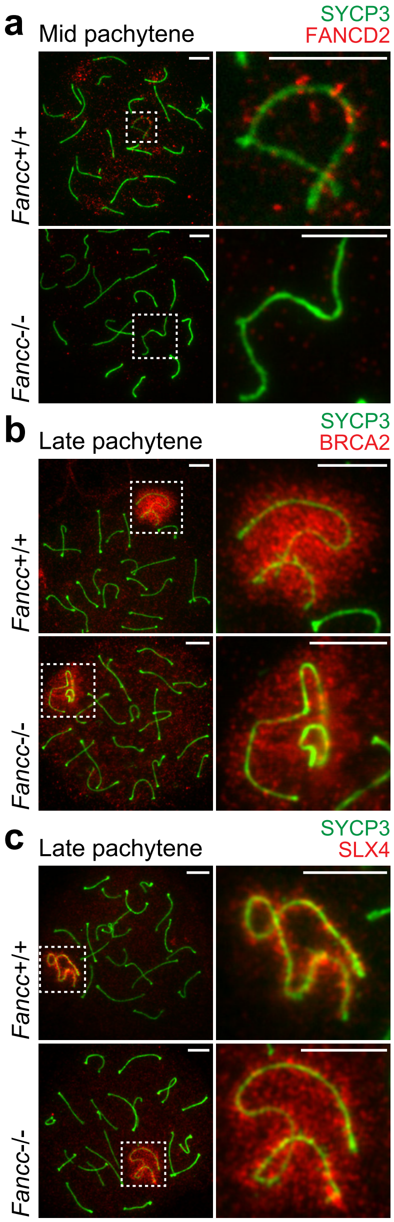

d *Fancc-/-*: Accumulation on the sex chromosomes

	EP	MP	LP	ED	LD
FANCD2					
BRCA2		domain	domain	domain	
SLX4	domain	domain	domain	domain	axial

🟩 present

□ absent

Supplementary Figure 2.4: Function of FANCC in the FA-BRCA pathway during meiosis, related to Figure 2.2.

Supplementary Figure 2.4: Function of FANCC in the FA-BRCA pathway during meiosis, related to Figure 2.2.

a–c, Immunostains using antibodies against the indicated proteins in meiotic chromosome spreads from *Fancc*$^{-/-}$ mice and wild-type littermate controls. Stages are labeled above, genotypes are labeled to the left. Dashed squares border sex chromosomes and are magnified to the right. Consistent results were obtained with n = 3 independent littermate pairs. Scale bars, 5 µm.

d, Summary of spatial and temporal localization of anti-FA protein antibodies on the sex chromosomes in *Fancc*$^{-/-}$ mice; summaries of localization in wild-type mice are shown in **Figure 2.1i** and **Supplementary Figure 2.3**.

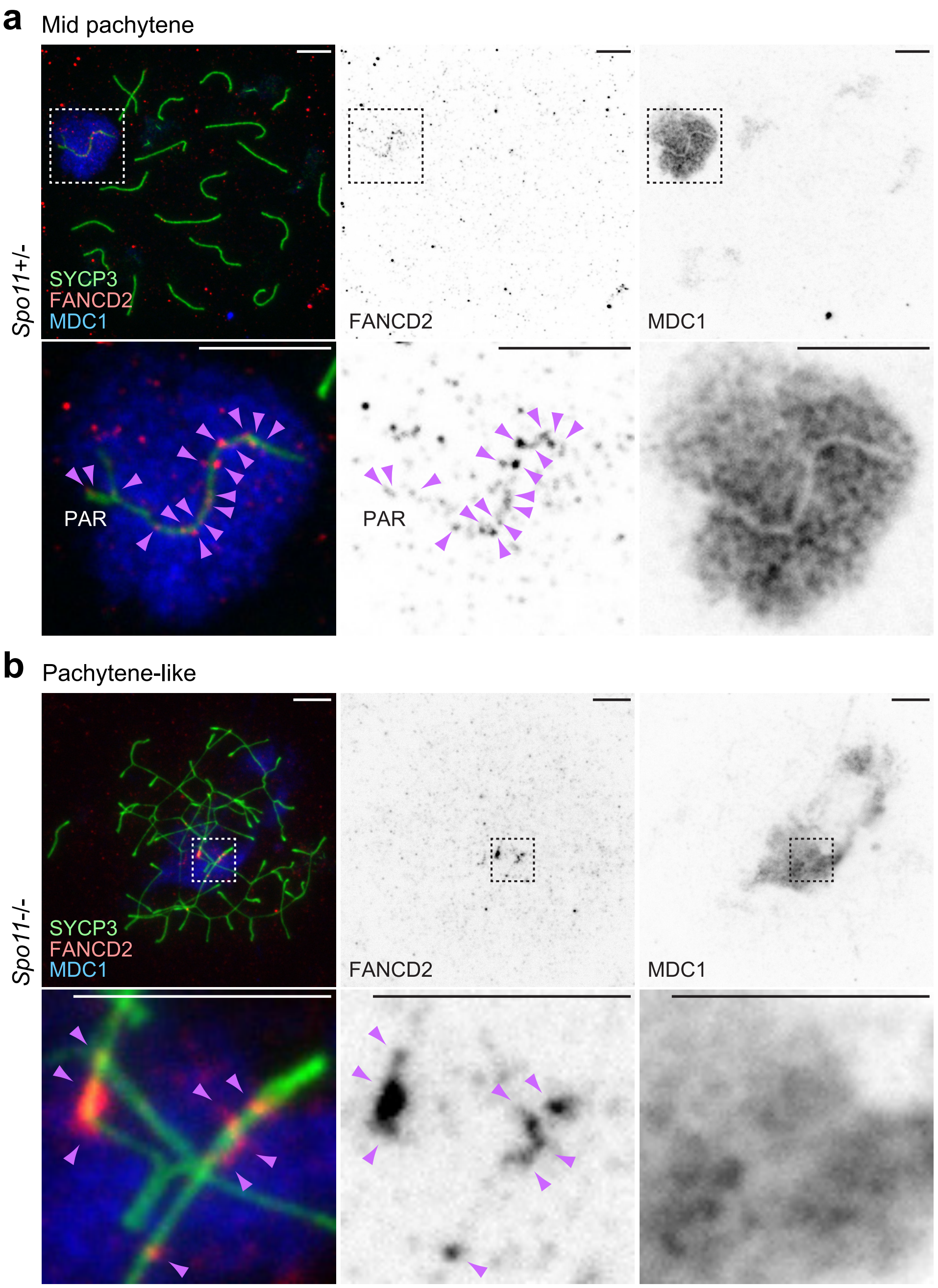

Supplementary Figure 2.5: FANCD2 foci are present in a pseudo-sex body independent of SPO11-generated DNA double-strand breaks, related to Figure 2.5.

Supplementary Figure 2.5: FANCD2 foci are present in a pseudo-sex body independent of SPO11-generated DNA double-strand breaks, related to Figure 2.5.

a, **b**, Immunostains using antibodies against the indicated proteins in meiotic chromosome spreads from *Spo11*$^{-/-}$ mice and control littermates. Stages are labeled above, genotypes are labeled to the left. Dashed boxes border selected nuclear regions and are magnified below. Arrowheads: colocalization of FANCD2 and MDC1. Consistent results were obtained with n = 3 independent littermate pairs. PAR, pseudoautosomal region. Scale bars, 5 μm.

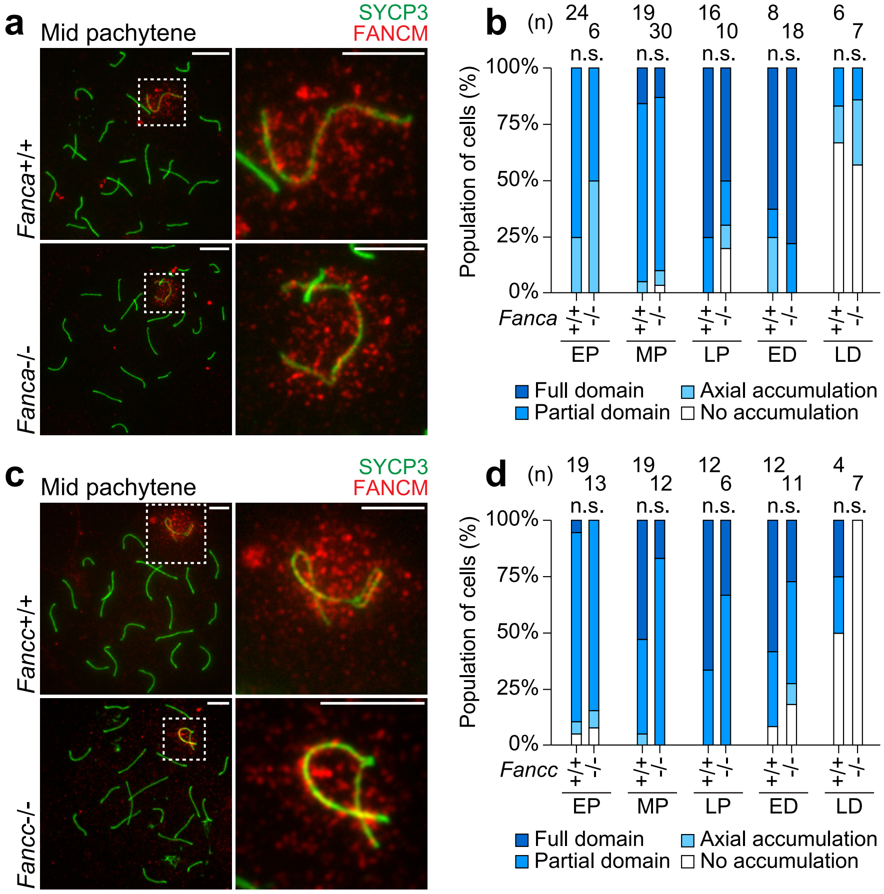

Supplementary Figure 2.6: The FA core complex is dispensable for the regulation of FANCM, related to Figure 2.6.

Supplementary Figure 2.6: The FA core complex is dispensable for the regulation of FANCM, related to Figure 2.6.

a, **c**, Immunostains using antibodies against the indicated proteins in meiotic chromosome spreads from *Fanca*$^{-/-}$ (**a**) and *Fancc*$^{-/-}$ (**c**) mice, and corresponding wild-type littermate controls. Stages are labeled above, genotypes are labeled to the left. Dashed squares border sex chromosomes and are magnified to the right. Consistent results were obtained with n = 4 independent littermate pairs for each model. Scale bars, 5 μm.

b, **d**, Categorical staining patterns for FANCM accumulation on sex chromosomes of *Fanca* (**b**) and *Fancc* (**d**) control and mutant spermatocytes. Numbers of spermatocytes analyzed are noted above each graph. Accumulation was scored according to criteria described in the legend for **Figure 2.4d**. Data are aggregated from n = 3 littermate pairs for each model. *P* values are derived from Pearson's chi-square tests: n.s., not significant.

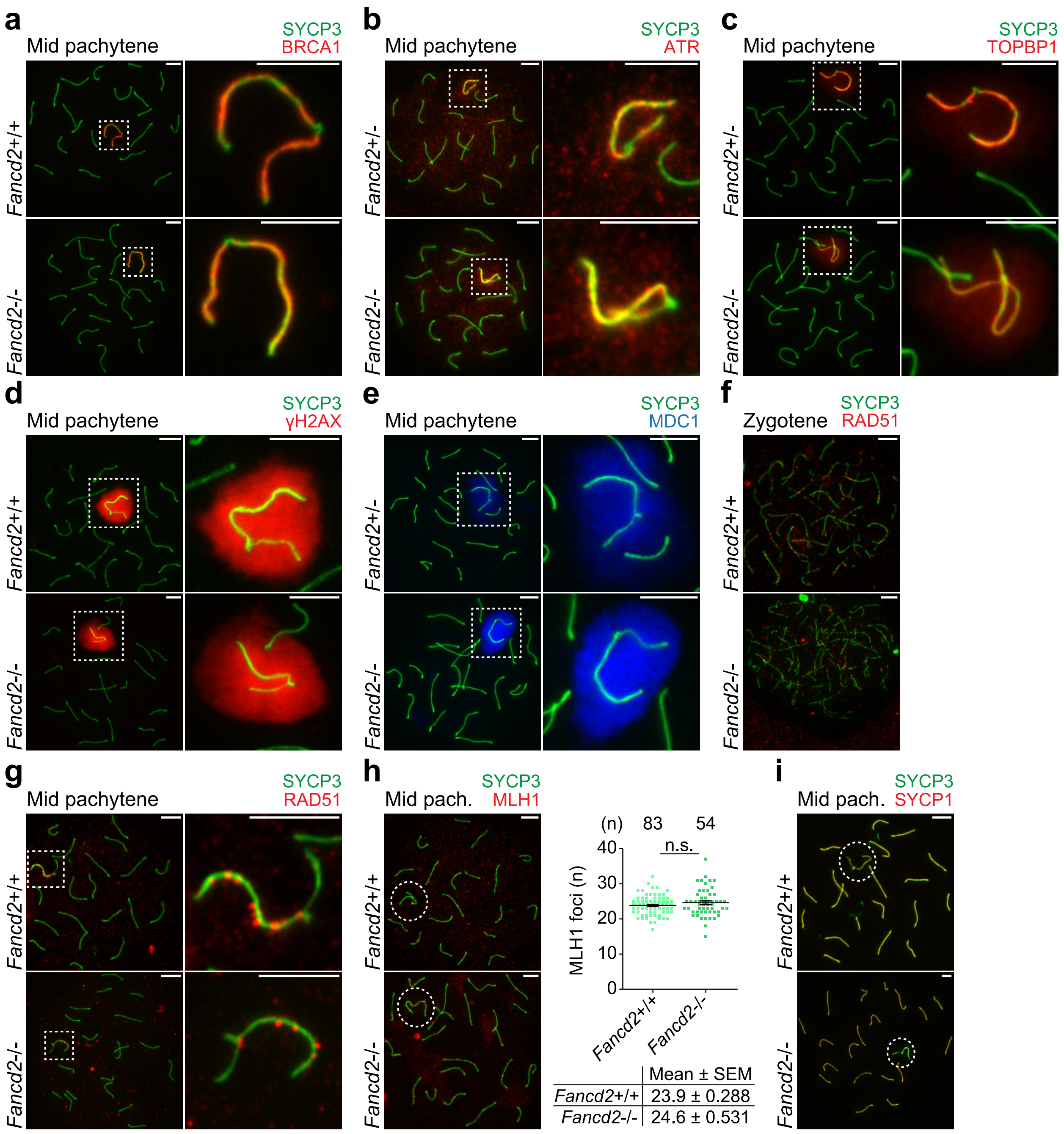

Supplementary Figure 2.7: Regulation of DNA damage response factors and recombination factors on the sex chromosomes in *Fancd2* mutant mice, related to Figure 2.6.

Supplementary Figure 2.7: Regulation of DNA damage response factors and recombination factors on the sex chromosomes in *Fancd2* mutant mice, related to Figure 2.6.

a–i, Immunostains using antibodies against the indicated proteins in meiotic chromosome spreads from *Fancd2*$^{-/-}$ mice and wild-type or heterozygous littermate controls. Stages are labeled above, genotypes are labeled to the left. Dashed squares border sex chromosomes and are magnified to the right. Dashed circles border the sex chromosomes in (**h**, **i**). Consistent results were obtained with n = 3 independent littermate pairs. Scale bars, 5 µm.

h, Bars represent means and standard errors. Data are aggregated from n = 3 littermate pairs of wild-type and mutant *Fancd2* mice. *P* values are derived from an unpaired, two-tailed Student's t test: n.s., not significant; $P > 0.05$.

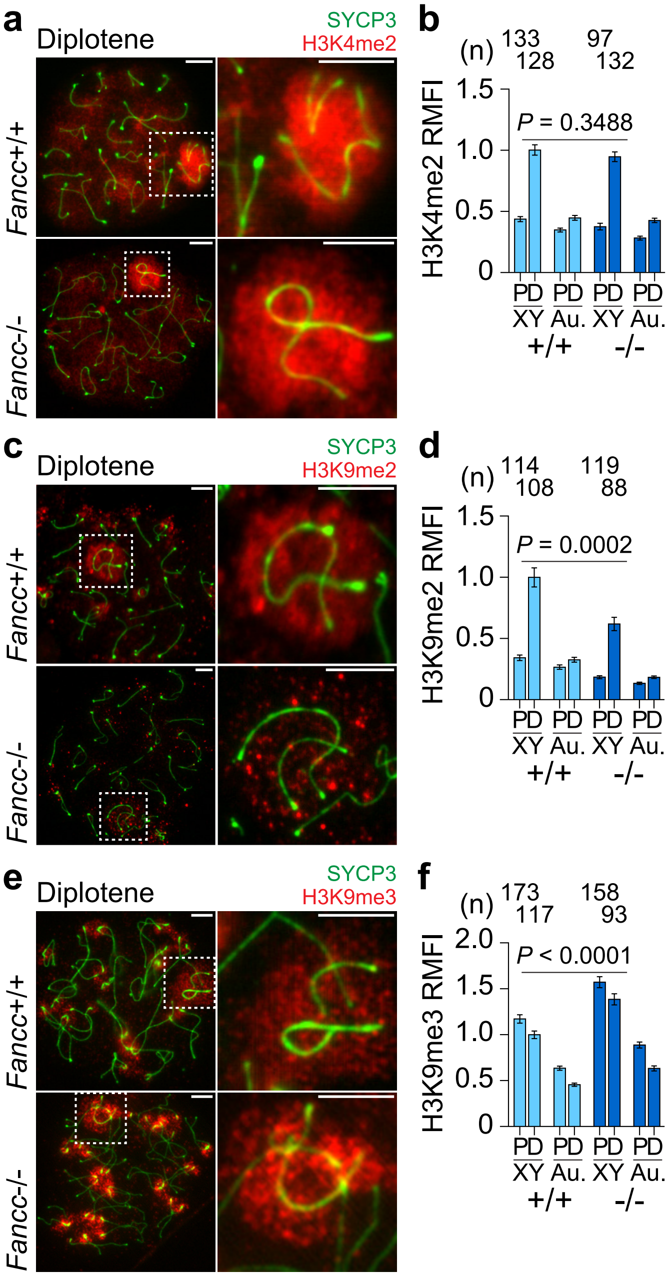

Supplementary Figure 2.8: FANCC regulates H3K9 methylation, related to Figure 2.7.

Supplementary Figure 2.8: FANCC regulates H3K9 methylation, related to Figure 2.7.

a, **c**, **e**, Immunostains using antibodies against the indicated proteins in meiotic chromosome spreads from *Fancc*$^{-/-}$ mice and corresponding wild-type controls. Stages are labeled above, genotypes are labeled to the left. Dashed squares border sex chromosomes and are magnified to the right. Scale bars, 5 µm.

b, **d**, **f**, Quantifications of H3K4me2 (**b**), H3K9me2 (**d**), and H3K9me3 (**f**) relative mean fluorescence intensity (RMFI) on sex chromosomes (XY) and autosome regions (Au.) in pachytene (P) and diplotene (D) spermatocytes. Numbers of spermatocytes analyzed are noted above each graph. Bars represent means and standard errors. Data are aggregated from n = 3 independent littermate pairs of wild-type and *Fancc*$^{-/-}$ mice. *P* values, indicated in the panels, are derived from one-way ANOVA and Tukey's method posttest.

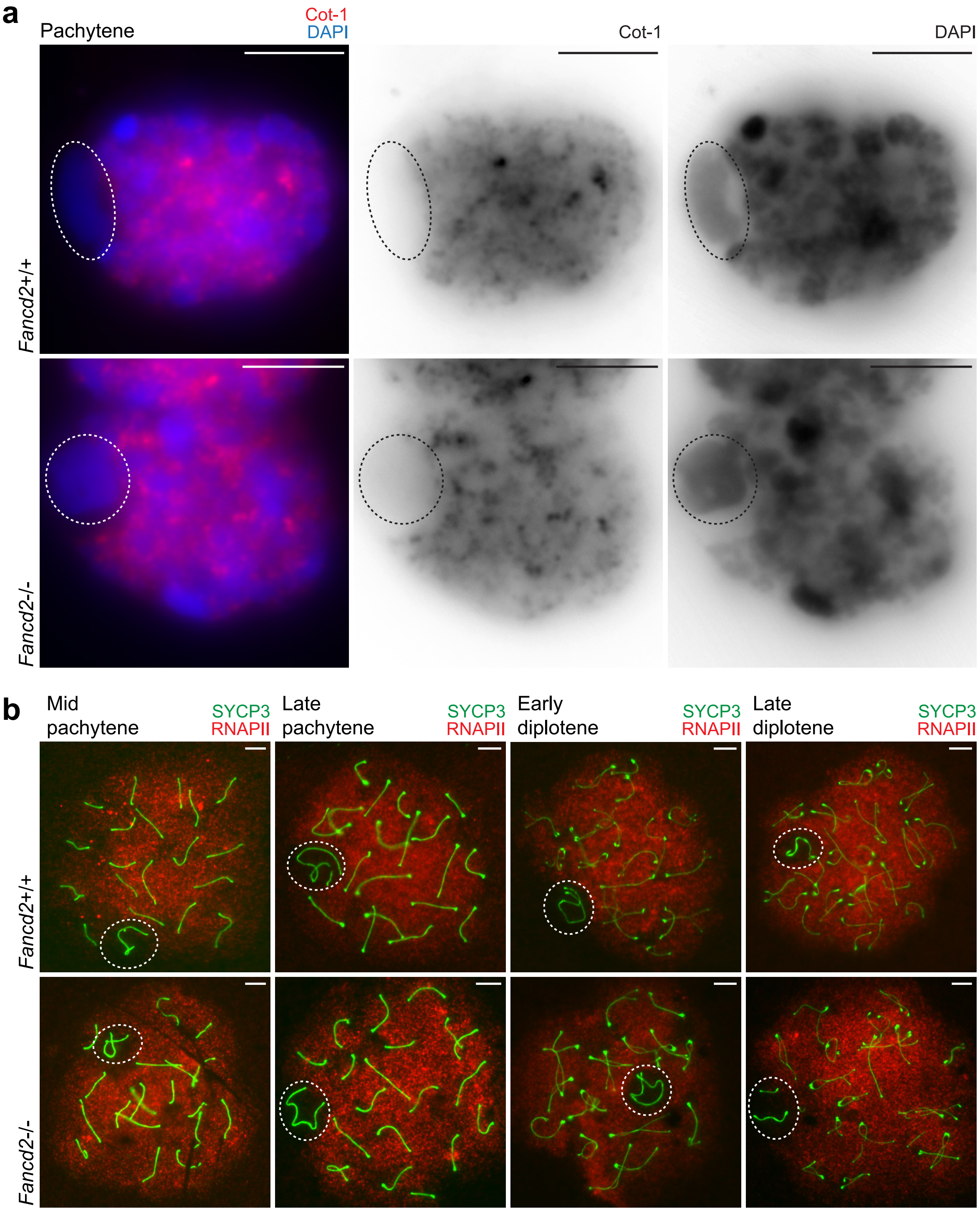

Supplementary Figure 2.9: Large-scale detection of transcription remains unchanged in *Fancd*2 mutants, related to Figure 2.7.

Supplementary Figure 2.9: Large-scale detection of transcription remains unchanged in *Fancd2* mutants, related to Figure 2.7.

a, Cot-1 RNA FISH (red signal) and DAPI (blue signal) in pachytene spermatocytes from *Fancd2*$^{-/-}$ and wild-type littermate control slides that maintain the three-dimensional architecture of nuclei (3D slides; **Materials & Methods**).

b, Immunostains of meiotic chromosome spreads using antibodies against the indicated proteins in *Fancd2*$^{-/-}$ mice and wild-type littermate controls.

a, **b**, Consistent results were obtained with n = 3 independent littermate pairs of mice. Dashed circles border and denote the XY chromatin. Scale bars, 5 μm.

Chapter 3

Attenuated chromatin compartmentalization in meiosis and its maturation in sperm development

Kris G. Alavattam[1,2,3], So Maezawa[2,3,4], Akihiko Sakashita[2,3], Haia Khoury[5], Artem Barski[3,6], Noam Kaplan[5,7,*], and Satoshi H. Namekawa[2,3,7,*]

[1]Graduate Program in Cancer and Cell Biology, Department of Cancer Biology, University of Cincinnati College of Medicine, Cincinnati, OH, USA

[2]Division of Reproductive Sciences, Division of Developmental Biology, Perinatal Institute, Cincinnati Children's Hospital Medical Center, Cincinnati, OH, USA

[3]Department of Pediatrics, University of Cincinnati College of Medicine, Cincinnati, OH, USA

[4]Department of Animal Science and Biotechnology, School of Veterinary Medicine, Azabu University, Sagamihara, Kanagawa, Japan

[5]Department of Physiology, Biophysics & Systems Biology, Rappaport Faculty of Medicine, Technion - Israel Institute of Technology, Haifa, Israel

[6]Division of Allergy and Immunology, Division of Human Genetics, Cincinnati Children's Hospital Medical Center, Cincinnati, OH, USA

[7]These authors jointly supervised this work: Noam Kaplan, Satoshi H. Namekawa.

[*]Correspondence: noam.kaplan@technion.ac.il; satoshi.namekawa@cchmc.org

Published in *Nat Struct Mol Biol*. 2019 Mar;26(3):175-184.

https://doi.org/10.1038/s41594-019-0189-y

(See reference[2].)

Abstract

Germ cells manifest a unique gene expression program and regain totipotency in the zygote. Here, we perform Hi-C analyses to examine 3D chromatin organization in male germ cells during spermatogenesis. We show that the highly compartmentalized 3D chromatin organization characteristic of interphase nuclei is attenuated in meiotic prophase I. Meiotic prophase I is predominated by short-range intrachromosomal interactions that represent a condensed form akin to that of mitotic chromosomes. However, unlike mitotic chromosomes, meiotic chromosomes display weak genomic compartmentalization, weak topologically associating domains, and localized point interactions. Genomic compartmentalization increases in postmeiotic round spermatids, giving rise to the strong compartmentalization seen in mature sperm. The X chromosome lacks domain organization during meiotic sex chromosome inactivation. We propose that male meiosis occurs amid the global reprogramming of 3D chromatin organization and that strengthening of chromatin compartmentalization takes place in spermiogenesis to prepare the next generation of life.

Introduction

The germline is the sole lineage supporting the perpetuity of life. Its unique potential to recover totipotency is defined by chromatin mechanisms. Using genome-wide chromosome conformation capture (Hi-C), recent studies have suggested that sperm has highly compartmentalized 3D chromatin organization that resembles the interphase nuclei of embryonic cells[13,16,166,167]. This raises the possibility that some aspects of paternal chromatin organization may be predetermined in sperm prior to embryonic development.

The hallmark of germline development is meiosis, when the germ cell genome goes through recombination to facilitate genetic diversity in offspring[54,56]. In late spermatogenesis, germ cells undergo cellular reconstruction and global chromatin remodeling that ultimately gives rise to functional sperm[8]. Beginning in meiosis, global transcription networks are altered by the activation of germline-specific genes, and this process continues in postmeiotic spermatids[3,69,82,83]. As a result, the testis has the most diverse and complex transcriptomes of all organs[6]. However, it remains unknown how the spatiotemporal organization of germ cell chromatin facilitates vital gene expression programs and sets the epigenetic state for the next generation of life.

By performing Hi-C on representative stages of male germ cells from mice, we found that meiosis occurs amid the attenuated compartmentalization of 3D chromatin organization; this compartmentalization is strengthened in haploid spermatids, giving rise to highly compartmentalized 3D chromatin organization in mature sperm. Our study suggests that the attenuated chromatin compartmentalization in male meiosis underlies complex germline transcriptomes and prepares for the next generation of life.

Results

The 3D chromatin organization of meiotic spermatocytes and post-meiotic spermatids. To determine the 3D chromatin organization of germ cells in late spermatogenesis, we isolated representative cell types from C57Bl/6J mice and performed Hi-C experiments. Our analyses focused on pachytene spermatocytes, which are in the midst of meiotic prophase I and the synapsis of homologous chromosomes, and round spermatids, which are haploid cells resulting from the second meiotic division (**Figure 3.1a**). These two stages are accompanied by high levels of gene expression[69], last about one week each during spermatogenic differentiation, and represent a majority of testicular germ cells. In isolating these cells, we confirmed their high purity (**Supplementary Figure 3.1**; **Supplementary Dataset 1**), consistent with our previous studies[82,90]. In addition to our processed Hi-C datasets (**Supplementary Dataset 2**; **Materials & Methods**), we reanalyzed a published dataset for mature sperm[167]. To provide a reference point for the analyses of spermatogenesis datasets, we also reanalyzed a mouse embryonic stem cell (ESC) dataset[168]. A recent study demonstrated that sperm has highly compartmentalized 3D chromatin organization that resembles the 3D chromatin organization of ESCs[167]. Although it was not possible using these data to distinguish the homologous chromosomes or sister chromatids characteristic of pachytene spermatocytes, we were able to evaluate the global features of 3D chromatin organization in each dataset.

First, we compared general features of pachytene spermatocyte genome organization with those of sperm and ESCs. Interaction maps of pachytene spermatocytes revealed atypical forms of higher-order chromatin organization in comparison to previous studies of interphase nuclei, sperm, and ESCs[169,170]. Consistent with chromosome condensation and the synapsis of homologous chromosomes, we detected an abundance of “near” intrachromosomal interactions (strong interactions along the diagonal of the PS panel in **Figure 3.1b**) relative to sperm and ESCs. In this respect, pachytene spermatocyte chromosomes bore resemblance to somatic mitotic chromosomes (prometaphase mitosis human foreskin fibroblasts)[171] as well as the chromosomes of oocytes arrested in metaphase of meiosis II (MII oocytes)[13] (**Supplementary Figure 3.2a**).

Next, we examined the intrachromosomal contact probability *P(s)* for pairs of genomic loci stratified by genomic distance *s*, which may be indicative of the general polymer state of chromatin[172,173]. In sperm and interphase chromosomes, intrachromosomal contact probability has been reported to follow a power law of $P(s) \sim s^{-1}$, which may be consistent with a fractal globule state[172,173]. In contrast, the chromosomes in pachytene spermatocytes displayed a gradual decrease in intrachromosomal contact probability, following a power law of $P(s) \sim s^{-0.61}$ at genomic distances up to 3 Mb (**Figure 3.1c**), followed by a steep drop in contact probability at larger distances. Of note, the chromatin in pachytene spermatocytes bore resemblance to that observed in mitotic chromosomes. Consistent with previous studies[171,174], mitotic chromosomes displayed a power-law decay of $P(s) \sim s^{-0.49}$ at distances up to 10 Mb, followed by a drop at larger distances; this has been suggested to be consistent with the presence of randomly anchored loop arrays[171,174]. The pachytene spermatocyte pattern also closely matched that observed for MII oocyte chromosomes: $P(s) \sim s^{-0.60}$ for distances up to 3 Mb, followed by a decrease in contact probability (**Figure 3.1d**). Together, these observations are in line with the overall condensed form shared by meiotic and mitotic chromosomes.

To investigate the dynamics of chromatin organization after meiosis, we studied Hi-C interaction maps of round spermatids. Round spermatid data were found to reflect an intermediate state between pachytene spermatocytes and mature sperm (**Figure 3.1b**, **3.1c**, **3.1e**), with more long-range interactions than pachytene spermatocytes but less than sperm. Following round spermatids, mature sperm evinced highly compartmentalized 3D chromatin (**Figure 3.1b**, **3.1e**). These results suggest that the large-scale structure of meiotic chromosomes in pachytene spermatocytes resembles that of mitotic chromosomes, with round spermatid chromatin presenting an intermediate state in the development towards mature sperm.

Attenuated compartmentalization of 3D chromatin organization in meiosis. Hi-C maps of interphase genomes often evince plaid patterns of chromatin interactions known as genomic compartments[173,175,176]. These have been interpreted as at least two alternating states of chromatin, A and B, in which each state preferentially interacts with other loci of the same state.

Genomic compartments have been shown to be strongly associated with biological features such as the epigenetic states of chromatin (A, active/euchromatin; B, inactive/heterochromatin) and gene expression (A, expressed; B, silenced). In order to accentuate genomic compartments, we normalized the intrachromosomal interaction maps by genomic distance and then calculated Pearson correlation matrices. In contrast to somatic mitotic chromosomes and MII oocytes, which do not show evidence of genomic compartments[13,16,171,174,177,178] (**Supplementary Figure 3.2b**), genomic compartments were observed in both pachytene spermatocytes and round spermatids (**Figure 3.2a**). Intriguingly, these compartments were attenuated relative to the compartments in sperm and ESCs (**Figure 3.2a**).

Next, we sought to quantify the degree to which the genomic compartment signal appears in the data. Genomic compartments are usually detected by applying principal component analysis (PCA) to Pearson correlation matrices and extracting the first eigenvector (EV1), where the sign indicates the state (A/B) of loci (**Supplementary Dataset 3**). However, PCA is not appropriate to quantify the degree of compartment signal due to its relative sensitivity to noise and insensitivity to scale. Thus, we used a new approach to quantify the genomic compartment signal. Briefly, given some vector that indicates genomic compartment values (e.g., EV1), we selected loci with the highest 25% (strongest A) and lowest 25% (strongest B) of values, and calculated the strength of A-A and B-B interactions relative to A-B interactions (**Materials & Methods**). We refer to this quantity as “genomic compartment strength”, and we verified that it can accurately quantify the degree of genomic compartment signal by mixing fixed proportions of the mature sperm Hi-C map, which shows strong genomic compartmentalization, with an interaction map that has no genomic compartments (**Supplementary Figure 3**; **Supplementary Dataset 3**). Using this approach, we verified that the attenuated compartmentalization observed in pachytene spermatocytes is probably not due to contamination by heterogeneous cells (**Supplementary Figure 1**; **Supplementary Dataset 1**); furthermore, we verified that genomic compartment strength in round spermatids indicates an intermediate status between pachytene spermatocytes and sperm (**Figure 3.2b**). Finally, as expected, we found that genomic compartments, as captured by EV1 (**Supplementary Dataset 3**), are correlated with both gene expression (RNA-seq signals) and chromatin state (ChIP-seq signals)[173] (**Figure 3.2c**; **Supplementary Figure 3.4**). Together, our data indicate that fundamental forms of genomic compartmentalization, similar to those found in interphase, are present but attenuated in male meiosis. These features are maintained and strengthened in the transition from meiotic to postmeiotic germ cells, despite an overall dramatically different nuclear organization.

Interchromosomal interactions in late spermatogenesis. Next, we sought to answer the following question: Does our Hi-C data recapitulate key features of chromosome organization in meiosis and spermatids? In pachytene spermatocytes, homologous chromosomes have undergone synapsis, whereas chromosomes that are nonhomologous are separated from each other[179]. Consistent with the separation of nonhomologous chromosomes during prophase, a low proportion of interchromosomal interactions in pachytene spermatocytes relative to sperm and ESCs was observed (**Supplementary Figure 3.5**; **Supplementary Dataset 2**). In order to accentuate interchromosomal interaction signals, we scaled the interaction matrix of each interchromosomal pair into a square matrix and calculated an average interchromosomal interaction frequency matrix over all such chromosome pairs (**Materials & Methods**). We found frequent interchromosomal interactions between the acrocentric ends of chromosomes (telomeres proximal to centromeres) during meiosis as well as the interchromosomal association of non-centromeric ends (telomeres distal to centromeres) (**Figure 3.3a**). These features may be due to the anchoring of telomeres to the nuclear membrane during meiosis (**Figure 3.3b**). Studies using microscopy demonstrated that, during meiotic prophase I, both chromosome ends attach to the nuclear membrane[180] and, in particular, the acrocentric ends tend to associate because of the frequent association of pericentromeric heterochromatin[181]. Our Hi-C results are consistent with these microscopic observations.

This association of pericentromeric heterochromatin culminates in a single chromocenter in round spermatids, and this chromocenter persists into sperm (**Figure 3.1a**). Consistent with this feature, we found that the acrocentric ends of chromosomes tended to associate in round spermatids and, to a lesser extent, in sperm (**Figure 3.3a** and the model shown in **Figure 3.3c**; direct interactions between centromeres were not observed due to technical limitations related to sequencing highly repetitive regions of DNA). These general features were also observable, to a lesser degree, when examining pairs of individual chromosomes (for example, chromosomes 2 and 4 in **Figure 3.3d**), as were interchromosomal interactions of genomic compartments (**Figure 3.3d**). Intriguingly, we observed the strongest interchromosomal interactions between those of genomic A compartments, which are gene-rich and abundant in active histone modifications (**Figure 3.2c**), and which persist throughout spermatogenesis and in ESCs (**Figure 3.3d**). And, as with intrachromosomal interactions in round spermatids, we observed an increased proportion of interchromosomal interactions in round spermatids relative to pachytene spermatocytes (**Figure 3.3e**). By measuring genomic compartment strength, we confirmed that interchromosomal genomic compartments are also present in pachytene spermatocytes (**Figure 3.3f**). These results are surprising, because they suggest that interactions associated with chromatin state are present between chromosomes in spite of their condensed form. Together, our data suggest that the observed interchromosomal interactions reflect key features of nuclear organization in spermatogenesis and that A compartments tend to self-associate between different chromosomes regardless of the stages of spermatogenesis (**Figure 3.3b**, **3.3c**).

Attenuated topologically associating domains in meiosis. In addition to genomic compartments, chromatin is spatially organized into regions of preferential interactions termed topologically associating domains (TADs)[169,170]. TADs have been implicated in the regulation of gene expression[170,182-184], and meiosis and subsequent stages are notable for their active transcriptomes, which are among the most complex and diverse known[6]. Thus, we identified TAD boundaries in late spermatogenesis with the software package HiCExplorer[185,186] (**Materials & Methods**; **Figure 3.4a**; **Supplementary Dataset 4**). In pachytene spermatocytes and round spermatids, we observed weak, large TADs, ~1.1 Mb in length on average (**Figure 3.4b**; **Supplementary Figure 3.6**; **Supplementary Dataset 4**). While many TAD boundaries were unique to each germ cell dataset (or shared between two of the three datasets), a subset of boundaries persisted from pachytene spermatocytes through to sperm (**Figure 3.4b**, **3.4c**): 622 TAD boundaries were common to pachytene spermatocytes (~27% of 2,300), round spermatids (~28% of 2,233), and sperm (~14% of 4,541). As late spermatogenesis progressed, the large TADs of pachytene spermatocytes and round spermatids underwent consolidation, forming an abundance of stronger, smaller TADs in sperm, ~0.56 Mb in length on average (**Figure 3.4b; Supplementary Figure 3.6**; **Supplementary Dataset 4**).

Consistent with these observations, the levels of distance-normalized chromatin interactions around sites of sperm TAD boundaries (±2 Mb) are higher in pachytene spermatocytes and round spermatids relative to those in sperm and ESCs (**Figure 3.4d**: the baseline is above 1.0 in the PS and RS datasets). We further confirmed these data with 2D analyses of interaction frequencies in relative positions from start and end sites of sperm TAD boundaries (**Figure 3.4e**). We detected weak structural features in pachytene spermatocytes and round spermatids ± 0.5 Mb from the sites of sperm boundaries (**Figure 3.4f**). This finding is in contrast with the sperm and ESC datasets, in which chromatin interactions were largely restricted to within the sperm TAD boundaries (**Figure 3.4f**). Interestingly, although a subset of weak TAD boundaries in pachytene spermatocytes were maintained as late spermatogenesis progressed, they did not strengthen in sperm or ESCs (**Supplementary Figure 3.7**). Taken together, these results suggest that many weak TAD boundaries apparent in meiotic spermatocytes are maintained in mature sperm, and additional alternative strong boundaries are gained.

Notably, in pachytene spermatocytes and round spermatids, the presence of common A and B compartments, along with large and weak TADs, evokes a chromosomal resemblance to paternal alleles in preimplantation development, which are in the midst of reprogramming of 3D chromatin organization[13,16,177]. Such features are distinct from those in somatic mitotic chromosomes and MII oocytes, which lack A and B compartments and TADs[13,16,171,174,177,178] (**Supplementary Figure 3.2b**), thereby illuminating a chromatin configuration unique to meiotic chromosomes. This 3D chromatin status persists from meiotic prophase I into round spermatids, which evince interphase-like nuclei after two rounds of reductional meiotic divisions. Through two successive rounds of meiotic divisions, chromosomes are condensed in two accompanying rounds of metaphase, during which 3D chromatin organization is presumed to have disappeared, as is the case with mitotic chromosomes and MII oocytes[13,16,171,174,177,178] (**Supplementary Figure 3.2b**). Thus, these results may suggest that the epigenetic state of 3D chromatin organization is maintained through meiotic divisions.

Pairwise point interactions and active transcription during meiosis. Localized pairwise point interactions have been identified in high-resolution Hi-C interphase maps and have been associated with the activation of transcription and the interplay of gene regulatory elements[187]. These point interactions are thought to arise from the clustering of regulatory elements and genes through chromatin looping mechanisms[187]. Chromosomes in meiotic prophase I are distinct from those in mitotic M phase due to ongoing robust transcription. Thus, we examined the data for signs of such point interactions, both visually and computationally. We found that point interactions are clearly apparent in the data (**Figure 3.5a**) and, using the cLoops peak-calling package[188] with stringent statistical filtering (**Materials & Methods**), we identified 1,985 such point interactions genome-wide in pachytene spermatocytes (**Supplementary Dataset 5**).

Next, we sought to answer the following question: Are these point interactions associated with specific genomic functions? We analyzed RNA-seq signal along with ChIP-seq signals for the deposition of active histone modifications H3K27ac and H3K4me3, as well as silent histone modification H3K27me3, at the anchor sites of point interactions (**Supplementary Dataset 5**).

We found that, on average, anchors are enriched in H3K27ac and H3K4me3 ChIP-seq signals, as well as RNA-seq signal (**Figure 3.5b**). Relative read enrichments for the histone and RNA-seq datasets were higher at anchors versus other regions of the genome (**Supplementary Figure 3.8a**, **3.8b**), and correlation calculations demonstrated a weak positive correlation between the anchors and the ChIP-seq and RNA-seq datasets (**Supplementary Figure 3.8c**). It is interesting to note, too, that the loci of point interactions appear to persist into round spermatids (**Supplementary Figure 3.8d**); this is consistent with the overall similarity of transcriptomes in pachytene spermatocytes and round spermatids after the mitosis-to-meiosis transition of spermatogenesis[3]. Our data suggest that point interactions comprise a higher-order form of chromatin organization associated with active histone modifications and gene activation in late spermatogenesis.

Epigenetic mechanisms associated with 3D chromatin organization in the germline. This led us to an intriguing question: How does the higher-order organization of pachytene spermatocytes and round spermatids relate to the formation of TADs in sperm? To seek an answer, we analyzed the deposition of H3K27ac, H3K4me3, and H3K27me3 at sites of sperm TAD boundaries (**Supplementary Dataset 4**) across the four datasets. Surprisingly, we observed the strong enrichment of H3K27ac, H3K4me3, and H3K27me3 at the sites of sperm TAD boundaries in pachytene spermatocytes and round spermatids (**Figure 3.6a**), indicating that sperm TAD boundaries are delineated with epigenetic marks as early as the pachytene spermatocyte stage. The enrichment of histone modifications at sperm TAD boundaries was also present in ESCs (**Figure 3.6b**). These results raise the possibility that epigenetic mechanisms—able to persist through divisions, including meiotic divisions—determine 3D chromatin organization in the germline. In the germline, bivalent genomic domains that retain both H3K4me3 and H3K27me3 on gene regulatory elements are postulated to be responsible for epigenetic inheritance across generations[4,90]. Therefore, such mechanisms could serve as persistent memories through meiotic divisions. In support of this notion, from pachytene spermatocytes through to sperm, H3K27me3 is enriched in A compartments, which are also enriched with H3K4me3 (**Figure 3.2c**; **Supplementary Figure 3.4**).

3D chromatin organization of the XY body during meiosis and postmeiotic sex chromatin in round spermatids. Next, we shifted our attention from autosome chromatin organization to chromatin organization of the X chromosome. In pachytene spermatocytes, the sex chromosomes undergo a phenomenon known as meiotic sex chromosome inactivation (MSCI) and form a transcriptionally silent compartment termed the “XY body” (also known as the “sex body”)[65]. MSCI begins when DNA damage signaling recognizes the unsynapsed status of the hemizygous X and Y chromosomes, resulting in their transcriptional repression[64]. Consistent with the distinct regulation of the sex chromosomes in the XY body, interaction maps of pachytene spermatocytes revealed that X evinces chromatin organization that is highly—but not entirely—homogenous (**Figure 3.7a–c**; **Supplementary Figure 3.9**), without chromatin compartments (**Figure 3.7a–c**; **Supplementary Figure 3.9b**). In this respect, the pachytene spermatocyte X closely resembles the MII oocyte X (**Supplementary Figure 3.9a**, **3.9b**). Interestingly, the chromatin features of the inactive X chromosome in meiosis are distinct from those of the inactive X chromosome in female X chromosome inactivation. In female X chromosome inactivation, X is folded into two “mega-domains”[187,189-191] that are established via a stepwise mechanism[192]. However, the silent male X in meiosis does not have apparent mega-domains (**Figure 3.7a**, **3.7c**; **Supplementary Figure 3.9a**, **3.9b**). This could be explained by the mechanistic difference between male and female inactive X chromosomes: The male inactive X chromosome is established via DNA damage signaling, whereas the female inactive X is established through the action of non-coding *Xist* RNA[64,143].

The distinct regulation of the sex chromosomes persists into postmeiotic round spermatids, where either X or Y is organized into a silent compartment, termed “postmeiotic sex chromatin," in the center of the nucleus[69] (**Figure 3.1a**). We observed the beginnings of higher-order chromatin organization in round spermatids in the form of distal interactions greater than 10Mb (**Figure 3.7b**); however, as in pachytene spermatocytes, round spermatids lacked chromatin compartmentalization in postmeiotic sex chromatin (**Figure 3.7c**, **3.6d**). In support of these results, by measuring genomic compartment strength, we confirmed that intrachromosomal genomic compartments are absent from the X chromosome in pachytene spermatocytes and round spermatids (**Figure 3.7e**). In round spermatids, a small number of sex-linked genes escape postmeiotic silencing to spur differentiation into sperm[69,72]. However, these escape genes did not demonstrate apparent features of 3D chromatin organization in round spermatids (**Supplementary Figure 3.9c**). By the time germ cells progressed to sperm, higher-order features of chromatin organization, such as compartments, were observable (**Figure 3.7**; **Supplementary Figure 3.9c**). The overall features of the sperm X resemble those of the active X in ESCs, especially with respect to multidomain organization[167] (**Figure 3.7a**; **Supplementary Figure 3.9c**), whereas compartments are distinct between the sperm X and the active X in male ESCs, which is of maternal origin (**Figure 3.7c**, **3.7d**). Together, our data implicate 3D chromatin organization in the distinct regulation of the sex chromosomes in germ cell development.

Discussion

In this study, we revealed a form of 3D chromatin organization predominated by local, weakly preferential chromatin interactions in meiotic prophase I; 3D chromatin organization expands to distal, although still weakly preferential, interactions in postmeiotic spermatids. These features present intriguing clues to understand the structure of meiotic chromosomes in prophase. Through microscopy of mammalian cells, chromatin loop array structures in meiotic prophase I were reported to be similar to those of their mitotic counterparts[193], which an earlier Hi-C study modeled as compressed arrays of consecutive loops[171]. However, to date, 3D structural information is lacking in mammalian meiotic prophase I. In yeast, chromosome conformation capture (3C), the pioneering method that underlies Hi-C, provided keen structural insights into meiotic chromosomes[194], and recent yeast Hi-C studies demonstrated that meiotic chromosomes are comprised of dense, dynamic arrays of chromatin loops with variable sizes[195,196]. However, in comparison with those of other eukaryotes, yeast chromosomes do not display some features of higher-order chromatin organization, such as A/B compartments[197-199], thereby precluding direct comparisons between yeast and mammalian meiotic chromosomes. Here, we show that mammalian meiotic chromosomes evince atypical features of higher-order chromatin organization: In comparison with somatic interphase chromosomes[169,173,175,178], the chromosomes of pachytene spermatocytes feature relatively attenuated structural features. One interpretation may account for this: Because our Hi-C data for pachytene spermatocytes represent the average structural features of ~25 million nuclei, each nucleus with two complements of the diploid genome, loop positions may be random in the cell population, and loop sizes may be variable.

Nonetheless, in comparison with mitotic chromosomes, pachytene spermatocyte chromosomes displayed a steeper decrease in intrachromosomal contact probability (**Figure 3.1d**), in addition to genomic compartmentalization (**Figure 3.2**) and the presence of TADs (**Figure 3.4**). It is intriguing to consider structural influences acting on the chromosomes of pachytene spermatocytes. Mechanistically, the structural features of meiotic chromosomes may be shaped by the meiosis-specific effects of cohesins and CTCF, which define 3D structural organization in interphase nuclei[200-202]. During meiosis, chromosome axes are ubiquitously loaded with meiosis-specific cohesins[203], and CTCF has an isoform unique to meiosis and subsequent stages, BORIS[204]. Thus, these factors may function in mechanisms that randomize loop positions.

After our analyses of meiotic chromosomes, the observations of patterns found in mitotic and interphase chromosomes raise interesting questions. For example, what physical genome structures are consistent with both the randomized loop arrays proposed for mitotic chromosomes and the consistent structural features typically found in interphase chromosomes? How is genomic organization functional in spite of its attenuated form? And how do condensed chromosomes form interchromosomal interactions between active chromatin loci (**Figure 3.3**)?

Although the features of chromatin loop arrays—random and/or structured—may be shared between autosomes and sex chromosomes during meiosis, we determined additional and unique structural features related to the inactive sex chromosomes in the male germline. Phase separation, a process by which membraneless organelles form and behave as liquid droplets[205,206], has been proposed as a mechanism for the formation of heterochromatin[207,208]. Furthermore, a phase separation mechanism was postulated for the stepwise establishment of the inactive X in females[192]. Given the highly homogeneous and isolated 3D chromatin organization of the inactive X in late spermatogenesis, the XY body and postmeiotic sex chromatin may represent droplet-like structures that are self-associating and spatially segregated via phase separation mechanisms. Furthermore, phase separation mechanisms also underlie sites of active transcription[209]. Therefore, it is tempting to speculate that phase separation mechanisms may underlie interchromosomal associations of A compartments.

In 1984, Robin Holliday proposed, in an article entitled “The biological significance of meiosis,” that a potential function of meiosis is the reprogramming of gametes to prepare for the next generation[15]. In accordance with this hypothesis, we propose that attenuated chromatin compartmentalization in meiosis is itself a form of reprogramming for 3D chromatin organization that facilitates spermatogenic gene expression. Moreover, attenuated chromatin compartmentalization corroborates the reorganization of various chromatin features in the mitosis-to-meiosis transition of the male germline[3,82,90]. In summary, our results reveal that the attenuated compartmentalization of germline chromatin is associated with unique and diverse transcriptomes, and that the maturation of germline chromatin to highly compartmentalized 3D chromatin organization in sperm prepares the next generation of life.

Statistical Analyses

No statistical methods were used to predetermine sample sizes. No data were excluded from analyses. The experiments were not randomized and, except where noted, investigators were not blinded to allocation during experiments and outcome assessment.

Materials & Methods

Animals and germ cell isolation. Wild-type C57Bl/6J mice were used for Hi-C analyses, and all experimental work was approved by the Institutional Animal Care and Use Committee, protocol no. IACUC2015-0032.

Pachytene spermatocytes and round spermatids were isolated from adult testes through sedimentation velocity at unit gravity as described[210]. At least 12 independent mice, at 90 to 120 days of age, were used for each isolation of germ cells. Purity was confirmed via fluorescence widefield microscopy. All images were acquired with an ECLIPSE Ti-E microscope (Nikon) and Zyla 5.5 sCMOS camera (Andor Technology), with 60× CFI Apochromat TIRF oil immersion lenses (Nikon), numerical aperture 1.40. Germ cells were identified by staining with 0.2 µg/ml Hoechst 33342. In keeping with previous studies from the Namekawa lab[3,82,90], mean purity of ≥91% for pachytene spermatocytes and ≥94% for round spermatids was confirmed for each experiment (**Supplementary Figure 3.1**; **Supplementary Dataset 1**). To quantify the purity of isolated germ cells, images of cell fractions from sedimentation velocity at unit gravity, their details having been blinded, were fed into a partially automated Fiji/ImageJ[163,164] processing pipeline. Using a Gaussian filter, the images were smoothed before the application of a pixel intensity maximum filter to identify local maxima, which were automatically scored as cells. Then, each processed image was checked manually to correct for false positives and false negatives. Unprocessed versions of the blinded images were manually checked for heterogeneous cell contamination. Percent contamination was calculated for given sets of images as follows:

$$\left(\frac{\text{number of heterogeneous cells}}{\text{corrected total number of cells}}\right) \times 100$$

The details of the processed and unprocessed versions of the images were unblinded, and sample purity for each fraction was calculated by subtracting the percent contamination for a given image from 100%. For both pachytene spermatocytes and round spermatids, two independent biological replicates were generated for Hi-C library preparation and sequencing (**Supplementary Dataset 2**).

Hi-C: Library generation and sequencing. To generate and sequence Hi-C libraries, Hi-C was performed as described[211] with the following details and additions: Samples were treated with HindIII restriction enzyme and, for DNA sequencing, NEBNext Oligos for Illumina, Index Primer Set 1, were used. To ensure high library complexity[176,187], each of two independent biological replicate libraries for pachytene spermatocytes, which have two complements of the diploid genome, were generated from 12.5 million cells (150-bp paired-end sequencing), and each of two biological replicate libraries for round spermatids, which have haploid genomes, were generated from 50 million cells (75-bp and 100-bp paired-end sequencing). All libraries were sequenced on either Illumina HiSeq2500 or HiSeq4000 sequencers according to the manufacturer's instructions.

Hi-C: Sourcing, alignment, and processing. Hi-C datasets not generated in this study were obtained from published work (**Supplementary Dataset 2**): sperm (50-bp paired-end reads; PMID 28178516, GEO GSE79230)[167], embryonic stem cells (ESCs; 75-bp paired-end reads; PMID 24185094, GEO GSE48592)[168], non-synchronized human foreskin fibroblasts (HFF1-non-synchronized; 50-bp paired-end reads; PMID 24200812, ArrayExpress E-MTAB-1948)[171], synchronized prometaphase mitosis human foreskin fibroblasts (HFF1-mitosis; 50-bp paired-end reads; PMID 24200812, ArrayExpress E-MTAB-1948)[171], and metaphase meiosis II oocytes (MII oocytes; 150-bp paired-end reads; PMID 28703188, GEO GSE82185)[13].

`.fastq` files for paired-end Hi-C libraries were mapped and processed using the cMapping package as described[175,176]. Matrix binning and balancing was performed with the cooler software package[212] (`version 0.7.6` or `0.7.10`). In brief, paired-end reads were iteratively mapped to the *Mus musculus* mm10 genome via Bowtie 2[213] (`version 2.3.3.1`), which was called with the following arguments:

```
--very-sensitive \
--no-head \
--no-sq \
--qc-filter \
--reorder
```

Uniquely aligned, paired reads were kept and assigned to restriction fragments. Mapped reads were filtered for fragment ends and uniqueness; PCR duplicates, defined as sequence matches with the exact same start and end, were excluded. Using the cooler software package, the valid pairs were binned at the following resolutions (kb):

1, 2, 5, 8, 10, 15, 20, 30, 40, 64, 100, 128, 250, 256, 512, 1024, 2048, 4096, and 8192

To correct for noisy and/or low-signal bins prior to matrix balancing, bins with coverage ≤20 genome-wide median deviations below the median bin coverage were excluded. Finally, matrices were balanced using Sinkhorn balancing such that the sum of every row and column is equal[175].

The alignment and processing pipeline resulted in 284.9 million unique, valid read pairs for pachytene spermatocytes (replicates pooled); 415.6 million unique, valid read pairs for round spermatids (replicates pooled); 371.0 million unique, valid read pairs for sperm (replicates pooled); 625.8 million unique, valid read pairs for embryonic stem cells (replicates pooled); 113.7 million unique, valid read pairs for non-synchronized human foreskin fibroblasts; 83.5 million unique, valid read pairs for synchronized prometaphase mitosis human foreskin fibroblasts; and 695.0 million unique, valid read pairs for metaphase meiosis II oocytes (replicates pooled; **Supplementary Dataset 2**). Processed, pooled Hi-C datasets were used for all experiments. To minimize the potential effects of variable sequencing depths when making comparisons between the datasets, processed, pooled Hi-C datasets for pachytene spermatocytes, round spermatids, sperm, embryonic stem cells, and metaphase meiosis II oocytes were randomly sampled to 280 million read pairs and then balanced via Sinkhorn balancing as described above; for non-synchronized human foreskin fibroblasts and synchronized prometaphase mitosis human foreskin fibroblasts, processed, pooled Hi-C datasets were randomly sampled to 83.5 million read pairs and then balanced via Sinkhorn balancing.

Hi-C: Analyses of intrachromosomal interaction matrices and differential interactions between samples. To generate and visualize interaction frequency heatmaps of whole chromosomes, Hi-C matrices at 100-, 128-, or 250-kb resolution were imported to the software package HiCExplorer[185,186] (`version 2.1.3 cooler_correction_patch`) for use with the application `hicPlotMatrix`. To aid visual comparisons between the datasets, matrices were natural log transformed. To analyze differential interaction frequencies between samples, the HiCExplorer application `hicCompareMatrices` was used to generate $\log_2$ ratios of interaction frequency matrices between two separate datasets.

Hi-C: Estimation of power-law coefficients for interaction frequency curves. To estimate the power-law decay coefficients for interaction frequency versus genomic distance, we used a maximum likelihood approach[214,215]. Specifically, we assumed that the probability of interaction between loci i and j is given by

$$P_{int}(i,j) = z|i-j|^{\alpha}$$

where z is a normalization factor to ensure a probability distribution. Next, we assumed a Hi-C experiment can be described as multinomial sampling from the above probability distribution. Therefore, the likelihood of observing Hi-C matrix X is

$$P_{int}(\,X|\alpha) = \left[\frac{!\sum X_{i,j}}{\prod(!\,X_{i,j})}\right]\Pi_{i,j}(z|i-j|^{\alpha})^{X_{i,j}}$$

We then used SciPy LM-BFGS quasi-Newton optimization[216] to find the α value that maximizes the likelihood. Since, in some cases, the data adhere to regimes with different power laws, we selected an appropriate range of genomic distances that were used to estimate α as follows: pachytene spermatocytes, 0.5–3 Mb; MII oocytes, 0.5–3 Mb; HFF1-mitosis, 0.5–7 Mb.

Hi-C: A/B compartment analyses. Hi-C matrices at 100- or 128-kb resolution were imported to HiCExplorer[185,186] (`version 2.1.3 cooler_correction_patch`) for use with the applications `hicTransform` and `hicPlotMatrix`. `hicTransform` was called to convert interaction frequency matrices to distance-normalized matrices (i.e., matrices taken from dividing observed interactions by expected interactions as described[173]), then to generate Pearson correlation coefficient matrices. `hicPlotMatrix` was used to visualize the Pearson correlation coefficient matrices.

To call genomic compartments, the HiCExplorer application `hicPCA` was employed to perform principal component analysis (PCA) on Pearson correlation coefficient matrices at 100- or 128-kb resolution (**Supplementary Dataset 3**). The largest eigenvector (EV1) represented the genomic compartment profile, which is consistent with previous reports[173,217,218]. For confirmation, consecutive eigenvectors were evaluated; eigenvectors beyond EV1 represented profiles distinct from genomic compartments (data not shown). Per convention, genomic compartments were assigned one of two designations, “A” (active/euchromatic compartments) and “B” (inactive/heterochromatic compartments), based on associated biological features, including gene density, mRNA transcription, and markers of chromatin state such as histone post-translational modifications. In comparison to B compartments, A compartments were denoted by higher gene densities (data not shown), increased enrichment for mRNA transcription, and increased enrichment of H3K27ac and H3K4me3, post-translational modifications conventionally associated with euchromatin and active transcription.

Hi-C: Evaluation of genomic compartment strengths. To evaluate the level of genomic compartmentalization between datasets, a new approach that calculates the “genomic compartment strength” was developed due to the limitations of PCA for this task. This approach quantifies the genomic compartment signal by examining the level of interaction in regions belonging to the same compartment versus regions belonging to different compartments. The definition of compartments is given by an eigenvector as explained in the preceding section; the choice of this vector is independent from the rest of the analysis. Then, we selected the highest 25% and lowest 25% of values, which indicate, respectively, strong A and strong B loci. Next, a Hi-C interaction matrix was distance-normalized by taking the

$$\log_2\left(\frac{\text{observed interactions}}{\text{expected interactions}}\right)$$

The resulting normalized matrix was referred to as a “LOE” matrix. Then, genomic compartment strength was defined as

$$\text{mean}(\text{AA LOE interactions}) + \text{mean}(\text{BB LOE interactions}) - 2[\text{mean}(\text{AB LOE interactions})]$$

Thus, if AA and BB interactions were stronger than AB interactions, a positive value was expected; if AA and BB interactions were equivalent to AB interactions, then a value close to zero was expected.

Hi-C: Genomic compartment strength analyses in a controlled setting. To evaluate the accuracy of quantified compartment strengths from genomic compartment strength analyses, different portions of the sperm Hi-C matrix S (which has the highest genomic compartment strength) were mixed with a matrix M that does not have genomic compartments. Matrix M was constructed by taking the pachytene spermatocyte interaction frequency map and converting it to an expected interaction map (PS) such that the interaction probability at distance x is the average interaction probability of all loci within that distance. It was verified that M has a genomic compartment strength of approximately zero. To obtain a mixed matrix with fraction f reads from the sperm matrix S, we sampled

$$f \times \mathrm{sum}(PS)$$

reads multinomially by the probabilities of matrix S, and combined these with

$$(1 - f) \times \mathrm{sum}(PS)$$

reads sampled multinomially by the probabilities of matrix M. We created mixed matrices at controlled levels, where

$$f \text{ is } [0, 0.1, 0.2, 0.3, 0.4, 0.5, 0.6, 0.7, 0.8, 0.9, 1.0]$$

and genomic compartment strength was calculated for each such matrix, both for cis and trans interactions. To avoid eigenvector distortion resulting from weak compartment signals, all mixed samples used the eigenvector extracted from S. To account for randomness introduced by sampling, we repeated this analysis 10 times and calculated the mean and standard deviation of the genomic compartment strength at each value of f (**Supplementary Dataset 3**). We observed that genomic compartment strength is sensitive to detect differences between the matrices and scales nearly linearly at ranges 0.2–1.0 (**Supplementary Figure 3.3**).

Next, we sought to address the following possibility: The relatively weak genomic compartment strengths observed in pachytene spermatocytes and round spermatids could be entirely due to contamination by a small fraction of cells that have strong compartmentalization. By comparing the observed genomic compartment strengths of pachytene spermatocytes and round spermatids to the calibration curve, we found that the pachytene spermatocyte samples would need to be contaminated by ~22% cells with strong compartmentalization to reach the observed genomic compartment strength; round spermatid samples would need to be contaminated by ~55% cells with strong compartmentalization (**Supplementary Figure 3.3**). Since the mean contamination of pachytene spermatocytes is ≤9% and the mean contamination of round spermatids is ≤6% (**Supplementary Figure 3.1**), these results suggested that the observed compartmentalization is likely not due to contamination. The analysis was performed with interaction matrices at 1024-kb resolution. Similar results were obtained with different matrix resolutions.

Hi-C: Evaluation of interchromosomal interactions. Given a Hi-C matrix at 1,024-kb resolution, an interchromosomal submatrix was taken for each pair of different chromosomes and rescaled into a matrix of size 500×500 bins. Each chromosome pair submatrix was taken in both orientations. Next, an average interchromosomal matrix was calculated by taking the average of all submatrices. Finally, the matrix was normalized by dividing each entry by the matrix mean and then taking the natural logarithm. Similar results were obtained with different matrix resolutions.

For analyses of interchromosomal interaction frequencies between two separate chromosomes, and for analyses of combined, genome-wide intrachromosomal and interchromosomal interactions, Hi-C matrices at 250-kb resolution were imported to HiCExplorer[185,186] (`version 2.1.3 cooler_correction_patch`) for use with the application `hicPlotMatrix`. Resulting data were natural log transformed to aid visual comparisons between the datasets.

Hi-C: Identification and visualization of topologically associating domains. Hi-C matrices were imported to HiCExplorer[185,186] (`version 2.1.3 cooler_correction_patch`) for use with the applications `hicFindTADs` and `hicPlotTADs`. `hicFindTADs` identifies TAD boundaries through an approach that calculates "TAD separation scores"[185,219]. Briefly, for each dataset, interaction frequency matrices at 20-kb resolution were transformed into z-score matrices based on the distribution of contacts at given genomic distances. Then, for a given bin of a z-score submatrix, the contacts between an upstream and downstream region of width w were calculated, thereby generating a TAD separation score; to reduce noise, multiple values were used for w and averaged per bin. Genomic bins with low TAD separation scores relative to neighboring regions were defined as local minima and called as TAD boundaries; stronger boundaries possessed lower TAD separation scores. Statistical significance was estimated for each local minimum by comparing the distribution of z-scores for submatrices, and the Wilcoxon rank sum test was used to compare the values. The false-discovery rate (FDR) was used to correct *P* values; the FDR *Q* value threshold was set to 0.01. A thorough explanation for how `hicFindTADs` functions, including usage examples, is available in PMID 29335486 [185] as well as the online documentation for HiCExplorer:

- http://hicexplorer.readthedocs.io/en/latest/content/tools/hicFindTADs.html#hicfindtads

`hicFindTADs` was called on all processed, pooled Hi-C matrices with the following arguments (all other arguments were set to default parameters):

```
--minDepth 80000 \

--maxDepth 800000 \

--step 40000 \

--minBoundaryDistance 80000 \

--correctForMultipleTesting fdr \

--thresholdComparisons 0.01 \

--delta 0.01
```

The output of `hicFindTADs` includes lists of TAD separation scores (**Supplementary Dataset 4**), and these were imported to the application `hicPlotTADs` in order to plot regions along the diagonals (i.e., the linear DNA) of interaction frequency matrices in combination with TAD boundary start and stop positions, which were also output by `hicFindTADs`. In addition, lists of TAD separation scores and positions were used to calculate and graph various TAD metrics for the individual datasets (e.g., **Figure 3.4a**, **3.4c**; **Supplementary Figure 3.6**; **Supplementary Dataset 4**).

Hi-C: Evaluation of topologically associating domain boundary intersections. To compare the intersections of TAD boundaries between pachytene spermatocytes, round spermatids, and sperm, we culled 1-bp TAD boundary positions using `.bed` output from `hicFindTADs` (**Supplementary Dataset 4**). However, because `hicFindTADs` was run on interaction frequency matrices at 20-kb resolution (i.e., binned in 20-kb windows), these data cannot call boundary positions with the accuracy of 1 bp; to account for this, we took the 1-bp TAD boundary positions ± 30 kb (i.e., 60 kb centered on each boundary) for subsequent analyses. The TAD boundary positions ± 30 kb were saved in `.bed` files (**Supplementary Dataset 4**) and fed into the command line program Intervene[220]. Intervene was set to call the R package UpSetR[221], which visualizes intersections in a matrix layout, grouping datasets based on the presence and/or absence of intersections. An example command line call for the evaluation of TAD boundary intersections:

```
$ intervene upset -i $PS_bed_30kb $RS_bed_30kb $sperm_bed_30kb
```

Hi-C: Evaluation of interaction frequencies between topologically associating domain boundaries. For each intrachromosomal matrix, we normalized each 2D bin *b* by dividing its value by the average value of all bins in its diagonal and taking the natural logarithm of the result. Next, for each pair of TAD boundaries, we extracted from the normalized matrix a 51×51 submatrix at 20-kb resolution, centered on the intersection of the boundaries. Then, we calculated the average over all submatrices. For this analysis we used only data within diagonals 3–500 (i.e., genomic distances of 60 kb to 10 Mb) of the normalized matrix.

To compute 2D line plots depicting interaction tendencies 0 to ±2 Mb from TAD boundaries (**Figure 3.4d**; **Supplementary Figure 3.7a**), distance-normalized submatrices (observed interactions/expected interactions), derived from Hi-C interaction frequency matrices at 20-kb resolution, were called with the HiCExplorer[185,186] (`version 2.1.3 cooler_correction_patch`) application `hicAggregateContacts`. In brief, submatrices centered at the intersections of TAD boundary start and end regions were selected, and all interactions from 0 to ±2 Mb of the boundaries were considered. These interactions were split over 100 bins from the center of the submatrix in the horizontal and vertical directions. Then, the submatrices were pooled by computing their averages at all positions. The interaction frequencies of the averaged submatrices were normalized by dividing individual values by the total interaction frequencies in the submatrix. Then, the diagonal, from top left to bottom right, of the pooled, averaged submatrix was output as a 2D line plot. `hicAggregateContacts` was called with the following arguments:

```
--avgType mean \
--transform obs/exp \
--range 20000:2020000 \
--numberOfBins 100 \
--plotType 2d \
--diagnosticHeatmapFile $basefile_description_date.svg \
--howToCluster diagonal \
--kmeans 1
```

Hi-C: Identification of pairwise point interactions in pachytene spermatocyte chromosomes. Pairwise point interactions were called on pachytene spermatocyte data using the software package cLoops (`version 0.9`)[188] as follows:

```
$ cLoops \
-f $file_bedpe \
-o $output_hic \
-s \
-eps 10000,15000,20000,25000 \
-minPts 10,20,30,40,50 \
-hic
```

We identified 12,990 significant point interactions. However, manual assessment of the results indicated that a majority of these could either not be confirmed visually or were not found in both replicates. We therefore reduced the set into a high-confidence set of 1,985 point interactions (**Supplementary Dataset 5**), which better matched visual assessment and was more consistent between replicates. To reduce the set, we selected only significant point interactions with a $\text{binomial } P \text{ value} < 1 \times 10^{-10}$. We found that this filtered set of point interactions was also consistent with an independent peak-calling method based on signal-processing filters (data not shown).

RNA-seq and ChIP-seq: Sourcing, alignment, processing, and visualization. RNA-seq and ChIP-seq datasets were obtained from published work: For RNA-seq, pachytene spermatocytes and round spermatids (PMID 25703348, GEO GSE55060)[3], sperm and embryonic stem cells (PMID 22242016, DDBJ DRA000484)[222]; for ChIP-seq of H3K27ac, pachytene spermatocytes and round spermatids (PMID 29462142, GEO GSE107398)[223], sperm (PMID 28178516, GEO GSE79230)[167], and embryonic stem cells (PMID 22763441, GEO GSE29218)[224]; for ChIP-seq of H3K4me3, pachytene spermatocytes and round spermatids (PMID 25703348, GEO GSE89502)[3], sperm (PMID 28178516, GEO GSE79230)[167], and embryonic stem cells (PMID 22763441, GEO GSE29218)[224]; for ChIP-seq of H3K27me3, pachytene spermatocytes and round spermatids (PMID 25703348, GEO GSE89502)[3], sperm (PMID 28178516, GEO GSE79230)[167], and embryonic stem cells (PMID 25303531, GEO GSE57912)[225].

For RNA-seq analyses, `.fastq` files were aligned to the *Mus musculus* mm10 reference genome via Spliced Transcripts Alignment to a Reference (STAR; `version 2.4.2a`)[226], and only unique alignments were allowed with a maximum of two errors per alignment. For ChIP-seq analyses, `.fastq` files were aligned to the *Mus musculus* mm10 reference genome with Bowtie[227] (`version 1.1.1`), and only unique alignments were allowed with a maximum of one error per alignment. To estimate fragment sizes, and to find islands of enrichment, MACS2[228] (`version 2.1.0.20140616`) was used with an FDR Q value threshold of <0.2.

RNA-seq and ChIP-seq datasets were processed and visualized through one of two pipelines: (1) the BioWardrobe Experiment Management Platform[229], which indexes and normalizes `.bam` files, makes use of NCBI RefSeq annotation to categorize reads from `.bam` files, and then, for viewing, uploads the data to the UCSC genome browser;[230] and (2) the deepTools[231] (`version 3.1.0`) application `bamCoverage`, which was used to normalize indexed `.bam` files and bin resulting values in 50-bp windows; then, the output of `bamCoverage` was imported to HiCExplorer (`version 2.1.3 cooler_correction_patch`)[185,186] for visualization via the applications `hicPlotMatrix` and `hicPlotTADs`.

RNA-seq and ChIP-seq enrichment with respect to topologically associating domain boundaries, genomic compartments, and point interaction anchor centers. Using sorted `.bam` files and the software package ngsplot (`version 2.6.3`)[232], we calculated the enrichment of RNA-seq data and/or ChIP-seq data for histone post-translational modifications with respect to EV1 lists (**Supplementary Dataset 3**), TAD boundary lists (**Supplementary Dataset 4**), and lists of point interaction anchor centers (**Supplementary Dataset 5**). An example command line call for point interaction anchor centers:

```
$ ngs.plot.r \
-G mm10 \
-R bed \
-C $configuration_file \
-O $output_file \
-SE 0 \
-FL 400 \
-L 1000000
```

RNA-seq and ChIP-seq read enrichment at pairwise point interaction anchors. Using `.bedpe` files output by cLoops (`version 0.9`)[188], we generated a `.bed` file containing genomic location information for individual pairwise point interaction anchors on pachytene spermatocyte chromosomes (**Supplementary Dataset 5**). Using the program bedtools (`version 2.27.1`)[233] and its application `intersect`, we also generated a `.bed` file for all genomic regions excluding point interaction anchors. Then, we calculated read enrichment for ChIP-seq and RNA-seq data at anchor or anchor-excluded (i.e., "other") genomic regions using bedtools `intersect`, e.g.,

```
$ bedtools intersect -c \
-a $bed_regions \
-b $sort_bam_NGS_data > ${sort_bam_NGS_data%.bam}_reads_enrichment_regions.txt
```

Resulting regional read enrichment was normalized for sequencing depth using a counts per million (CPM) calculation, i.e., uniquely mapped reads were scaled by the total number of sequenced reads multiplied by 1,000,000:

$$\text{regional read enrichment} \times \left(\frac{1}{\text{total number of sequenced reads}} \times 1{,}000{,}000\right)$$

To test for statistical differences between reads at "anchor" versus "other" regions, we performed Wilcoxon rank sum tests with Bonferroni post corrections.

RNA-seq and ChIP-seq enrichment correlation with pairwise point interactions. The pairwise point interaction anchor `.bed` file (**Supplementary Dataset 5**) was converted to a `.bam` file through the bedtools[233] (`version 2.27.1`) application `bedtobam`. Then, we employed the software package deepTools[231] (`version 3.1.0`) application `multiBamSummary` to stratify the anchor, RNA-seq, and ChIP-seq `.bam` files in 40-kb bins and calculate the genome coverage for each bin. Resulting coverage matrices were processed with the deepTools application `plotCorrelation` in order to compute the Pearson and Spearman correlation coefficients, and to visualize the correlation calculation results as hierarchically clustered heatmaps.

Figure Preparation

Plots were generated with, alone or in combination, Excel (2013, Microsoft), the R software package ggplot2 (`version 3.1.0`)[234], and the various plotting programs employed by the other software packages used in this study. Illustrator (CS6, Adobe) was used for composing figures.

Code Availability

Source code for software used in this study, with documentation, examples, and additional information, is available at the following URLs:

- https://github.com/dekkerlab/cMapping [175,176]
- https://github.com/mirnylab/cooler [212]
- http://bowtie-bio.sourceforge.net/bowtie2 [213]
- https://github.com/deeptools/HiCExplorer [185,186]
- https://github.com/asntech/intervene [220]
- https://github.com/hms-dbmi/UpSetR [221]
- https://github.com/YaqiangCao/cLoops [188]
- https://github.com/alexdobin/STAR [226]
- http://bowtie-bio.sourceforge.net/ [227]
- https://github.com/taoliu/MACS [228]
- https://github.com/deeptools/deepTools [231]
- https://github.com/arq5x/bedtools2 [233]
- https://github.com/shenlab-sinai/ngsplot [232]
- https://github.com/tidyverse/ggplot2 [234]

Other code used in this study, including code for compartment strength analysis and code for average trans interaction analysis, is available at GitHub page of the lab of co-supervising author Noam Kaplan. A version of HiCExplorer[185,186] that includes the `version 2.1.3` `cooler_correction_patch` branch is forked at the Namekawa Lab's GitHub page and the lead author's GitHub page. A version of cLoops[188] that includes `version 0.9` is forked at the Namekawa Lab's GitHub page and the lead author's GitHub page. See the following URLs:

- https://github.com/KaplanLab/Spermatogenesis
- https://github.com/NamekawaLab/HiCExplorer [185,186]
- https://github.com/kalavattam/HiCExplorer [185,186]
- https://github.com/NamekawaLab/cLoops [188]
- https://github.com/kalavattam/cLoops [188]

Any further code is available upon request; otherwise, the additional code will be uploaded to the lead author's GitHub page as time allows. Information for the BioWardrobe Experiment Management Platform[229], which is commercial software, is available at the following URLs:

- https://biowardrobe.com [229]
- https://github.com/Barski-lab/biowardrobe [229]

Data Availability

All Hi-C sequencing data used in this study, including processed files for published datasets, have been deposited in the National Center for Biotechnology Information (NCBI) Gene Expression Omnibus (GEO) under the accession number GSE119805. The data that support the findings of this study are available from the corresponding authors upon reasonable request.

Acknowledgments

For advice and/or support during various stages of this project, we thank Job Dekker and Johan Gibcus, University of Massachusetts Medical School; James Taylor and Michael E. G. Sauria, Johns Hopkins University; Carolyn M. Price, University of Cincinnati College of Medicine; Joachim Wolff, University of Freiburg; Masashi Yukawa, Cincinnati Children's Hospital Medical Center; and Wenbo Deng, Cincinnati Children's Hospital Medical Center. For assistance with highperformance computing, we extend a special thank you to Roberto Perea, Cincinnati Children's Hospital Medical Center. We also thank members of the Namekawa Lab and Kaplan Lab for discussion and helpful comments regarding the manuscript. Funding sources: Albert J. Ryan Fellowship to Kris G. Alavattam; National Institutes of Health (NIH) R01 GM098605, R01 GM122776, and R21 ES027117, Research Grant (FY13-510) from the March of Dimes Foundation to Satoshi H. Namekawa; Azrieli Faculty Fellowship and Taub Fellowship to Noam Kaplan; NIH DP2 GM119134 to Artem Barski.

Author Contributions

The manuscript was written by Kris G. Alavattam, Noam Kaplan, and Satoshi H. Namekawa, with critical feedback from all other authors, and Kris G. Alavattam and Satoshi H. Namekawa designed the Hi-C experiments. Kris G. Alavattam and So Maezawa performed the Hi-C experiments. Kris G. Alavattam, Akihiko Sakashita, Haia Khoury, Artem Barski, Noam Kaplan, and Satoshi H. Namekawa designed and interpreted the computational analyses. Kris G. Alavattam, Akihiko Sakashita, Haia Khoury, and Noam Kaplan performed the computational analyses. Noam Kaplan and Satoshi H. Namekawa were joint supervisors of this work.

Competing Interests

Artem Barski is a cofounder of Datirium, LLC.

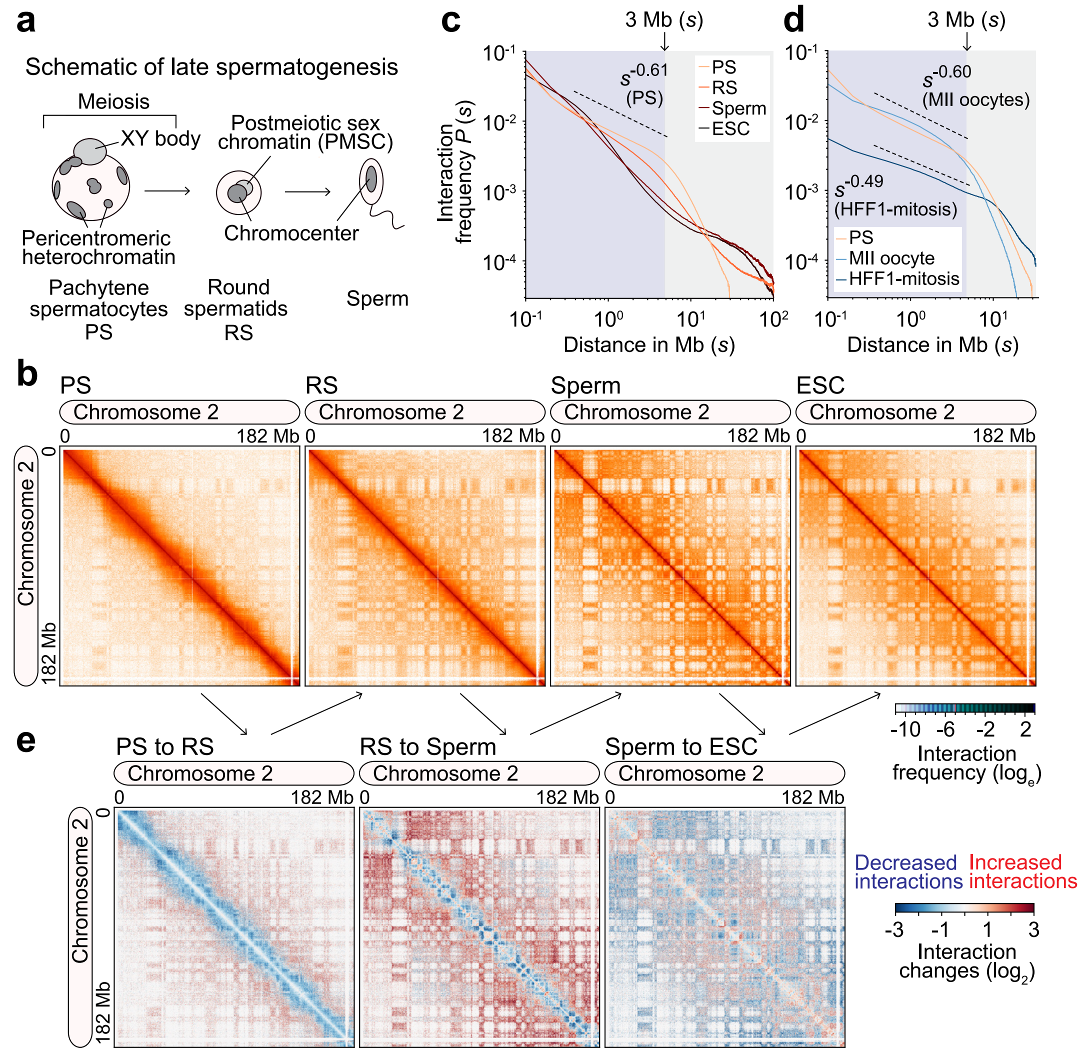

Figure 3.1: Dynamic 3D chromatin organization in late spermatogenesis.

Figure 3.1: Dynamic 3D chromatin organization in late spermatogenesis.

a, Schematic of stages of late spermatogenesis analyzed in this study. PS, pachytene spermatocyte; RS, round spermatid.

b, Heatmaps showing normalized Hi-C interaction frequencies (128-kb bins, chromosome 2) in PS, RS, sperm, and ESCs.

c, **d**, Hi-C intrachromosomal interaction frequency probabilities *P* stratified by genomic distance *s* for each cell type shown (100-kb bins, all chromosomes). MII oocyte, metaphase meiosis II oocyte; HFF1-mitosis, synchronized prometaphase mitosis human foreskin fibroblasts. The blue shadow indicates intrachromosomal interactions up to 3 Mb, and the gray shadow indicates intrachromosomal interactions at and beyond 3 Mb. Scaling coefficients are shown.

e, $\log_2$ ratio comparisons of the Hi-C interaction frequencies (128-kb bins, chromosome 2) for successive cell types.

Details and metrics for Hi-C datasets are presented in **Supplementary Dataset 2**.

See also **Supplementary Figures 3.1**, **3.2**.

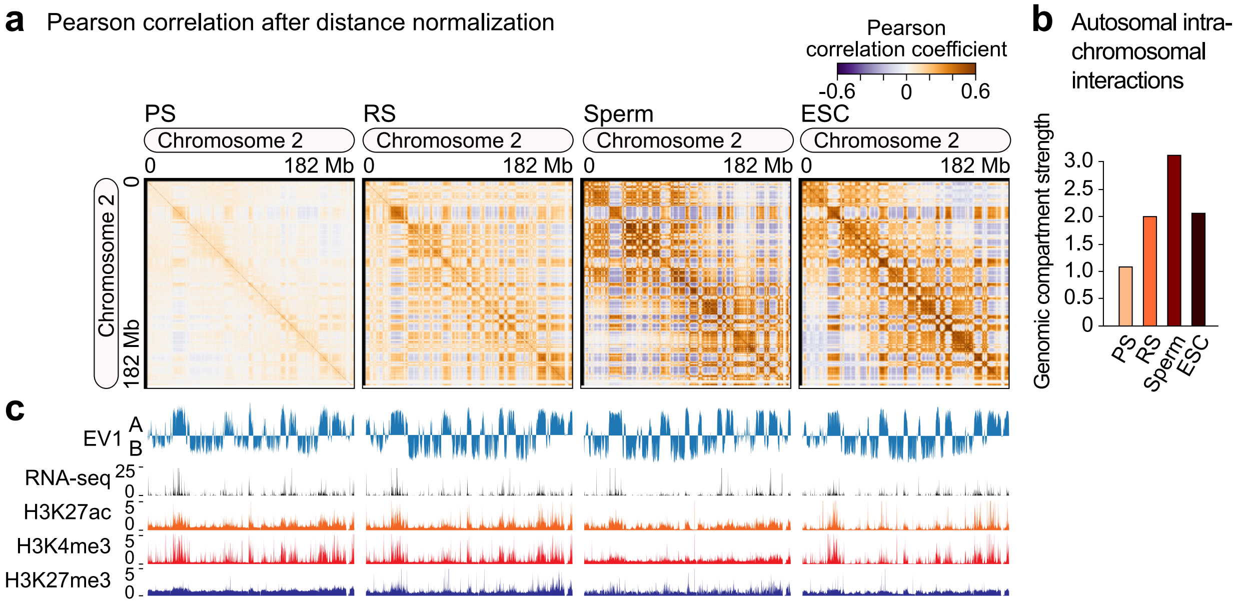

Figure 3.2: Attenuated compartmentalization of 3D chromatin organization in meiosis and its maturation in sperm development.

Figure 3.2: Attenuated compartmentalization of 3D chromatin organization in meiosis and its maturation in sperm development.

a, Pearson’s correlation for Hi-C interaction frequencies (128-kb bins, chromosome 2), which captures genomic compartmentalization patterns in pachytene spermatocytes (PS), round spermatids (RS), sperm, and ESCs.

b, Autosomal intrachromosomal interactions determined by the measurement of genomic compartment strength (**Materials & Methods**).

c, EV1 from principle component analysis, RNA-seq data, and ChIP-seq data for H3K27ac, H3K4me3, and H3K27me3 to classify genomic compartments as active (A) and repressed (B) in all cell types (128-kb bins, chromosome 2).

EV1s from principle component analyses are presented in **Supplementary Dataset 3**.

See also **Supplementary Figures 3.2–3.4**.

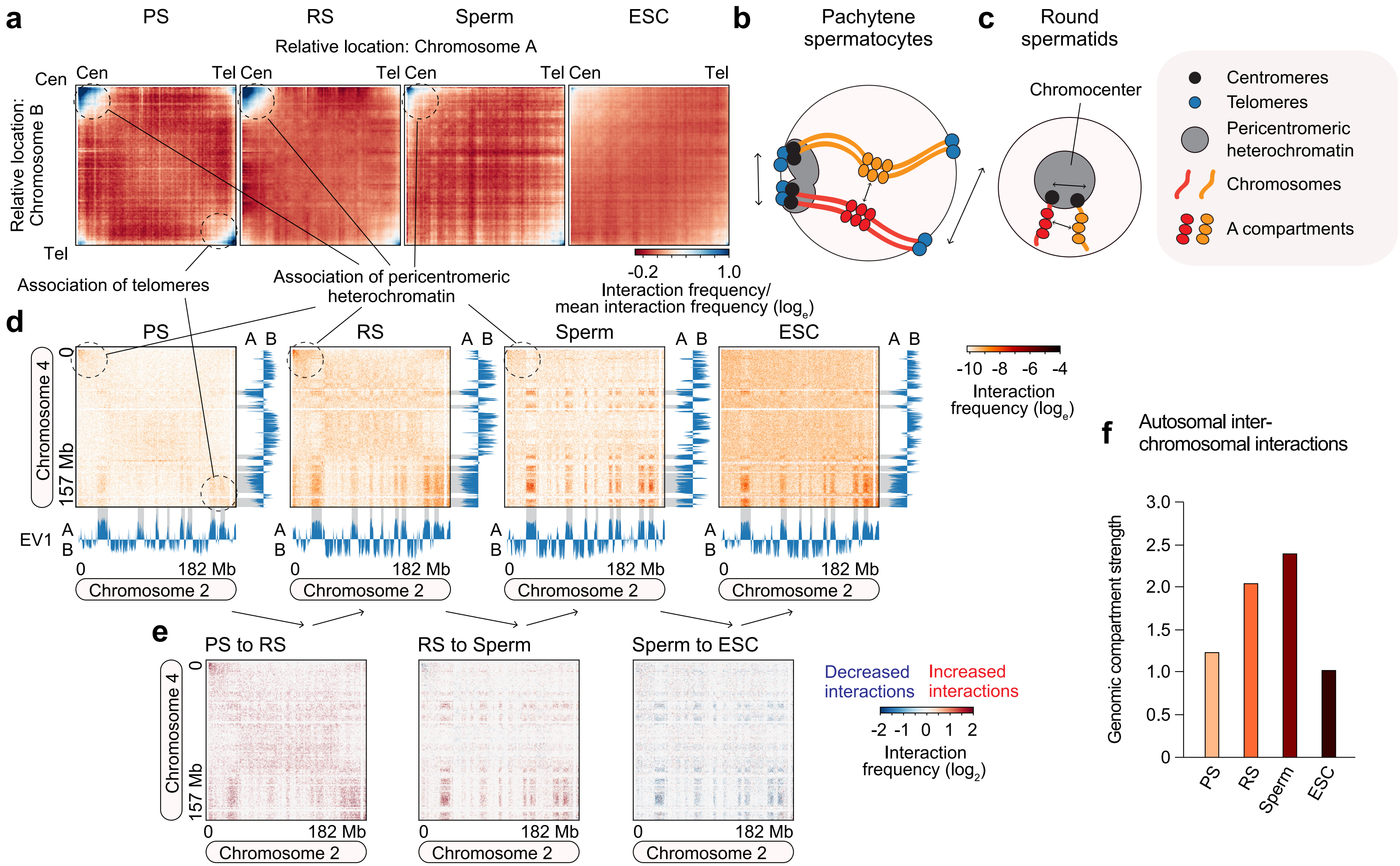

Figure 3.3: Interchromosomal interactions in late spermatogenesis.

Figure 3.3: Interchromosomal interactions in late spermatogenesis.

a, Average interchromosomal interactions between different chromosomes (denoted as chromosome A and chromosome B; Methods) in pachytene spermatocytes (PS), round spermatids (RS), sperm, and ESC. Cen, acrocentric ends (telomeres proximal to centromeres); tel, non-centromeric ends (telomeres distal to centromeres).

b, **c**, Models of interchromosomal interactions in pachytene spermatocytes (**b**) and round spermatids (**c**).

d, Heatmaps showing normalized Hi-C interchromosomal interactions (250-kb bins, chromosomes 2 and 4) for all cell types.

e, $\log_2$ ratio comparisons of the interchromosomal interaction frequencies (250-kb bins, chromosomes 2 and 4) for successive cell types.

f, Autosomal interchromosomal interactions determined by measurements of genomic compartment strength (**Materials & Methods**).

EV1s from principle component analyses are presented in **Supplementary Dataset 3**.

See also **Supplementary Figures 3.3**, **3.5**.

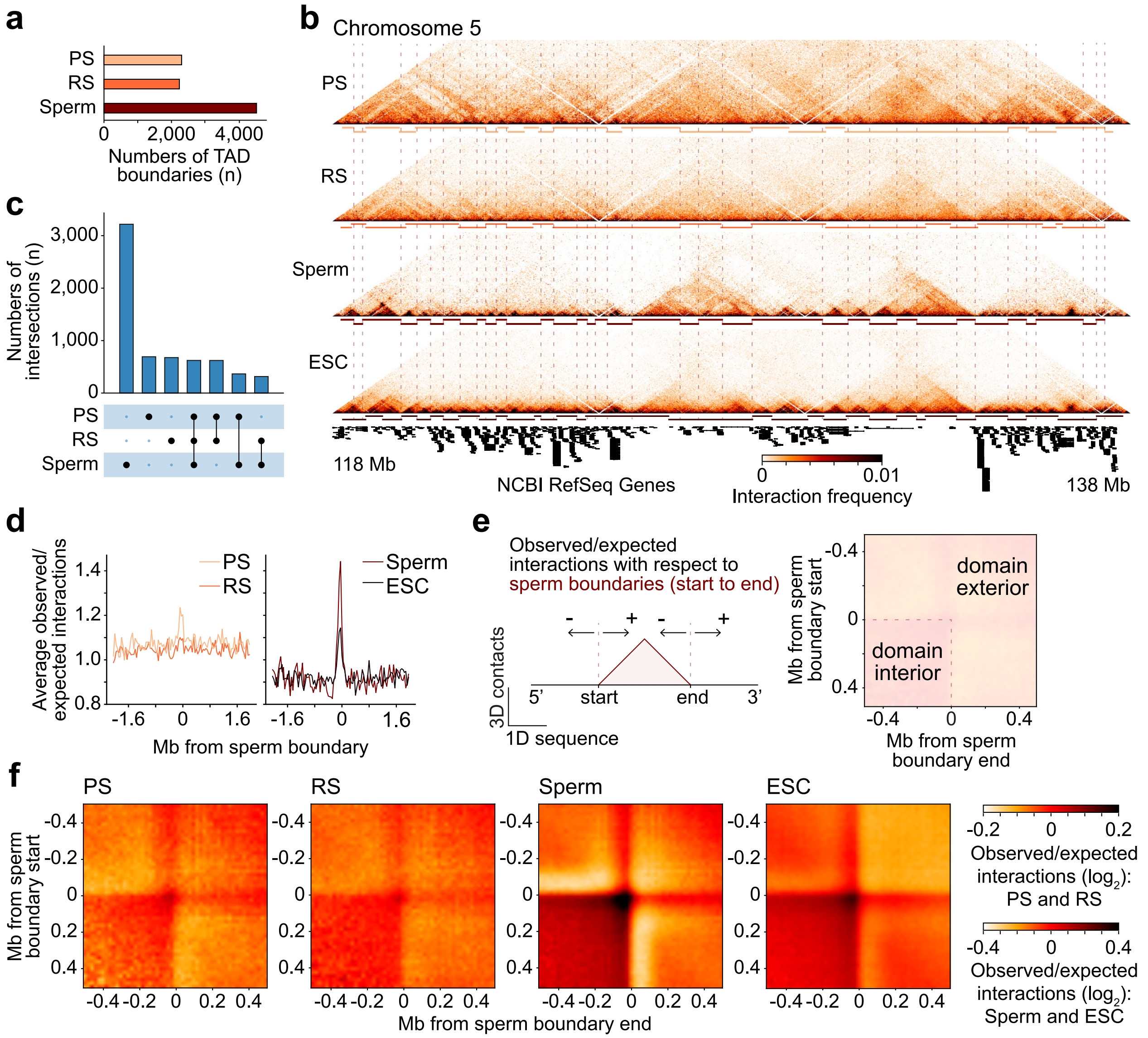

Figure 3.4: Attenuated topologically associating domains in meiosis and their maturation in sperm development.

Figure 3.4: Attenuated topologically associating domains in meiosis and their maturation in sperm development.

a, Numbers of TAD boundaries (*n*) in each dataset (60 kb centered on the boundary, 20-kb bins) for pachytene spermatocytes (PS), round spermatids (RS), and sperm.

b, Hi-C interaction heatmaps (20-kb bins, chromosome 5, 118–138 Mb) showing dynamics of local interactions and TADs in PS, RS, sperm, and ESCs. Horizontal solid bars, TADs as delimited by the software package HiCExplorer (**Materials & Methods**); dashed transparent bars, sperm TAD start and stop boundaries.

c, Numbers of intersections of TAD boundaries (*n*) between datasets. Vertical bars, overlap between TAD boundaries in the datasets below, which are further specified by solid black circles; black lines connecting the black circles indicate overlaps between multiple datasets. The intersections were plotted using the Intervene and UpSetR packages (**Materials & Methods**).

d, Average observed/expected interaction frequencies at sperm TAD boundaries ± 2 Mb for all cell types (20-kb bins, chromosome 2).

e, Schematic for interpretation of 2D matrix visualizations of observed/expected interaction frequencies at sperm TAD start and stop boundaries.

f, 2D matrix visualizations of $\log_2$ observed/expected interaction frequencies at sperm TAD start and stop boundaries ± 0.5 Mb for all cell types (20-kb bins, all chromosomes). In order to highlight their weak interaction patterns, PS and RS interactions are plotted on a different color scale.

Genomic location information for TAD boundaries and results from the evaluation of TAD boundary intersections are presented in **Supplementary Dataset 4**.

See also **Supplementary Figures 3.6**, **3.7**.

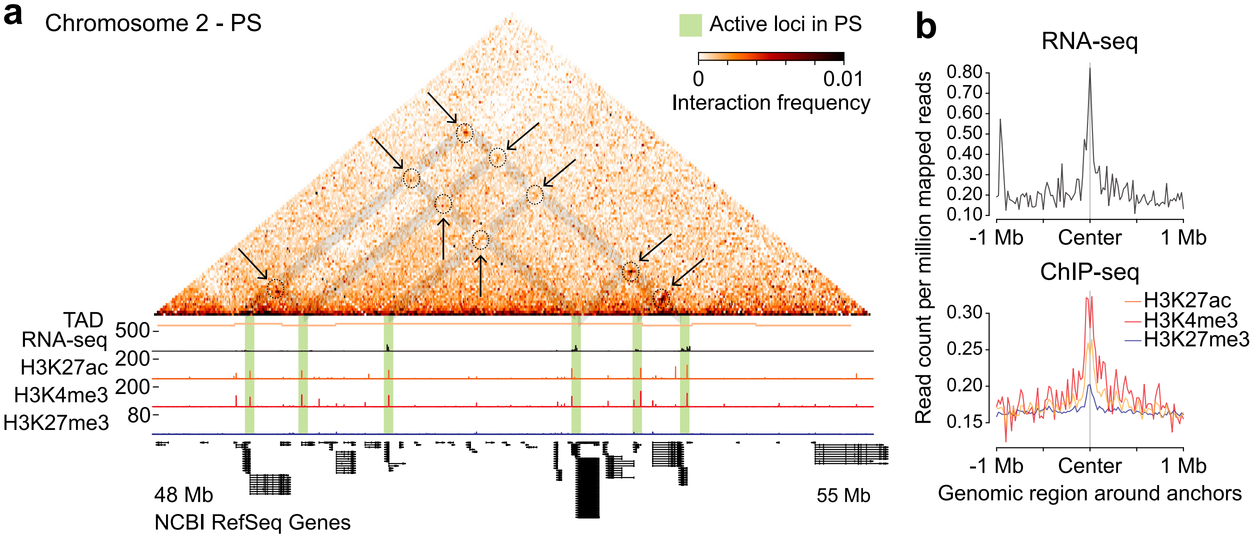

Figure 3.5: Pairwise point interactions in meiosis are delineated with epigenetic marks.

Figure 3.5: Pairwise point interactions in meiosis are delineated with epigenetic marks.

a, Hi-C interaction heatmaps (20-kb bins, chromosome 2, 48–55 Mb) of pachytene spermatocytes (PS) showing the dynamics of local interactions of active gene loci together with RNA-seq data and ChIP-seq data for H3K27ac, H3K4me3, and H3K27me3. y axis, RPKM. Solid bars, TADs called with the software package HiCExplorer (**Materials & Methods**). Green and gray highlights, arrows, and dashed circles indicate localized pairwise point interactions and related features of interest.

b, RNA-seq data (top) and ChIP-seq data for H3K27ac, H3K4me3, and H3K27me3 (bottom) to examine enrichment at the center of pachytene spermatocyte point interaction anchors ± 1 Mb (20-kb bins, all chromosomes). Point interactions were called with the software package cLoops (**Materials & Methods**).

Genomic location information for pairwise point interactions are presented in **Supplementary Dataset 5**.

See also **Supplementary Figure 3.8**.

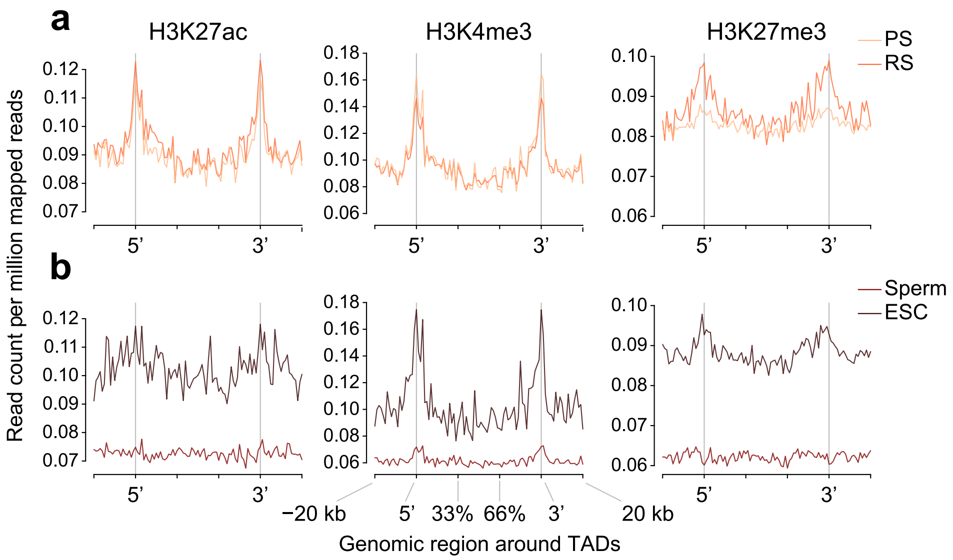

Figure 3.6: Sperm topologically associating domain boundaries are delineated with epigenetic marks as early as meiosis.

Figure 3.6: Sperm topologically associating domain boundaries are delineated with epigenetic marks as early as meiosis.

a, **b**, ChIP-seq data for H3K27ac, H3K4me3, and H3K27me3 to examine enrichment at sperm TAD start and stop boundaries along with domain interior and exterior (± 20 kb) portions (20-kb bins, all autosomes), in PS, RS, sperm, and ESCs.

Genomic location information for TAD boundaries are presented in **Supplementary Dataset 4**.

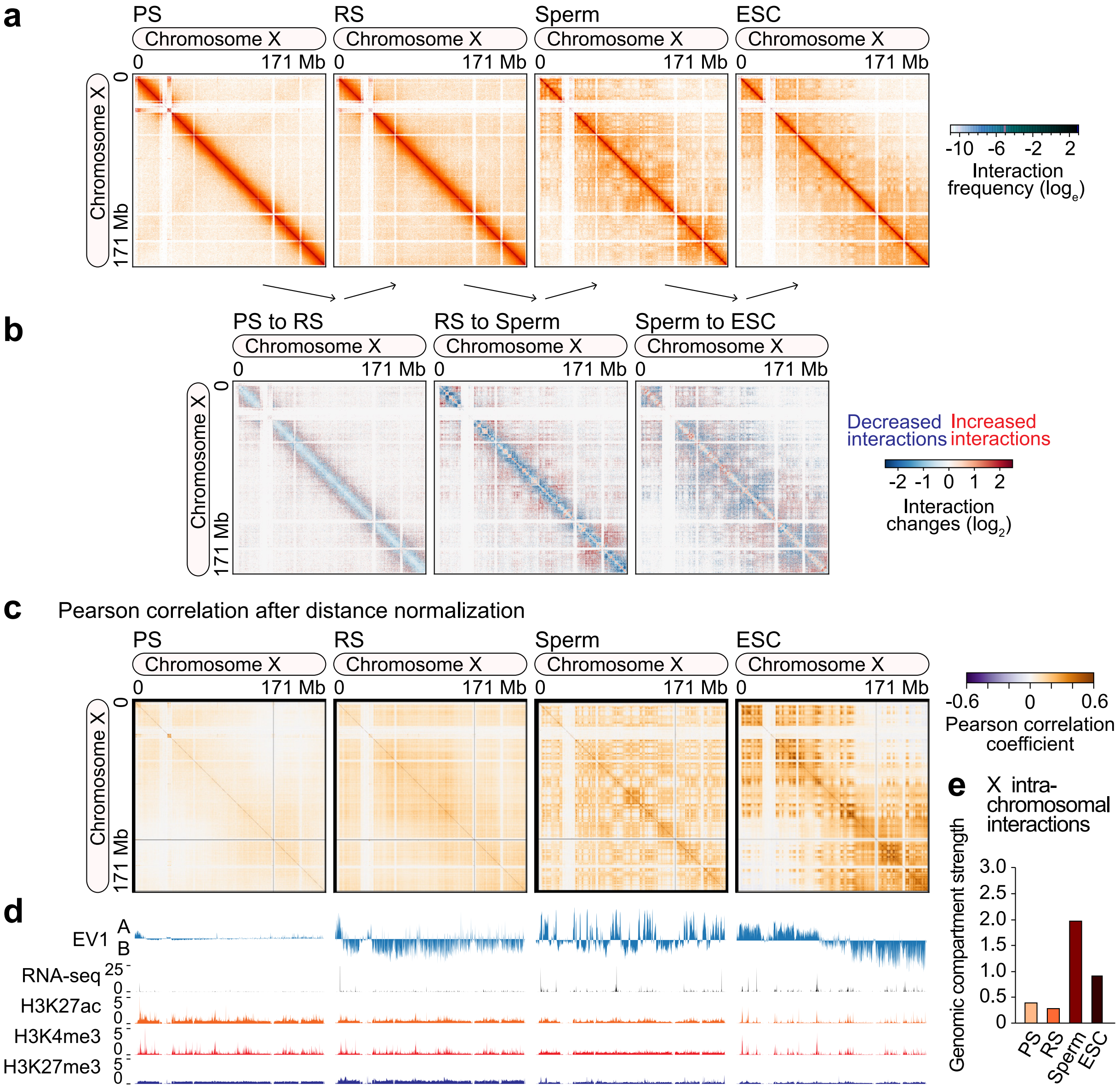

Figure 3.7: Chromosome X is lacking in higher-order chromatin organization during meiotic and postmeiotic silencing.

Figure 3.7: Chromosome X is lacking in higher-order chromatin organization during meiotic and postmeiotic silencing.

a, Heatmaps showing normalized Hi-C interaction frequencies (128-kb bins, chromosome X) in pachytene spermatocytes (PS), round spermatids (RS), sperm, and ESCs.

b, $\log_2$ ratio comparisons between the Hi-C interaction frequencies for successive cell types (128-kb bins, chromosome X).

c, Pearson's correlation for Hi-C interaction frequencies (128-kb bins, chromosome X), which captures genomic compartmentalization patterns in all cell types.

d, EV1 from principle component analysis, RNA-seq data, and ChIP-seq data for H3K27ac, H3K4me3, and H3K27me3 to classify genomic compartments as active (**a**) and repressed (**b**) in all cell types (128-kb bins, chromosome X).

e, X intrachromosomal interactions determined by the measurement of genomic compartment strength (**Materials & Methods**).

EV1s from principle component analyses are presented in **Supplementary Dataset 3**.

See also **Supplementary Figure 3.9**.

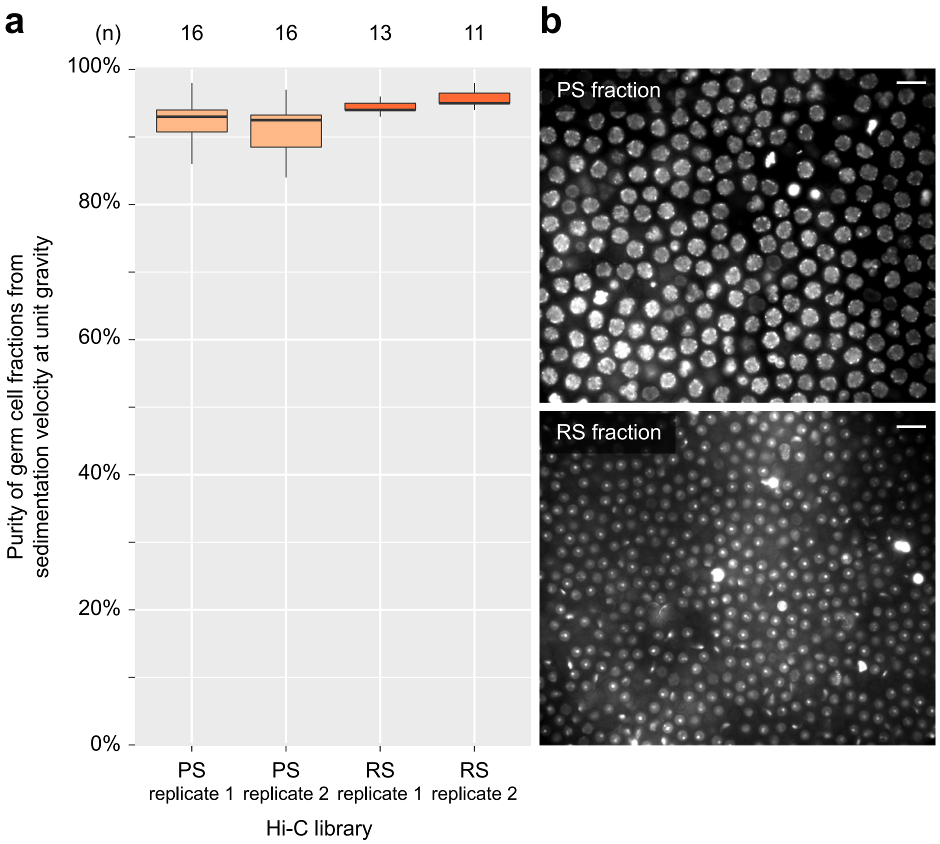

Supplementary Figure 3.1: Purity of germ cells isolated for Hi-C libraries, related to Figure 3.1.

Supplementary Figure 3.1: Purity of germ cells isolated for Hi-C libraries, related to Figure 3.1.

a, Box-and-whisker plots in the style of Tukey showing the distributions of percent purity of cell fractions obtained from sedimentation velocity at unit gravity (**Materials & Methods**) for the following: pachytene spermatocyte (PS) Hi-C library replicates 1 and 2, and round spermatid (RS) Hi-C library replicates 1 and 2. Numbers (n) along the top indicate the numbers of fractions used to prepare the corresponding library replicates below. Means and standard deviations for the purities of each cell fraction comprising the pachytene spermatocyte libraries: 92% ± 5.6% (replicate 1) and 91% ± 4.7% (replicate 2); for the round spermatid libraries: 94% ± 1.5% (replicate 1) and 95% ± 2.1% (replicate 2).

b, Fluorescence wide-field microscopy images of representative cell fractions for pachytene spermatocytes (top) and round spermatids (bottom). Scale bars, 20 μm.

See **Supplementary Dataset 1**.

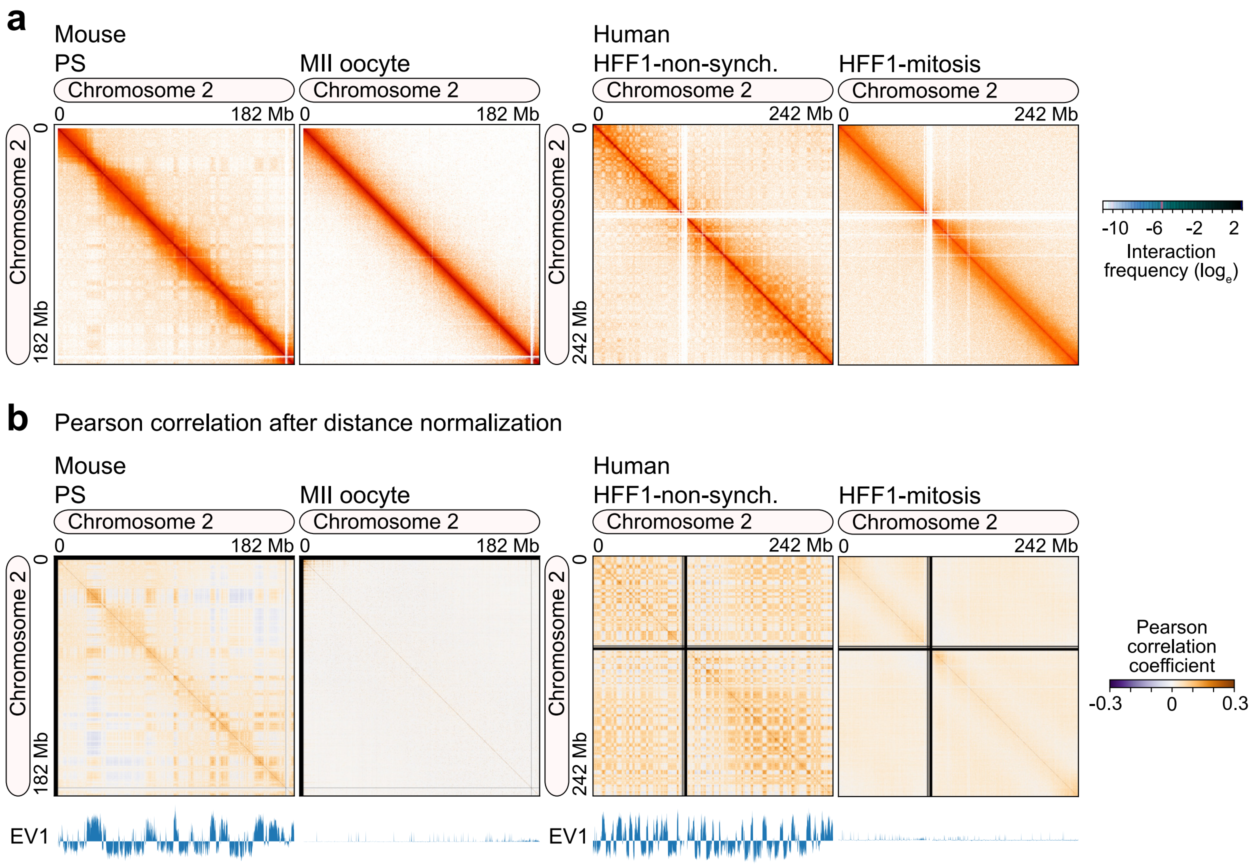

Supplementary Figure 3.2: Comparison of 3D chromatin organization in pachytene spermatocytes versus mitotic chromosomes, related to Figures 3.1, 3.2.

Supplementary Figure 3.2: Comparison of 3D chromatin organization in pachytene spermatocytes versus mitotic chromosomes, related to Figures 3.1, 3.2.

a, Heatmaps showing normalized Hi-C interaction frequencies (100-kb bins, chromosome 2) in pachytene spermatocytes (PS), metaphase meiosis II oocytes (MII oocyte), non-synchronized human foreskin fibroblasts (HFF1-non-synch.), and synchronized prometaphase mitosis human foreskin fibroblasts (HFF1-mitosis; HFF1-non-synch. is a control for HFF1-mitosis).

b, Pearson's correlation for Hi-C interaction frequencies (100-kb bins, chromosome 2) along with eigenvector 1 (EV1) from principle component analysis.

See **Supplementary Dataset 3**.

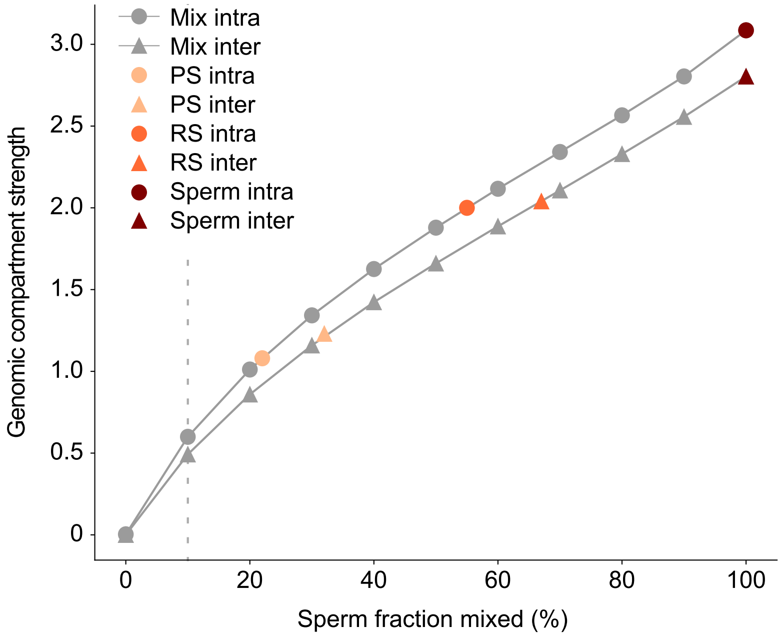

Supplementary Figure 3.3: Genomic compartment strength calibration, related to Figures 3.2, 3.3.

Supplementary Figure 3.3: Genomic compartment strength calibration, related to Figures 3.2, 3.3.

A random sample from the sperm Hi-C matrix, which has the highest genomic compartment strength, was mixed with a random sample from a Hi-C matrix which does not have genomic compartments (**Materials & Methods**). These were mixed at different ratios such that 10%, 20%, 30%, 40%, 50%, 60%, 70%, 80%, 90%, or 100% of the total reads were sampled from the sperm matrix, and this was repeated 10 times. Then, average genomic compartment strength was calculated at each mixing ratio to construct calibration curves for intrachromosomal compartments (grey circles) and interchromosomal compartments (grey triangles). Standard deviations are not shown as they were all smaller than 0.005. Finally, pachytene spermatocyte (PS) and round spermatid (RS) genomic compartment strength values were plotted on the calibration curves in order to estimate whether it is plausible that the observed genomic compartment strength is due only to contamination by approximately 10% (dashed line) cells that have genomic compartments.

See **Supplementary Dataset 3**.

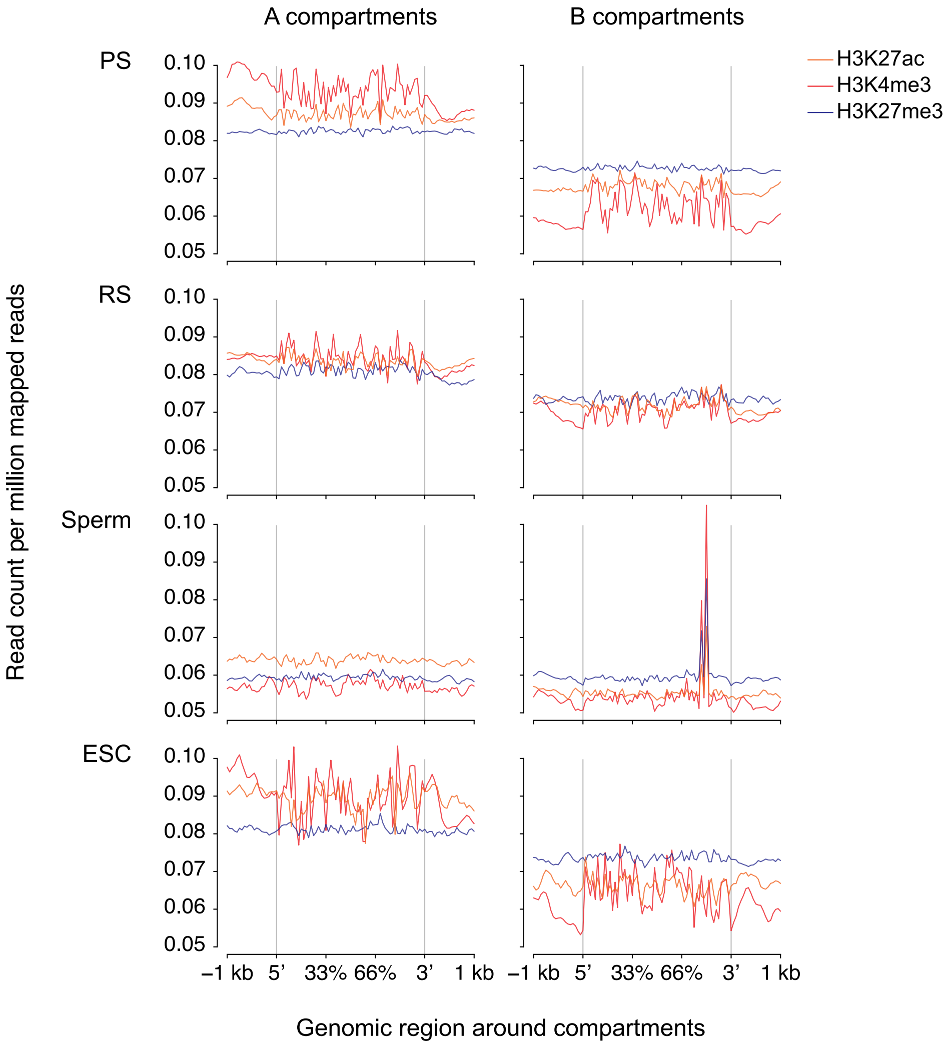

Supplementary Figure 3.4: Association of histone post-translational modifications and genomic compartments in late spermatogenesis, related to Figure 3.2.

Supplementary Figure 3.4: Association of histone post-translational modifications and genomic compartments in late spermatogenesis, related to Figure 3.2.

ChIP-seq data for H3K27ac, H3K4me3, and H3K27me3 to examine enrichment with respect to A and B compartment interiors and exteriors ± 1 kb (128-kb bins, all chromosomes) in pachytene spermatocytes (PS), round spermatids (RS), sperm, and ESCs.

See **Supplementary Dataset 3**.

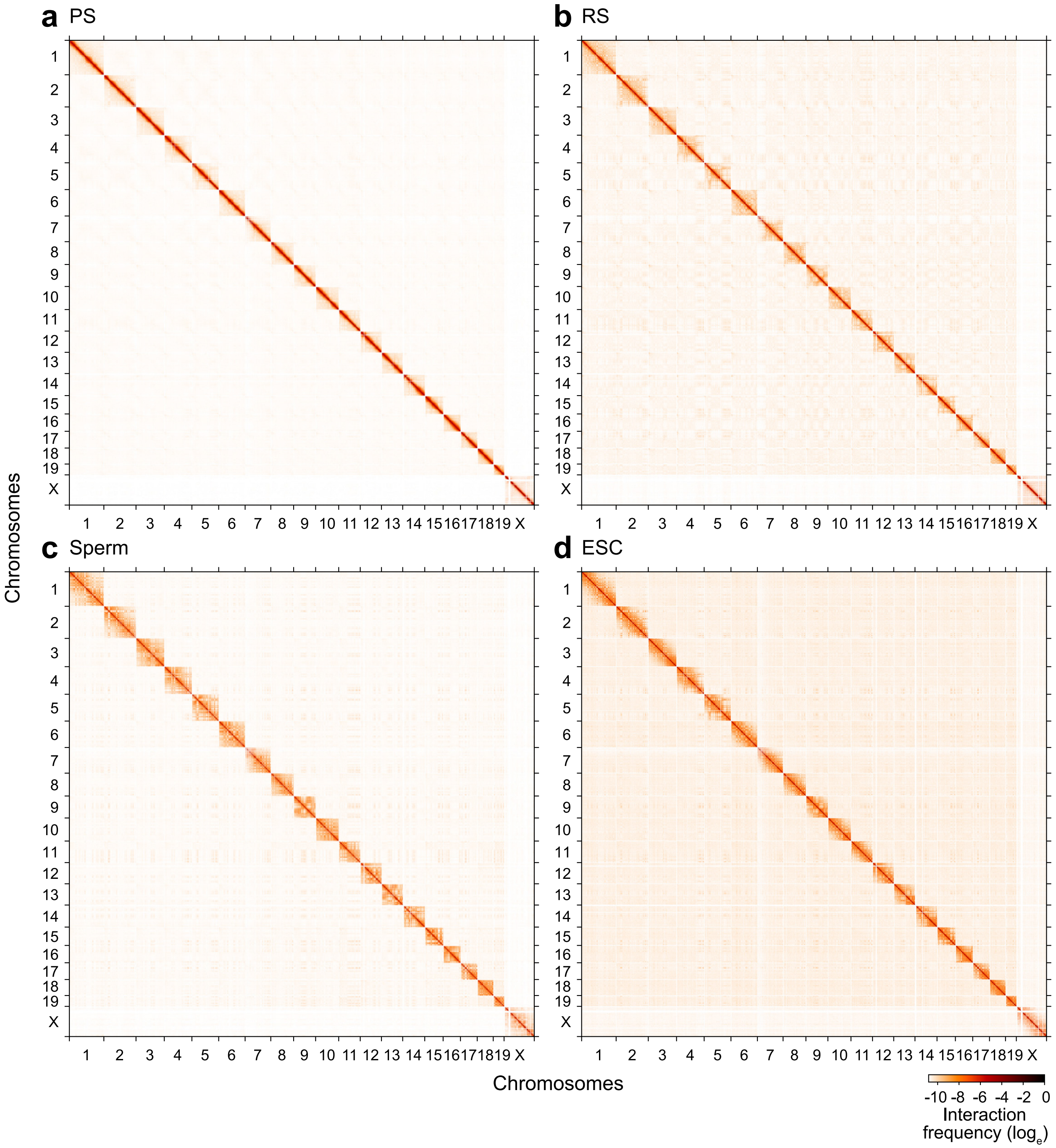

Supplementary Figure 3.5: Interchromosomal interactions in late spermatogenesis, related to Figure 3.3.

Supplementary Figure 3.5: Interchromosomal interactions in late spermatogenesis, related to Figure 3.3.

a–**d**, Heatmaps showing genome-wide normalized Hi-C interaction frequencies (250-kb bins) in pachytene spermatocytes (PS; **a**), round spermatids (RS; **b**), sperm (**c**), and ESCs (**d**).

a PS

Number of called TADs	2,279
Mean ± SE TAD size	1,110 ± 23.8 kb
Median TAD size	740 kb
10th percentile	240 kb
25th percentile	380 kb
75th percentile	1,440 kb
90th percentile	2,400 kb

RS

Number of called TADs	2,212
Mean ± SE TAD size	1,130 ± 22.6 kb
Median TAD size	800 kb
10th percentile	220 kb
25th percentile	400 kb
75th percentile	1,480 kb
90th percentile	2,460 kb

Sperm

Number of called TADs	4,520
Mean ± SE TAD size	562 ± 7.51 kb
Median TAD size	400 kb
10th percentile	200 kb
25th percentile	280 kb
75th percentile	640 kb
90th percentile	1,060 kb

ESC

Number of called TADs	4,008
Mean ± SE TAD size	632 ± 8.90 kb
Median TAD size	480 kb
10th percentile	220 kb
25th percentile	300 kb
75th percentile	780 kb
90th percentile	1,200 kb

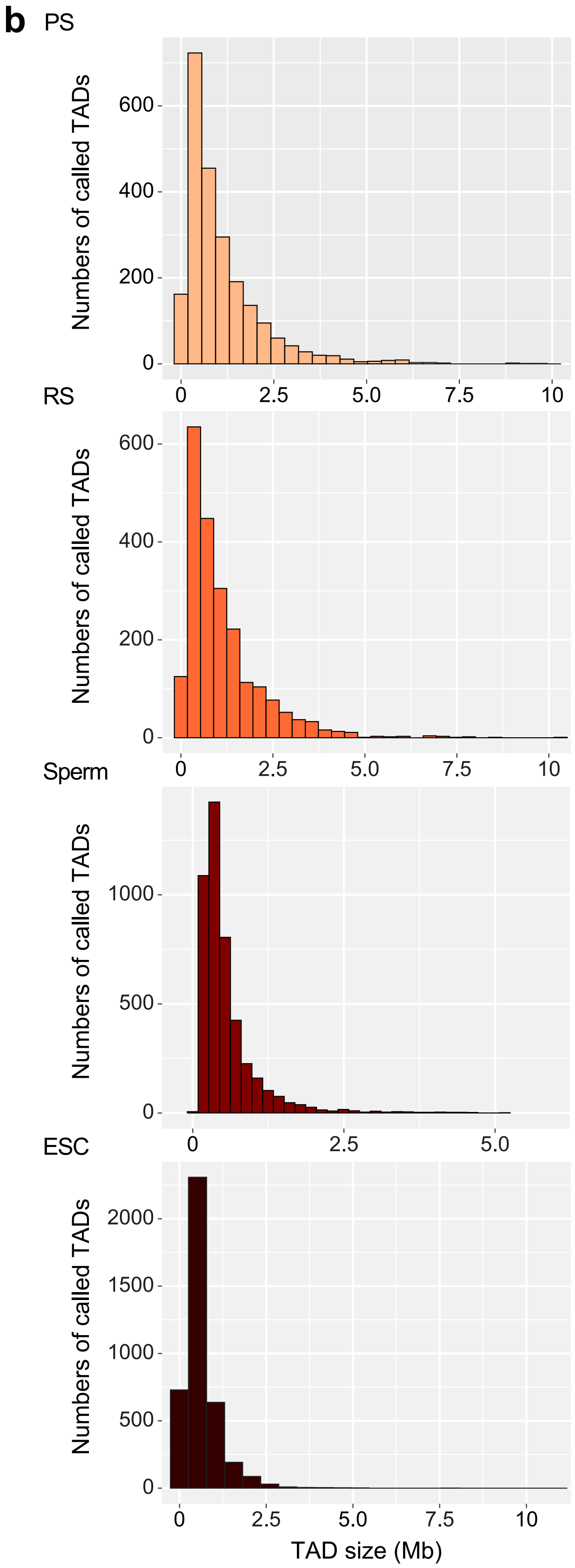

Supplementary Figure 3.6: Topologically associating domains in late spermatogenesis, related to Figure 3.4.

Supplementary Figure 3.6: Topologically associating domains in late spermatogenesis, related to Figure 3.4.

a, Numbers of TADs called with the software package HiCExplorer (**Materials & Methods**) along with derived statistics for TAD size distributions for pachytene spermatocytes (PS), round spermatids (RS), sperm, and ESCs. SE: standard error.
b, Size distribution histograms for TADs.

See **Supplementary Dataset 4**.

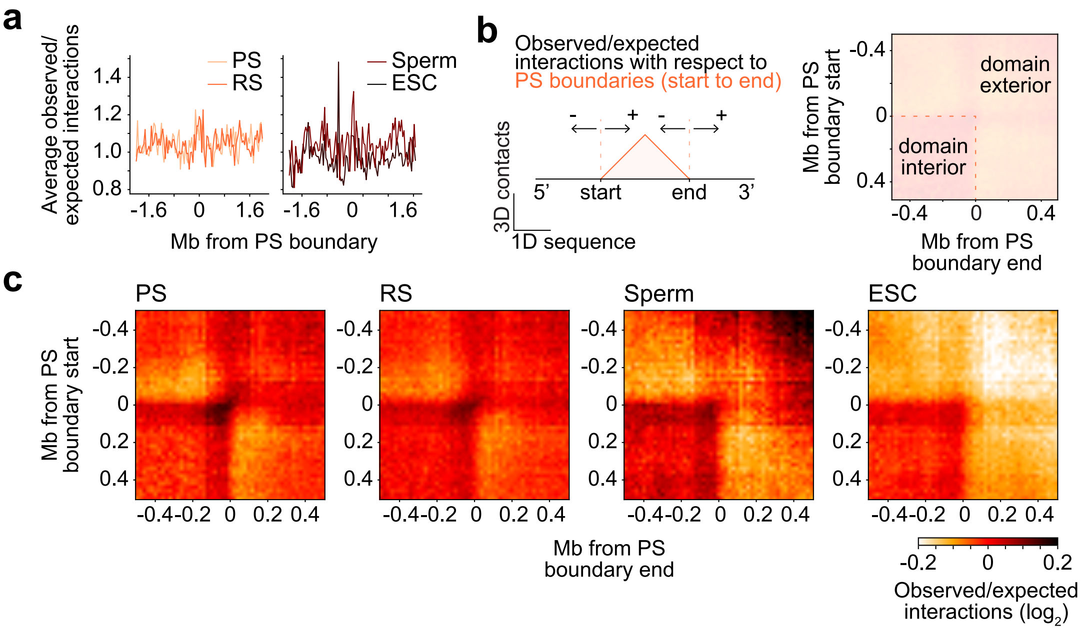

Supplementary Figure 3.7: A subset of weak topologically associating domain boundaries apparent in pachytene spermatocytes is maintained in sperm, related to Figure 3.4.

Supplementary Figure 3.7: A subset of weak topologically associating domain boundaries apparent in pachytene spermatocytes is maintained in sperm, related to Figure 3.4.

a, Average observed/expected interaction frequencies at pachytene spermatocyte TAD boundaries ± 2 Mb (20-kb bins, chromosome 2) for pachytene spermatocytes (PS), round spermatids (RS), sperm, and ESCs.

b, Schematic for interpretation of 2D matrix visualizations of observed/expected interaction frequencies at pachytene spermatocyte TAD start and stop boundaries.

c, 2D matrix visualizations of $\log_2$ observed/expected interaction frequencies at pachytene spermatocyte TAD start and stop boundaries ± 0.5 Mb for all cell types (20-kb bins, all chromosomes).

See **Supplementary Dataset 4**.

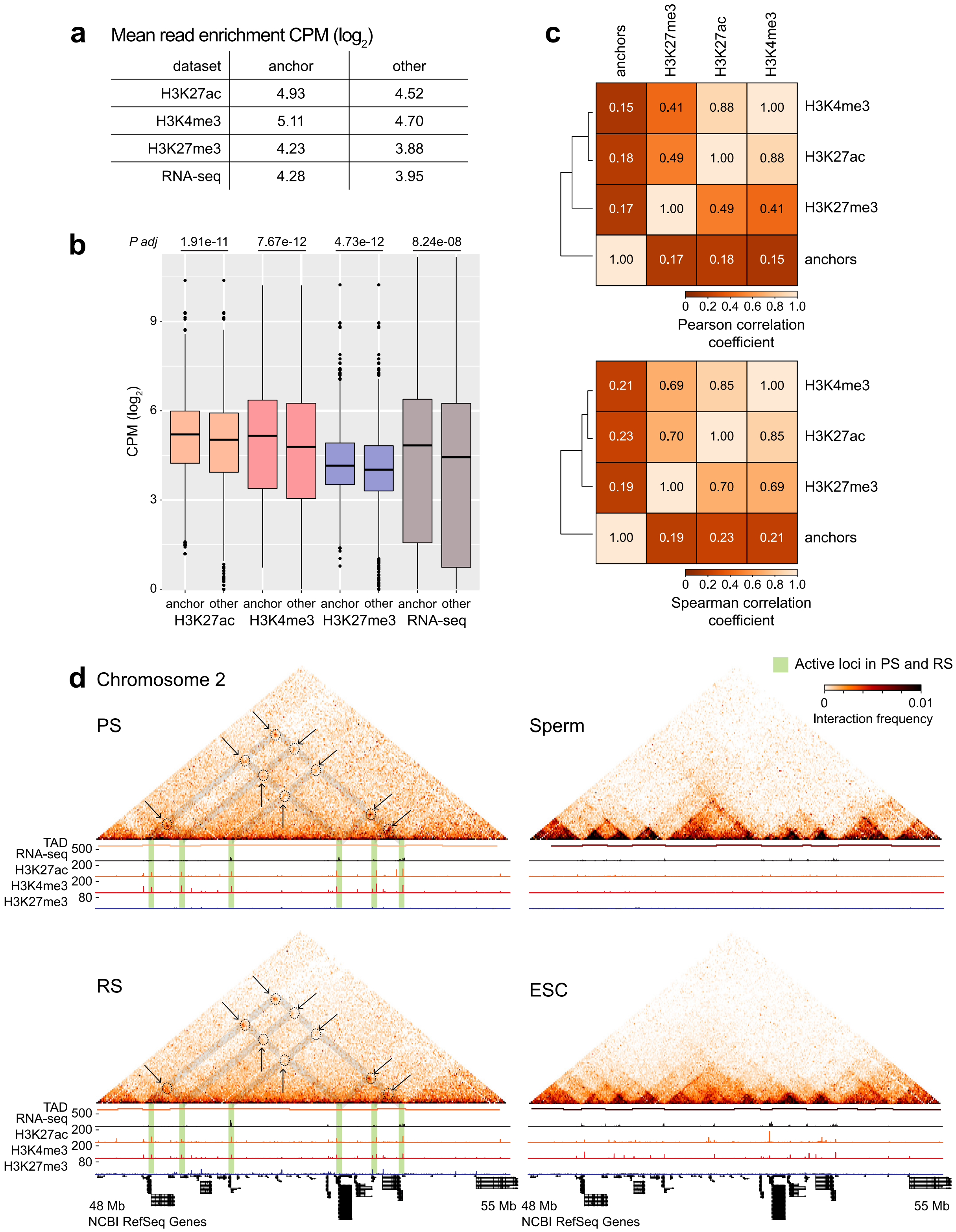

Mean read enrichment CPM ($\log_2$)

dataset	anchor	other
H3K27ac	4.93	4.52
H3K4me3	5.11	4.70
H3K27me3	4.23	3.88
RNA-seq	4.28	3.95

Pearson correlation coefficient

	anchors	H3K27me3	H3K27ac	H3K4me3
H3K4me3	0.15	0.41	0.88	1.00
H3K27ac	0.18	0.49	1.00	0.88
H3K27me3	0.17	1.00	0.49	0.41
anchors	1.00	0.17	0.18	0.15

Spearman correlation coefficient

	anchors	H3K27me3	H3K27ac	H3K4me3
H3K4me3	0.21	0.69	0.85	1.00
H3K27ac	0.23	0.70	1.00	0.85
H3K27me3	0.19	1.00	0.70	0.69
anchors	1.00	0.19	0.23	0.21

Supplementary Figure 3.8: Pairwise point interactions and active transcription during late spermatogenesis, related to Figure 3.5.

Supplementary Figure 3.8: Pairwise point interactions and active transcription during late spermatogenesis, related to Figure 3.5.

a, Average read enrichments in $\log_2$ counts per million (CPM) from ChIP-seq data for H3K27ac, H3K4me3, and H3K27me3, and RNA-seq data at sites of pachytene spermatocyte pairwise point interaction anchors ("anchors") and all sequenced regions of the genome excluding anchor regions ("other").

b, Box-and-whisker plots in the style of Tukey showing the distributions of $\log_2$ counts per million for the datasets at "anchor" and "other" regions. Numbers along the top indicate the adjusted *P* values from Wilcoxon rank sum tests, with Bonferroni posttests, between "anchor" and "other" regions. Statistics were derived from n = 1 sample pooled from 2 biologically independent samples.

c, Hierarchical clusters of the "anchor," ChIP-, and RNA-seq datasets after Pearson (top) and Spearman (bottom) correlation calculations.

d, Hi-C interaction heatmaps (20-kb bins, chromosome 2, 48-55 Mb) for pachytene spermatocytes (PS), round spermatids (RS), sperm, and ESCs showing the dynamics of local interactions of active gene loci together with RNA- and ChIP-seq data. y axis: RPKM. Solid bars: TADs called with the software package HiCExplorer (**Materials & Methods**). Green and grey highlights, arrows, and dashed circles indicate localized pairwise point interactions and related features of interest.

See **Supplementary Dataset 5**.

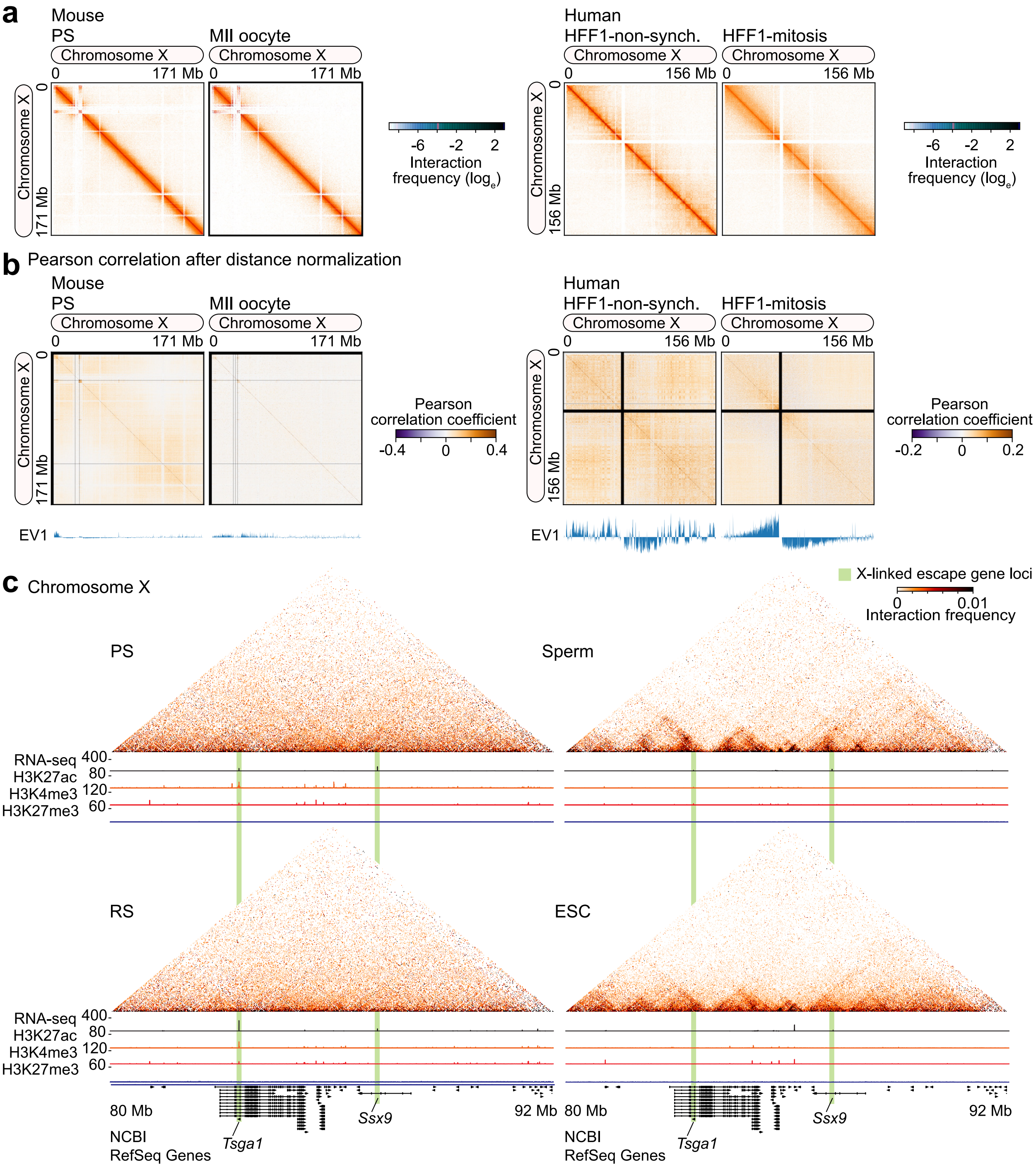

Supplementary Figure 3.9: Chromosome X is lacking in higher-order chromatin organization in late spermatogenesis, related to Figure 3.6.

Supplementary Figure 3.9: Chromosome X is lacking in higher-order chromatin organization in late spermatogenesis, related to Figure 3.6.

a, Heatmaps showing normalized Hi-C interaction frequencies (100-kb bins, chromosome X) in pachytene spermatocytes (PS), metaphase meiosis II oocytes (MII oocyte), non-synchronized human foreskin fibroblasts (HFF1-non-synch.), and synchronized prometaphase mitosis human foreskin fibroblasts (HFF1-mitosis; HFF1-non-synch. is a control for HFF1-mitosis).

b, Pearson's correlation for Hi-C interaction frequencies (100-kb bins, chromosome X) along with eigenvector 1 (EV1) from principle component analysis.

c, Hi-C interaction heatmaps (20-kb bins, chromosome X, 80-92 Mb) showing the dynamics of local interactions of gene loci together with RNA-seq data and ChIP-seq data for H3K27ac, H3K4me3, and H3K27me3.

See **Supplementary Dataset 3**.

Supplementary Datasets

Visit the following URL to access and download **Supplementary Datasets**:

- https://www.nature.com/articles/s41594-019-0189-y#Sec35

Supplementary Dataset 1: Purity of germ cells isolated for Hi-C libraries.

Each of the four spreadsheet pages represents data for Hi-C libraries. From left to right, those libraries are for pachytene spermatocyte (PS) replicate 1, pachytene spermatocyte replicate 2, round spermatid (RS) replicate 1, and round spermatid replicate 2. Within each spreadsheet page, the columns represent, from left to right, the name of the image of the isolated germ cell fraction from sedimentation velocity at unit gravity (**Materials & Methods**), the population cell type, the library (rep: replicate), and the mean purity (**Materials & Methods**).

Supplementary Dataset 2: Details and metrics for Hi-C datasets used in this study.

The columns represent, from left to right, the dataset's full name, its abbreviated name, replicate information (if applicable), PubMed reference number for initial study, database for initial study, accession number for initial study, URL for database query, database for this study, accession number for this study, restriction enzyme used when generating the dataset, paired-end read length for sequencing, and the genome to which the reads were aligned. The remaining 13 columns represent dataset sequencing results and mapping statistics; for detailed information on the metrics, please see the *Methods* manuscript from Lajoie, Dekker, & Kaplan (2015)[176].

Supplementary Dataset 3: Genomic compartment strength calibration and first eigenvectors from principle component analyses of pooled Hi-C datasets.

The first spreadsheet page represents genomic compartment strength measurements for mixtures of the sperm Hi-C matrix and a Hi-C matrix that does not have genomic compartments (**Materials & Methods**); the genomic compartment strength measurements are for the means and standard deviations of intrachromosomal (cis) interactions, and the means and standard deviations of interchromosomal (trans) interactions. The next four spreadsheet pages contain first eigenvectors from principle component analyses of the following Hi-C datasets binned in 128-kb windows (**Materials & Methods**): pachytene spermatocyte (PS), round spermatid (RS), sperm, and embryonic stem cell (ESC); EV1: first eigenvector. The final four spreadsheet pages contain first eigenvectors from principle component analyses of the following Hi-C datasets binned in 100-kb windows (**Materials & Methods**): pachytene spermatocyte, metaphase meiosis II oocyte (MII oocyte), non-synchronized human foreskin fibroblast (HFF1-non-synchronized), and synchronized prometaphase mitosis human foreskin fibroblast (HFF1-mitosis; HFF1-non-synchronized is a control for HFF1-mitosis).

Supplementary Dataset 4: Information for topologically associating domains: boundaries, boundary intersections between datasets, sizes, and derived statistics.

The first three spreadsheet pages contain the genomic locations of topologically associating domain (TAD) boundaries ± 30 kb (60 kb centered on each boundary; Methods) for the following datasets: pachytene spermatocyte (PS), round spermatid (RS), and sperm. The fourth spreadsheet page contains the results from the evaluation of TAD boundary intersections via the program UpSetR (**Materials & Methods**). The fifth through eighth spreadsheet pages contain information for the genomic locations of TAD start and stop positions, the initial separation scores for TADs (**Materials & Methods**), and individual TAD sizes for the following datasets: pachytene spermatocyte, round spermatid, sperm, and embryonic stem cell (ESC). The final spreadsheet page contains derived statistics for TAD sizes for the datasets.

Supplementary Dataset 5: Pairwise point interactions in pachytene spermatocytes.

The first spreadsheet page contains genomic location information for anchors of pairwise point interactions; each point interaction has two anchors, and each anchor has a start and stop position. The sixth column contains the binomial *P* value calculated by the point interaction calling program cLoops (**Materials & Methods**). The second spreadsheet page contains genomic location information for the center of each point interaction's anchor (**Materials & Methods**).

Chapter 4

The higher-order chromatin organization of pachytene spermatocytes from three perspectives: A Rashomon effect

Kris G. Alavattam[1,2,3]

[1]Graduate Program in Cancer and Cell Biology, Department of Cancer Biology, University of Cincinnati College of Medicine, Cincinnati, OH, USA

[2]Division of Reproductive Sciences, Division of Developmental Biology, Perinatal Institute, Cincinnati Children's Hospital Medical Center, Cincinnati, OH, USA

[3]Department of Pediatrics, University of Cincinnati College of Medicine, Cincinnati, OH, USA

Introduction

In something of an epistemological quirk, there are multiple valid ways to describe scientific truths. Speaking on the Law of Gravitation in a 1964 lecture[235], the physicist Richard Feynman remarked on this, "One of the amazing characteristics of nature is this variety of interpretational schemes." This variety constitutes what is sometimes called a "Rashomon effect," so named for Akira Kurosawa's 1950 film *Rashomon*[236]. In *Rashomon*, multiple characters detail alternative versions of an impactful event (to say the least) after the fact, their perspectives guided by their histories, goals, and biases. An explicit definition, formulated in the context of film and communication studies, states that a Rashomon effect arises from differences in perspective in combination with "equally plausible accounts, with the absence of evidence to elevate one above others, with the inability to disqualify any particular version of the truth, all surrounded by the social pressure for closure on the question"[237]. It is reasonable to adapt the definition to other research disciplines, such as physics and molecular biology, even though the "absence of evidence" is—at least in the context of this dissertation—replaced by its presence in the form of openly available raw and processed data, and transparent and rigorous data analyses; perhaps, too, the "social pressure for closure" manifests as pressure on researchers to publish quickly and/or frequently.

Drawing on Feynman's observations, a kind of Rashomon effect is at play in scientific truths—but Feynman made another observation: The effect seems to be weakened or lost if scientific laws and theories are misrepresented. "If you modify the laws much, you find you can only write them in fewer ways," he said. This variety in interpretation, despite equal plausibility, does not necessarily mean parity or equity in interpretation: Descriptions of scientific truths are judged more or less valuable for their ability to promote and sustain future developments, to generate the questions and hypotheses that fuel further research.

I begin this discussion with the Rashomon effect in mind. Here, I attempt to compare and contrast our report on the dynamics and functions of chromatin organization in spermatogenic cells (**Chapter 3**)[2] with two closely related studies published at or around the same time: Patel &

Kang et al., published in *Nature Structural and Molecular Biology* (March, 2019)[19]; and Wang & Wang et al., published in *Molecular Cell* (February, 2019)[20]. Independent of each other, and through a mixture of models, experiments, and analyses, sometimes similar, sometimes dissimilar, our three groups obtained comparable high-throughput chromosome conformation capture (Hi-C) datasets for the higher-order chromatin organization of pachytene spermatocytes. Pachytene spermatocytes are developing male germ cells in an eventful portion of meiotic prophase I; like the characters in *Rashomon*, the three teams see this same "event" from different viewpoints. And although there is overlap in our reports, we present distinct interpretations and ideas too. It is edifying to consider these differences. At the same time, I attempt to contextualize the three studies amid others that explore an ascendant model for how genomes are organized, the "loop extrusion model"[238-242]. I pursue a theme in which the three studies offer views of the loop extrusion model from different perspectives. Then, reflecting on meiotic sex chromosome inactivation with respect to the findings of both **Chapter 2** and **Chapter 3**, I consider the implications of a protracted DNA damage response on higher-order chromatin organization. Finally, I conclude this essay with more questions, and I briefly discuss potential directions for future research.

Evaluation

The three studies describe several of the same fundamental findings. So, to begin, how are the three studies similar? Remarkably, we recognize many of the same features of higher-order chromatin organization in our independent pachytene spermatocyte datasets; these include the following:

1. In the pachytene spermatocyte samples, an overwhelming prevalence of chromatin interaction probabilities within 10 Mb of the linear sequence of a chromosome's DNA:
    - **Figure 3.1**
    - Patel & Kang et al.: Figure 1

    - Wang & Wang et al.: Figures 1, 4, 5

2. Similar power-law scaling for chromatin interaction probabilities over given genomic distances[173], a revealing metric for the macromolecular organization of chromosomes:
    - **Figure 3.1**
    - Patel & Kang et al.: Figure 4; Supplementary Figure 6
    - Wang & Wang et al.: Figures 1, 6; Supplementary Figures 1, 3–5
3. The retention of chromatin compartmentalization in meiotic prophase I nuclei, in contrast to reports of mitotic prometaphase nuclei[171,174], in which chromatin compartmentalization is not observed:
    - **Figures 3.1**, **3.2**; **Supplementary Figures 3.2–3.4**
    - Patel & Kang et al.: Figures 1, 5; Supplementary Figure 4
    - Wang & Wang et al.: Figure 1; Supplementary Figures 2, 3
4. The presence of pairwise point interactions, i.e., punctate signals in Hi-C heatmaps that are associated with the activation of transcription and the interplay of gene regulatory elements[187], and which are thought to arise from the clustering of regulatory elements and genes through chromatin looping mechanisms[187]:
    - **Figure 3.5**; **Supplementary Figure 3.8**
    - Patel & Kang et al.: Figures 2, 3
    - Wang & Wang et al.: Supplementary Figure 3
5. The loss of higher-order chromatin organization of the X chromosome in pachytene spermatocytes, which coincides with meiotic sex chromosome inactivation, wherein the male sex chromosomes are transcriptionally silenced and sequestered away from transcriptionally active, recombining autosomes:
    - **Figure 3.7**; **Supplementary Figure 3.9**
    - Patel & Kang et al.: Figure 6
    - Wang & Wang et al.: Figure 3; Supplementary Figures 3, 4, 6, 7

The three studies diverge and overlap in terms of experimental design. So, in what ways are the three studies different? First, there are, of course, differences in experimental design, for example, the model organisms used, the cell types analyzed, and the methods of cell isolation:

1. Using mice, Patel & Kang et al. focused on the higher-order chromatin organization of cells in two stages of meiotic prophase I: zygotene and pachytene spermatocytes. To isolate these cells for experiments and analyses, Patel & Kang et al. pursued a strategy of spermatogenic cell synchronization. To block spermatogonial differentiation, neonatal mice at two days postpartum were treated with a compound that inhibits the synthesis of retinoic acid, an essential signaling molecule for spermatogenesis, among other developmental processes; then, to promote synchronous spermatogonial differentiation, the pups were injected with retinoic acid one week later[238]. The treated animals underwent recovery periods of various lengths[239] in order to isolate synchronized cells at the two different stages of meiotic prophase I (Patel & Kang et al.: Supplementary Figure 1; Supplementary Table 1). Using flow cytometry[240], the cells from synchronized testes were isolated and then sorted for 4C DNA content (because cells in meiotic prophase I have two complements of the diploid genome) and the accumulation of the testis-specific linker histone H1T, which is present in pachytene spermatocytes and later cell types, but not zygotene spermatocytes (Patel & Kang et al.: Supplementary Figure 1; Supplementary Table 1). Their experimental mice were drawn from the F1 generations of male CAST/EiJ × female C57Bl/6J crosses, which provide sufficient SNP density to unambiguously analyze chromatin interactions between maternal and paternal homologs (Patel & Kang et al.: Supplementary Figure 1; Supplementary Table 2). The intriguing results from these analyses are described below.
2. Using both Rhesus macaque and mouse model organisms, Wang & Wang et al. made use of the STA-PUT method for gravity sedimentation at unit velocity as described in the

literature[210,241-246]. The authors isolated mitotically proliferating spermatogonia, pachytene spermatocytes, round spermatids, sperm, and fibroblasts from adult male Rhesus macaques. For analyses of mouse meiotic prophase I, Wang & Wang et al. isolated pachytene spermatocytes from adult male mice, the F1 generations of male PWK/PhJ mice × female C57Bl/6N crosses. However, the authors found that the SNP density from this breeding strategy was too low to unambiguously analyze chromatin interactions between maternal and paternal homologs.

3. Like Wang & Wang et al., we also made use of the STA-PUT method to isolate pachytene spermatocytes and round spermatids, albeit from adult C57Bl/6J males. As such, it was not possible to distinguish interhomolog chromatin interactions with these data. (To parse interhomolog chromatin interactions, we have generated unpublished Hi-C datasets from male JF1/MsJ × female C57Bl/6J crosses for; these analyses are ongoing.) And rather than isolate and sequence new samples for sperm and unsynchronized embryonic stem cells, we made use of published high-quality datasets with similar coverages to our own: The sperm were from a CD-1 background[167], and the embryonic stem cells were derived from a male CAST/EiJ × female S129/SvJae cross[168,247].

It is important to note that these differences in experimental design are secondary to a goal shared by our three studies: to derive data for genome-wide chromatin interaction probabilities by both timepoint and cell homogeneity. So, it can be said, in that respect, our studies are unified.

The three studies diverge and overlap in terms of experimental impurities. Our studies are unified in another respect: All of the datasets are contaminated with heterogenous cells—although this contamination appears to be low: ≤10% mean impurities for many of the Hi-C datasets. More specifically, Patel & Kang et al. note that their dataset for zygotene spermatocytes has a mean purity of ~93%, while their dataset for pachytene spermatocytes has a mean purity of ~80% (Patel & Kang et al.: Supplementary Table 1). Importantly, heterogenous cell contaminants in their data are, for the most part, from cell types that are “temporal neighbors;” for example, regarding their pachytene spermatocyte dataset, the majority of heterogenous cell contaminants are from the next stage of meiotic prophase I, the diplotene spermatocyte stage. Diplotene spermatocytes comprise ~19% of the pachytene spermatocyte dataset (Patel & Kang et al.: Supplementary Table 1); for this reason, Patel & Kang et al. also refer to the pachytene spermatocyte dataset as a “late meiotic prophase I” dataset.

Regarding the study from Wang & Wang et al., in studying the reported cell isolation purity data for Rhesus macaques, the mean purities appear to be ~93% for spermatogonia, ~88% for pachytene spermatocytes, and ~90% round spermatids (Wang et al.: Supplementary Figure 1b; note that specific values are not given in the manuscript, and these values are my approximations from analyzing a data-point plot of mean ± standard error purities). No quantitative information is given for the purity of sperm and fibroblasts. Regarding the Rhesus macaque sperm dataset, a microscopy image seems to indicate high levels of purity (Wang & Wang et al.: Supplementary Figure 1b), and the brief methodological description for sperm isolation indicates that the purity is nearly 100%, consistent with other studies that used this or similar isolation methods for sperm[167,248]. No qualitative description is given for the fibroblasts, although, again, microscopy images seem to indicate high purity (Wang & Wang et al.: Supplementary Figure 1b). Wang & Wang et al. do not provide quantitative purity metrics for their mouse pachytene spermatocyte datasets (Wang & Wang et al: Figures 5, 6; Supplementary Figures 5–7); presumably, the purities are similar to those of Rhesus macaque pachytene spermatocytes isolated via STA-PUT and/or the purities of those I obtained using the same STA-PUT method. Speaking of which, I isolated mouse pachytene spermatocytes and round spermatids for the datasets analyzed in our report (**Chapter 3**)[2], and I determined that our pachytene spermatocyte dataset has a mean purity of ~91% while our round spermatid dataset has a mean purity of ~94% (**Supplementary Figure 3.1**; **Supplementary Dataset 1**). It should be noted that cell isolation via STA-PUT is based on cell density; while the cell types of meiotic prophase I evince differences in density[210], the differences between pachytene spermatocytes and diplotene spermatocytes are subtle. This raises the possibility that the datasets of Wang & Wang et al., as well as our datasets, may be affected by undetected diplotene spermatocytes, which would be similar to the pachytene spermatocyte data obtained by Patel & Kang et al.

As I consider these issues, I also ruminate on the idea that the temporal resolution of our datasets—whether from flow assisted cell sorting or STA-PUT—could be considered "coarse." Here's my reasoning: In mice, the pachytene stage, for example, is ~7 days in duration and comprised of distinct substages, as is the round spermatid stage of spermiogenesis; these time periods are ~10–11 days in Rhesus macaques. Similarly, spermatogonia are a highly heterogenous group of cells from a lengthy phase of spermatogenesis, comprised of multifarious substages. This leads me to ask the following questions: (1) By deriving our datasets from pools of cells with a variety of substages, are we unable to sufficiently capture and/or observe substage-specific features of chromatin organization? (2) Given that several substages are functionally distinct, what are we to make of population, or "bulk," chromatin interaction readouts? (3) Are we inadvertently "averaging away" timepoint-dependent features? It remains largely unknown how and to what extent the above-mentioned considerations impact the reported data, nor is it known how these factors influence our interpretations. Still, the observations from the three studies are remarkable for their similarity; even in light of these questions, analyzed on their own or with respect to each other, these studies make important contributions to the fields of reproductive and chromatin biology (see below).

Certain analytical results and interpretations set the three studies apart. Next, in looking at the three studies, I shift attention to notable variations. These largely concern our analyses and interpretations of two fundamental forms of higher-order chromatin organization: chromatin compartmentalization and chromatin topology.

Chromatin compartmentalization. First, chromatin compartmentalization: We observed that, in pachytene spermatocytes and round spermatids, genomic A/B compartmentalization is similar to that found in interphase nuclei but is "attenuated" (**Figures 3.1**, **3.2**; **Supplementary Figure 3.2–3.4**; **Supplementary Dataset 3**). Our initial observations led us to develop a new method to quantitate, measure, and compare genomic A/B compartmentalization between datasets (**Chapter 3 Materials & Methods**), allowing us to reach conclusions that the genomic A/B compartments of our pachytene spermatocyte and round spermatid datasets are indeed weaker than those of somatic interphase nuclei, unsynchronized embryonic stem cells, and sperm (**Figure 3.2**; **Supplementary Figure 3.3**; **Supplementary Dataset 3**). The studies from Patel & Kang et al. and Wang & Wang et al. also described genomic A/B compartmentalization in meiosis, although these studies diverge from ours in how they approach the descriptions, measurements, and/or interpretations. Neither Patel & Kang et al. nor Wang & Wang et al. quantified genomic A/B compartmentalization *per se*.

I will break it down: In their observations, Patel & Kang et al. note a "strong" retention of genomic A/B compartments in zygotene and pachytene spermatocytes. I suspect the discrepancy in adjectives, i.e., "strong" versus "attenuated" or "weak," between Patel & Kang et al. and the other two studies—and, more generally, the difficulty of making direct comparisons between the three studies' Pearson correlation heatmaps, the transformed data central to compartmentalization analyses—arises from the following: In visualizing their heatmaps, the color scale maxima and minima appear to not be fixed between processed Hi-C datasets. The visualizations seem to scale the unfixed maximum and minimum correlation coefficients to, respectively, the hottest and coldest colors of the heatmaps. This means that while color scale maxima and minima do not change from visualization to visualization, the Pearson correlation coefficients assigned to those colors do. For example, a brightly colored compartment in one heatmap represents, say, a positive Pearson correlation coefficient, but that positive value is undescribed and also unfixed, varying from heatmap to heatmap.

Shifting focus to Wang & Wang et al., they describe genomic A/B compartments in pachytene spermatocytes as “weak plaid patterns” (an interesting, relevant aside: Wang & Wang et al. also observe relatively weak genomic A/B compartments in their spermatogonia dataset, which represents a heterogenous population of mitotically proliferating germ cells with varying degrees of differentiation; there is no mention of genomic A/B compartmentalization with respect to their round spermatid and sperm datasets). Having made that observation, they make yet another: Drawing on the observation that chromatin interactions in pachytene spermatocytes are overwhelmingly limited to within ~10 Mb of the linear sequence of a chromosome’s DNA, the authors set out to analyze fine patterns in chromatin compartmentalization apparent at the ~10-Mb scale (Wang & Wang et al.: Figure 4; Supplementary Figures 3–6). To clearly visualize these patterns, they pursued a similar data science strategy as that used for genomic A/B compartments: They transformed their Hi-C datasets for pachytene spermatocytes to Pearson correlation matrices and then performed principle component analysis (PCA); however, instead of running this transformation on, say, whole chromosomes, as has become typical in studies of higher-order chromatin organization[173,175], Wang & Wang et al. ran the method on 10 Mb × 10 Mb matrices of interest along the linear sequence of a chromosome’s DNA. They term the compartmentalization observed in these 10 Mb × 10 Mb regions “refined A/B compartments,” and the authors demonstrate that these refined A/B compartments are a previously undescribed feature of higher-order chromatin organization enriched in pachytene spermatocytes. Through various analyses, Wang & Wang et al. show that the refined A/B compartments correlate with transcriptional activity (Wang & Wang et al.: Figure 4; Supplementary Figures 4, 5), similar to genomic A/B compartments, i.e., A compartments correlate with transcriptional activity and B compartments correlate with transcriptional inactivity. The use of this terminology and the partial overlap in definition suggests that refined A/B compartments are similar to genomic A/B compartments.

Chromatin topology. Switching from the topic of chromatin compartmentalization to the topic of chromatin topology, I reach what is perhaps the biggest difference in analysis and interpretation between our study and the others. In interpreting their interaction probability datasets for pachytene spermatocytes, both Patel & Kang et al. and Wang & Wang et al. draw a conclusion that topologically associating domains (TADs)—regions of preferential, or concentrated, chromatin interaction probabilities on the 100 kb-to-1 Mb scale[169,170,249]—are "mostly lost" (Patel & Kang et al.) and/or "undergo dissolution" (Wang & Wang et al.). In contrast, in analyzing Hi-C heatmaps, we visually observed and computationally detected the presence of faint, 1 Mb-scale triangles projecting from the linear sequence of a chromosome's DNA (**Figure 3.4**; **Supplementary Figures 3.6**, **3.7**; **Supplementary Dataset 4**; we visually detected such patterns in the datasets from the other two groups too). These observations suggest that TADs are not lost but, instead, attenuated. Considering the hundreds of thousands (Patel & Kang et al.) or millions of nuclei (Wang & Wang et al.; **Chapter 3 Materials & Methods**) that are sampled and averaged together in bulk Hi-C experiments, intra-TAD chromatin interaction probabilities are only slightly above those of inter-TAD chromatin interaction probabilities (**Figure 3.4d**; **Supplementary Figure 3.7**). This, in turn, suggests the following possibilities: (1) Small subsets of the cell population evince "strong" TADs at the time of experimental sampling, or—what may be the case—(2) larger subsets evince more attenuated TADs at the time of sampling.

Discussion

Intriguingly, the differences between our studies are not contradictory or otherwise incompatible with each other. In keeping with the definition of a Rashomon effect, all accounts are plausible, and in a compelling example of the effect, our variations in data interpretation give multiple perspectives on an important conceit in chromatin biology: the loop extrusion model[250-254].

Loop extrusion informs our understanding of pachytene chromatin organization. Before explaining how, I will take a moment to introduce the loop extrusion model, which seeks to address how chromatin loops are formed—until recently, a longstanding question in cell biology. The model puts forward that cohesin—a ring-shaped, multi-subunit protein complex implicated in the cohesion of sister chromatids[255,256] and gene expression[257,258]—entraps a small loop, or multiple small loops, of chromatin inside its proteinaceous lumen; then, through progressive, processive extrusion, the loops are enlarged up to the Mb scale[252]. In this model, the colocalization of cohesin with the transcription factor/insulator protein CTCF limits further extrusion[251,254,259-262]: Chromatin loops are formed almost exclusively between "convergent" CTCF-bound consensus sequences—or motifs—i.e., those bound by CTCF and pointing toward each other with respect to the linear sequence of a chromosome's DNA[187,249,263,264]. The specificity of orientation appears to ensure that CTCF-binding sites come together in 3D space[254,265,266], which is consistent with the widely reported presence of cohesin at CTCF sites as well as the widely reported presence of convergently oriented CTCF-binding sites at the bases of chromatin loops[187,267-269]. The loop extrusion model predicts that, in extruding chromatin loops through its lumen, cohesin directly or indirectly "scans" the linear sequence of a chromosome's DNA to detect the orientations of CTCF-bound motifs, stalling or halting in the presence of two CTCF-bound motifs in convergent orientation with respect to each other. Thus, the loop extrusion model has the potential to explain not only pairwise point interactions but also the organization of chromosomes into TADs, which are often bordered by convergent CTCF-bound motifs[169,170,187,264,267,270].

To reiterate, we observed what appears to be the presence of faint TADs in our and the others' pachytene spermatocyte datasets, in addition to pairwise point interactions and extensive numbers of near-cis intrachromosomal interactions ≤10 Mb from the linear sequence of a chromosome's DNA. The loop extrusion model suggests functional linkage between these observations: Given that they are often flanked by convergent CTCF-bound motifs, it has been proposed that TADs are "loops in progress," i.e., collections of smaller loops formed from ongoing cohesin processivity, thereby giving rise to the hallmark sign of TADs in Hi-C heatmaps: the small triangle-shaped increases in chromatin interaction probability proximal to the linear sequence of a chromosome's DNA (**Figure 3.4b**; **Supplementary Figure 3.8d**). Importantly, it is not understood how CTCF functions to flank TADs; perhaps a mechanism involving steric hindrance is at play, or perhaps cohesin and CTCF interact via direct or indirect covalent binding. Nonetheless, it is known that the boundaries formed by convergent CTCF sites are not absolute and cohesins can extend beyond them, although the mechanisms underlying this phenomenon are not well understood. For example, a growing body of work indicates that methylation or mutation of CTCF-binding motifs can prevent the binding of CTCF to DNA, facilitating the cohesin-mediated extrusion of chromatin beyond convergent motifs[271,272]. More recent work has suggested that cohesin is subject to rapid turnover[260], limiting the timespan for cohesin-chromatin interactions and, thus, loop extrusion. Under conditions where cohesin turnover is prolonged or stopped, cohesin appears to progress beyond convergent CTCF-bound motifs[201,273,274]. Under such conditions, chromosomes in cultured somatic cells have been observed to condense into a conspicuous structural conformation termed *vermicelli* (Italian for, literally, "little worms")[274], which, similar to chromosomes in meiotic prophase I, evince cohesin-predominated chromosome axes from which chromatin loops furl outwards.

With that in mind, given the strengths of their signals in our pachytene spermatocyte datasets, pairwise point interactions may represent a non-random, transcription-associated class of "completed" or "condensed" loops, i.e., those resulting from persistent cohesins that have moved beyond convergent CTCF-bound motifs to extrude as much chromatin as they can before constraint at, presumably, meiotic chromosome axes. Finally, the presence of extensive near-cis intrachromosomal interactions may indicate a chromatin topology predominated by randomly distributed loop positions in various stages of completion and, thus, of variable lengths; such a possibility is consistent with our observation of attenuated TADs. Indeed, Patel & Kang et al. performed calculations to ascertain the lengths of chromatin loops in their zygotene and pachytene spermatocyte datasets, finding that average loop lengths in the zygotene stage, 0.8–1 Mb, extend to 1.5–2 Mb in the pachytene stage (Patel & Kang et al.: Figure 4). This suggests a period of prolonged, global loop extension in meiotic prophase I.

Loop extrusion affects the strength of genomic A/B compartmentalization. Intriguingly, loop extension is associated with the strengths of genomic A/B compartments. The acute depletion of cohesin causes the potentiation and fragmentation of genomic A/B compartments[201,202,273,275]. On the other hand, *in silico* models for prolonged cohesin-chromatin interactivity show the apparent attenuation of genomic A/B compartments[253]. Keeping these findings in mind, it has been proposed that cohesin regulates the overall flexibility of chromosomes[201], e.g., chromosomes become more flexible with the depletion of cohesin: Distal portions may bend into contact with each other at higher probabilities, giving rise to stronger genomic A/B compartments; on the other hand, prolonged cohesin-chromatin interactions may promote the relative rigidity of chromosomes, resulting in attenuated genomic A/B compartments.

Evidence from Patel & Kang et al. allows further insight into the putative relationship between chromosome flexibility and genomic A/B compartmentalization: By generating genome-wide chromatin interaction probability maps using only contacts between paternal and maternal homologs, the authors detected strong chromatin interaction signals along the diagonal of zygotene and pachytene spermatocyte intrachromosomal maps, an explicit indication that homologs are tightly aligned along their length (Patel & Kang et al.: Figure 4; Supplementary Figure 7). What's more, preferential associations between genomic A/B compartments, depicted as pronounced "plaid" patterns along the diagonal, were apparent in the maps of interhomolog interaction probabilities (Patel & Kang et al.: Figure 4; Supplementary Figure 7). This led the authors to posit a model whereby the chromatin loops of paired homologs are thoroughly interdigitated (Patel & Kang et al: Figure 4), facilitating the self-association of A and B compartments between paternal and maternal homologs. Relatedly, discrete "X-like" patterns for interchromosomal chromatin interaction probabilities were reported in our data (**Figure 3.3**) and the data of Patel & Kang et al. (Patel & Kang et al.: Supplementary Figures 1, 3); and although not directly reported in the study from Wang & Wang et al., these patterns are observable when visualizing their datasets (data not shown). It is interesting to speculate that this pattern may result from condensed chromosomes—their loops extensively extruded and interdigitated between homologs—with respect to each other in the space of a nucleus. Our observations of relatively strong interchromosomal interactions between A compartments (**Figure 3.3**)—even in light of the condensed state of pachytene chromosomes—could support such an assertion.

Does a DNA damage response alter the higher-order chromatin organization of the meiotic sex chromosomes? Among the most fascinating findings from the three studies, the pachytene spermatocyte X chromosome appears to lack A/B compartmentalization altogether. Indeed, the pachytene X chromosome evinces few, if any, of the contact probability patterns typical of bulk Hi-C experiments using interphase cells or, considering autosomes only, pachytene spermatocytes; for example, neither TADs nor pairwise point interactions are apparent on the pachytene X chromosome.

To begin to understand this, there is much to consider about the male sex chromosomes in meiotic prophase I. For one, it is important to note that the X and Y chromosomes must negotiate meiotic prophase I amid nuclei in extreme—albeit highly ordered—flux. This nuclear dynamism is something truly remarkable: This is a nuclear environment where hundreds of programmed DNA double-strand breaks (DSBs) rend the genome to initiate meiotic recombination; where DNA damage response (DDR) signals, driven at first by the serine/threonine kinase ATM, cascade and propagate through the nucleus to facilitate homologous recombination repair; where, in response, vast, interrelated protein networks descend upon chromatin to promote the careful synapsis of homologous sequences and homology search; where, too, immense protein polymers assemble to form the synaptonemal complexes that align and stabilize homolog pairs, working in concert with myriad chromatin structural complexes in the midst of loop extrusion; and where downstream DSB repair takes place, a part of which facilitates genetic crossovers between homologs—crossovers that will, in the short term, enable proper segregation at meiotic anaphase I and, in the long term, promote genetic diversity in offspring[55,56].

In the midst of such intense activity, the structures of X and Y ensure their distinct regulation. This is because, unlike homomorphic autosomes, whose homologs can pair and synapse along their entire lengths, the male sex chromosomes are heteromorphic, pairing and synapsing at only a small region of homologous sequence called the pseudoautosomal region. The remaining unsynapsed sex chromatin, then, encounters something of a genomic tripwire: Through a mechanism termed "meiotic silencing of unsynapsed chromatin" (MSUC), the nucleus mounts a defense of genomic integrity that sees the transcriptional repression of unsynapsed chromatin—whether autosomal or sex chromosomal—in both male and female meiosis[74,78,81]. To facilitate equal distributions of genetic material in gametes, recombining homologous chromosomes need to precisely synapse and, later, segregate; so it is that the genome defense mechanisms of meiotic prophase I have adapted to recognize chromosome asynapsis as a breach of genomic integrity[63-65].

Evidence suggests MSUC is adapted from a DDR pathway driven primarily by the activity of ATR, a kinase closely related to ATM[63,78,81,140]. ATR is a serine/threonine kinase that, like ATM, phosphorylates serine 139 of histone H2AX (γH2AX); but, unlike ATM, which acts on H2AX surrounding DSBs, ATR acts on H2AX at and around the sites of stalled DNA replication forks and single-stranded DNA overhangs. Regarding the male sex chromosomes in meiosis, the growing consensus is that a feedforward molecular mechanism centered on ATR, in complex with TOPBP1 and other DDR factors, works with BRCA1 to promote the spreading of γH2AX along X- and Y-chromosome axes; at nearly the same time, the ATR complex works with MDC1 to promote the spreading of γH2AX through X- and Y-chromatin loops[62-64,71,73,76,276-278].

This ATR-mediated propagation of γH2AX through the sex chromatin is at the heart of a key regulatory event considered a special instance of MSUC: meiotic sex chromosome inactivation (MSCI). A molecular mechanism essential to the viability of germ cells and, thus, male fertility[62,65,66], MSCI results in the transcriptional silencing of X and Y, and the subsequent sequestration of X and Y away from recombining, transcriptionally active autosomes. The sex chromosomes are eventually positioned at the periphery of spermatocyte nuclei in a well-bounded, semi-heterochromatic structure, or domain, termed the “XY body” (also known as the “sex body”). Subsequent steps in the MSCI mechanism facilitate epigenetic programming and chromatin remodeling of the domain, including the deposition of numerous histone post-translational modifications—both active and repressive—as well as other chromatin modifications[3,67-75].

Whereas pachytene spermatocyte autosomes display many of the contact probability patterns typical of bulk Hi-C experiments, the pachytene spermatocyte X chromosome does not. So, the existence of the XY body raises thought-provoking questions: Does a genome defense mechanism promote a chromosome-wide chromatin organization scheme that is near-patternless? If so, then how? And what could be the purpose of such an organization scheme? The answers may lie in a physical phenomenon called “phase separation,” a process by which membraneless organelles form and behave as liquid droplets[205,206]; heterochromatin, for example, has been proposed to form through phase separation[207,208,279]. It could be that an ATR-driven, chromosome-wide DDR initiates a phase separation mechanism that sees the X and Y chromatin coalesce into a self-associating, droplet-like domain that lacks several obvious features of higher-order chromatin organization, including TADs and genomic A/B compartments.

Interestingly, the links between DDR signaling and phase separation have precedents: Recent studies of the DDR found that, in somatic cells within the G1 phase of the cell cycle, DSBs induced within transcribing genes, or within the promoters of transcribing genes, tend to mobilize and cluster together in distinct, liquid-like chromatin domains [280-283]. This clustering is largely restricted to cells in the G1 phase, when chromatin is reported to be relatively mobile in comparison to other phases of the cell cycle[284-286]. This enhanced chromatin mobility is thought to enable the clustering of DSBs, emblematic of a biophysical state in nuclei that, upon exiting M phase, facilitates the reestablishment of higher-order chromatin organization[287]. Furthermore, it was found that the clusters of DSBs persist through S phase—with its extensive DNA replication, histone biogenesis, and chromatin remodeling—into G2 phase. Nuclei in G2 phase, like nuclei in meiotic prophase I, contain double complements of the diploid genome; it is thought, then, that the persistence of chromatin-domain clusters is part of an overarching mechanism in which transcriptionally active genes rely on additional, newly replicated DNA as a template for homologous recombination repair, which is otherwise suppressed in G1 phase[283,288,289]. This, in turn, sidesteps the problems associated with the relatively error-prone, potentially mutagenic repair mechanism favored in G1 phase, nonhomologous end joining repair, which anneals the ends of DSBs without respect to templates. Thus, based on a growing body of observations in the literature, I submit that self-associating, droplet-like chromatin domains facilitate distinct environments for DDR mechanisms.

However, the DDR that initiates MSCI is distinct from the somatic response to DSBs in G1 phase. How, then, is a response to chromatin asynapsis related to a response to DSBs? To address this, it is important to consider certain nuances of the DDR prior to and during XY body formation. Consider that, in the beginning of meiotic prophase I, ATM catalyzes the phosphorylation of H2AX in response to hundreds of DSBs, generated by a topoisomerase II-like enzyme called SPO11, distributed throughout the genome[58,140]. Beginning in the zygotene stage, ATR catalyzes successive, overlapping waves of H2AX phosphorylation on unsynapsed chromosome axes in response to putative single-strand or single-strand-like DNA structures[63]. Taken together, these single-strand DNA structures are likely to persist at the sites of what were once SPO11-dependent DSBs[137]; this is perhaps, in part, a consequence of the DNA double-strand resectioning necessary to form the single-stranded, DNA-protein nucleofilaments—bound by recombinases such as RAD51—that mediate homology search. This raises the possibility that, in the pachytene stage, DSBs prefigure the localization of MSUC factors on unsynapsed sex chromosome axes. In support of this idea, it was reported that, in *Spo11*-deficient spermatocytes, in which chromosomes undergo aberrant synapsis in the absence of programmed DSBs[136,140], a small number of DSBs arise and persist in the absence of programmed breaks[136]. Interestingly, these breaks colocalize with transcriptionally inactive XY body-like domains enriched with γH2AX, ATR, and other DDR factors—termed "pseudo-sex bodies" because their localization in the genome is not limited to XY—indicating that DSBs trigger the localization of ATR-driven DDR signaling that gives rise to MSUC[76,136]. Related to this, another influential study is revealing[290]: In dissecting conditions that favor homologous recombination repair in yeast, the study's authors sought to determine what becomes of DSBs when sequence homology is not found; using a genetic system to generate an irreparable DSB, the authors observed the chromosome-wide propagation of DDR signals such as RAD51. Drawing on all of this, then, our lab has proposed that persistent DSBs constitute "an evolutionarily conserved cue for the amplification of DDR factors" and, under conditions where sequence homology is not readily found, such amplification can propagate chromosome-wide[76].

I submit, then, after distinct waves of ATM- and ATR-catalyzed H2AX phosphorylation in early meiotic prophase I, the ATR-mediated propagation of DDR signaling through the pachytene sex chromosomes promotes the formation of a membrane-free, liquid-like droplet that is devoid of genomic A/B compartments, TADs, and other obvious features of higher-order chromatin organization. Since electrostatic interactions are at the heart of phase separation events[279,291], extensive accumulation of negative charges caused by γH2AX may be essential for the formation of a liquid-like XY body. In making this argument, I draw on the following findings: In mouse models deficient for *Mdc1*, an XY body fails to form, because, although DDR signaling can occur along the axes of the sex chromosomes, DDR signaling cannot propagate through XY chromatin loops[63]; in mouse models deficient for *Brca1*, XY bodies largely fail to form because DDR signaling along XY axes is aberrant, as is DDR signaling through XY chromatin loops[73,76]. Similar findings were observed in mouse models with inducible deficiencies for *Atr* and *Topbp1*[71,276,278]. This has interesting implications, including the notion that the deposition of various DDR factors that bind the XY axes, such as BRCA1, and that bind both the axes and chromatin loops of XY, such as ATR and TOPBP1, may be key to the coalescence of XY bodies.

Notably, it was proposed that X chromosome inactivation, a molecular mechanism specific to females that equilibrates X-linked gene dosage between the two sexes, also occurs via a phase separation mechanism[192]. However, the mechanism of X chromosome inactivation hinges on the activity of an X-linked long non-coding RNA, *Xist*, which, through chromosome-wide binding to X chromatin, facilitates a cascade of chromatin changes, including the deposition of various heterochromatic histone post-translational modifications and changes to DNA methylation. Not unlike the inactive male X in the pachytene stage of meiotic prophase I, the female inactive X has a higher-order organization scheme distinct from autosomes (and the active X chromosome): X is folded into two “mega-domains” [187,189-191] that are established via a step-wise mechanism[192]. Yet the inactive male X appears to lack obvious features of higher-order chromatin organization: Besides its distinct chromosome territoriality, there are few-to-no signs of, say, TADs, pairwise point interactions, refined compartments, or genomic A/B compartments. Thus, it is intriguing to consider that the activity of multiple DDR factors—propagating in a feedforward mechanism through the sex-chromosome axes and chromatin—phase-separate the male meiotic sex chromosomes, giving rise to a nuclear domain with an apparently near-patternless chromatin organization scheme.

What is the function of such a domain? A phase-separated XY body may serve as a microenvironment for the function of DDR factors, chromatin remodelers, and other factors associated with MSCI—while also excluding non-essential factors. In the course of MSCI, the sex chromosomes are subject to numerous forms of epigenetic programming. For example, as described in **Chapter 2**, a broad Fanconi anemia-DDR network regulates the deposition of epigenetic marks such as histone H3 lysine 9 di- and trimethylation (H3K9me2/3), heterochromatic histone post-translational modifications associated with the transcriptional repression of the pachytene and post-pachytene sex chromosomes; and histone H3 lysine 4 dimethylation (H3K4me2), a euchromatic histone post-translational modification associated with the transcriptional activation of sex chromosome-linked genes in the round spermatid phase of spermatogenesis, an essential event that facilitates the later steps of sperm development. Consistent with the putative phase separation of the XY body, the formation of heterochromatin is proposed to result from phase separation[207,208] and, during the initial coalescence of the XY body, XY chromatin is enriched with heterochromatic H3K9me3; however, this mark is lost in the middle phases of the pachytene stage only to return when pachytene spermatocytes progress into the subsequent diplotene stage of meiotic prophase I. This is presumably due to the replacement of H3.1/H3.2 histones with H3.3[75], after which H3K9me3 is deposited along with other heterochromatic histone post-translational modifications and proteins. It is possible, then, that other forms of functionally significant epigenetic programming—beyond, for example, the deposition of H3K4me2 for downstream sex-linked transcription—are facilitated by the unique chromatin environment of the XY body. I speculate that the near-patternless organization scheme of the X chromosome indicates both cause and consequence of the molecular machinery—needed in what may be stupendous amounts—that executes the chromosome-wide confluence of biological activity. With all of this in mind, it is interesting to consider that, as early as the pachytene stage, XY chromatin may be epigenetically programmed to transmit functionally significant biological information to the next generation; this includes, for example, information for imprinted X-inactivation, i.e., following fertilization, the selective inactivation of paternally derived X chromosomes during the course of embryogenesis[292].

Taking it all together, then, I propose that the putatively phase-separated XY body—sequestered apart from the recombining and transcriptionally active autosomes, and lacking the contact probability patterns typical of bulk Hi-C experiments—provides an environment that is physically, energetically favorable tor extensive epigenetic programming by DDR and chromatin remodeling networks—some in cooperation and/or reliance with each other, some not—to encode vital and heritable information in the XY chromatin.

Questions

In reflecting on this research, many questions come to mind. Here are some samples: If prolonged loop extrusion processivity is indeed driving the formation and/or maintenance of meiotic chromosomes, and thereby the attenuation of genomic A/B compartments, then in what ways is that functionally significant? And what are the specific functions of other architectural factors besides cohesin—such as CTCF and condensin, a protein complex that shares many subunits with cohesin—in the higher-order chromatin organization of pachytene spermatocytes and subsequent cell types? Meiosis and post-meiotic cell types are home to germline-specific variants of CTCF and cohesin/condensin subunits[203,204]: What are their functions in higher-order chromatin organization and gametogenesis? And what about attenuated TADs, which are reported to form from putative loops in progress? Is perhaps some portion of them not formed in this way? Have we unknowingly observed TADs or TAD-like forms of local topology that arise from some CTCF-independent means? And what about refined A/B compartments as reported by Wang & Wang et al.? Like genomic A/B compartments, are they correlated with looping mechanisms too? Building on our proposal that higher-order chromatin organization in meiotic prophase I is, itself, a form of epigenetic reprogramming, are heritable features of topology and/or compartmentalization passed through cell divisions? Do they influence subsequent gametogenesis, the competency for fertilization, and/or embryogenesis? And what of the DDR and higher-order chromatin organization? Apart from the sex chromosomes in MSCI, are near-patternless organization schemes observed at other sites and/or types of DDR signaling? Is this organization scheme some consequence, at least in part, of the prolonged loop extrusion processivity of meiotic prophase I? How is the phase separation of MSCI related to prolonged loop extrusion? What is the functional significance of the X chromosome's near-patternless organization scheme? I am eager to generate hypotheses to test these (and more) questions.

Conclusions

I am proud to write that our three studies, with their similarities and differences, evoke so many questions. They have also contributed new methods and new concepts to the fields of germline biology and chromatin biology. I hope that other researchers will adapt this information, including the quantitative comparisons genomic A/B compartment strengths; as well, I hope researchers will draw on the work of Wang & Wang et al. to analyze compartmentalization on the sub-chromosomal scale, correlating readouts with transcription. On a related note, Patel & Kang et al. have set a new standard for the specificity of germ cell isolation from male mammalian meiotic prophase I, and I hope others adopt their approach; and although only briefly touched on in this chapter, their analyses of chromatin interaction probabilities—especially via power-law scaling and related calculations—offer important, fascinating insights into the lengths, densities, and interactions of chromatin loop arrays.

Of course, our stories have their differences. Like the characters in *Rashomon*, our words, experiences, and interpretations may vary, but they nevertheless inform and expand our understanding of something fundamental: We see the outlines of mechanisms that drive chromatin looping, we recognize the power of the DDR to reorganize whole chromosomes, and we can begin to conceive of new dynamics for chromatin organization. I can't wait to do more research. I am deeply curious and passionate about all of this. If you have read this far, then I suspect I am not alone. Thank you.

Bibliography

1. Alavattam, K.G. *et al.* Elucidation of the Fanconi Anemia Protein Network in Meiosis and Its Function in the Regulation of Histone Modifications. *Cell Rep* **17**, 1141-1157 (2016).
2. Alavattam, K.G. *et al.* Attenuated chromatin compartmentalization in meiosis and its maturation in sperm development. *Nat Struct Mol Biol* **26**, 175-184 (2019).
3. Hasegawa, K. *et al.* SCML2 establishes the male germline epigenome through regulation of histone H2A ubiquitination. *Dev Cell* **32**, 574-588 (2015).
4. Lesch, B.J. & Page, D.C. Poised chromatin in the mammalian germ line. *Development* **141**, 3619-3626 (2014).
5. Lesch, B.J., Silber, S.J., McCarrey, J.R. & Page, D.C. Parallel evolution of male germline epigenetic poising and somatic development in animals. *Nat Genet* **48**, 888-894 (2016).
6. Soumillon, M. *et al.* Cellular source and mechanisms of high transcriptome complexity in the mammalian testis. *Cell Rep* **3**, 2179-2190 (2013).
7. Gill, M.E., Erkek, S. & Peters, A.H. Parental epigenetic control of embryogenesis: a balance between inheritance and reprogramming? *Curr Opin Cell Biol* **24**, 387-396 (2012).
8. Kimmins, S. & Sassone-Corsi, P. Chromatin remodelling and epigenetic features of germ cells. *Nature* **434**, 583-589 (2005).
9. Kota, S.K. & Feil, R. Epigenetic transitions in germ cell development and meiosis. *Dev Cell* **19**, 675-686 (2010).
10. Saitou, M., Kagiwada, S. & Kurimoto, K. Epigenetic reprogramming in mouse pre-implantation development and primordial germ cells. *Development* **139**, 15-31 (2012).
11. Sasaki, H. & Matsui, Y. Epigenetic events in mammalian germ-cell development: reprogramming and beyond. *Nat Rev Genet* **9**, 129-140 (2008).
12. Denomme, M.M. *et al.* Inheritance of epigenetic dysregulation from male factor infertility has a direct impact on reproductive potential. *Fertil Steril* **110**, 419-428 e411 (2018).

13. Du, Z. *et al.* Allelic reprogramming of 3D chromatin architecture during early mammalian development. *Nature* **547**, 232-235 (2017).
14. Hammoud, S.S. *et al.* Distinctive chromatin in human sperm packages genes for embryo development. *Nature* **460**, 473-478 (2009).
15. Holliday, R. The biological significance of meiosis. *Symp Soc Exp Biol* **38**, 381-394 (1984).
16. Ke, Y. *et al.* 3D Chromatin Structures of Mature Gametes and Structural Reprogramming during Mammalian Embryogenesis. *Cell* **170**, 367-381 e320 (2017).
17. Schagdarsurengin, U. & Steger, K. Epigenetics in male reproduction: effect of paternal diet on sperm quality and offspring health. *Nat Rev Urol* **13**, 584-595 (2016).
18. Siklenka, K. *et al.* Disruption of histone methylation in developing sperm impairs offspring health transgenerationally. *Science* **350**, aab2006 (2015).
19. Patel, L. *et al.* Dynamic reorganization of the genome shapes the recombination landscape in meiotic prophase. *Nat Struct Mol Biol* **26**, 164-174 (2019).
20. Wang, Y. *et al.* Reprogramming of Meiotic Chromatin Architecture during Spermatogenesis. *Mol Cell* **73**, 547-561 e546 (2019).
21. Burton, A. & Torres-Padilla, M.E. Chromatin dynamics in the regulation of cell fate allocation during early embryogenesis. *Nat Rev Mol Cell Biol* **15**, 723-734 (2014).
22. Jirtle, R.L. & Skinner, M.K. Environmental epigenomics and disease susceptibility. *Nat Rev Genet* **8**, 253-262 (2007).
23. Murrell, A., Rakyan, V.K. & Beck, S. From genome to epigenome. *Hum Mol Genet* **14 Spec No 1**, R3-R10 (2005).
24. Skinner, M.K., Anway, M.D., Savenkova, M.I., Gore, A.C. & Crews, D. Transgenerational epigenetic programming of the brain transcriptome and anxiety behavior. *PLoS One* **3**, e3745 (2008).
25. Skinner, M.K. Metabolic disorders: Fathers' nutritional legacy. *Nature* **467**, 922-923 (2010).

26. Reinberg, D. & Vales, L.D. Chromatin domains rich in inheritance. *Science* **361**, 33-34 (2018).

27. Perez, M.F. & Lehner, B. Intergenerational and transgenerational epigenetic inheritance in animals. *Nat Cell Biol* **21**, 143-151 (2019).

28. Heard, E. & Martienssen, R.A. Transgenerational epigenetic inheritance: myths and mechanisms. *Cell* **157**, 95-109 (2014).

29. Klukovich, R. *et al.* Environmental Toxicant Induced Epigenetic Transgenerational Inheritance of Prostate Pathology and Stromal-Epithelial Cell Epigenome and Transcriptome Alterations: Ancestral Origins of Prostate Disease. *Sci Rep* **9**, 2209 (2019).

30. Al-Sady, B., Madhani, H.D. & Narlikar, G.J. Division of labor between the chromodomains of HP1 and Suv39 methylase enables coordination of heterochromatin spread. *Mol Cell* **51**, 80-91 (2013).

31. Allis, C.D. & Jenuwein, T. The molecular hallmarks of epigenetic control. *Nat Rev Genet* **17**, 487-500 (2016).

32. Allshire, R.C. & Madhani, H.D. Ten principles of heterochromatin formation and function. *Nat Rev Mol Cell Biol* **19**, 229-244 (2018).

33. Coleman, R.T. & Struhl, G. Causal role for inheritance of H3K27me3 in maintaining the OFF state of a Drosophila HOX gene. *Science* **356**(2017).

34. Gaydos, L.J., Wang, W. & Strome, S. Gene repression. H3K27me and PRC2 transmit a memory of repression across generations and during development. *Science* **345**, 1515-1518 (2014).

35. Laprell, F., Finkl, K. & Muller, J. Propagation of Polycomb-repressed chromatin requires sequence-specific recruitment to DNA. *Science* **356**, 85-88 (2017).

36. Margueron, R. *et al.* Role of the polycomb protein EED in the propagation of repressive histone marks. *Nature* **461**, 762-767 (2009).

37. Muller, M.M., Fierz, B., Bittova, L., Liszczak, G. & Muir, T.W. A two-state activation mechanism controls the histone methyltransferase Suv39h1. *Nat Chem Biol* **12**, 188-193 (2016).

38. Trojer, P. & Reinberg, D. Beyond histone methyl-lysine binding: how malignant brain tumor (MBT) protein L3MBTL1 impacts chromatin structure. *Cell Cycle* **7**, 578-585 (2008).

39. Yang, H. *et al.* Distinct phases of Polycomb silencing to hold epigenetic memory of cold in Arabidopsis. *Science* **357**, 1142-1145 (2017).

40. Schultz, R.M. The molecular foundations of the maternal to zygotic transition in the preimplantation embryo. *Hum Reprod Update* **8**, 323-331 (2002).

41. Tadros, W. & Lipshitz, H.D. The maternal-to-zygotic transition: a play in two acts. *Development* **136**, 3033-3042 (2009).

42. Eckersley-Maslin, M.A., Alda-Catalinas, C. & Reik, W. Dynamics of the epigenetic landscape during the maternal-to-zygotic transition. *Nat Rev Mol Cell Biol* **19**, 436-450 (2018).

43. Xu, Q. & Xie, W. Epigenome in Early Mammalian Development: Inheritance, Reprogramming and Establishment. *Trends Cell Biol* **28**, 237-253 (2018).

44. Puschendorf, M. *et al.* PRC1 and Suv39h specify parental asymmetry at constitutive heterochromatin in early mouse embryos. *Nat Genet* **40**, 411-420 (2008).

45. Inoue, A., Jiang, L., Lu, F. & Zhang, Y. Genomic imprinting of Xist by maternal H3K27me3. *Genes Dev* **31**, 1927-1932 (2017).

46. Inoue, A., Jiang, L., Lu, F., Suzuki, T. & Zhang, Y. Maternal H3K27me3 controls DNA methylation-independent imprinting. *Nature* **547**, 419-424 (2017).

47. Kurotaki, Y.K. *et al.* Impaired active DNA demethylation in zygotes generated by round spermatid injection. *Hum Reprod* **30**, 1178-1187 (2015).

48. Ohta, H., Sakaide, Y. & Wakayama, T. Functional analysis of male mouse haploid germ cells of various differentiation stages: early and late round spermatids are functionally equivalent in producing progeny. *Biol Reprod* **80**, 511-517 (2009).

49. Lesch, B.J. *et al.* Intergenerational epigenetic inheritance of cancer susceptibility in mammals. *Elife* **8**(2019).

50. Ohinata, Y. *et al.* Blimp1 is a critical determinant of the germ cell lineage in mice. *Nature* **436**, 207-213 (2005).

51. Ueno, H., Turnbull, B.B. & Weissman, I.L. Two-step oligoclonal development of male germ cells. *Proc Natl Acad Sci U S A* **106**, 175-180 (2009).

52. Leitch, H.G., Tang, W.W. & Surani, M.A. Primordial germ-cell development and epigenetic reprogramming in mammals. *Curr Top Dev Biol* **104**, 149-187 (2013).

53. Kumar, D.L. & DeFalco, T. Of Mice and Men: In Vivo and In Vitro Studies of Primordial Germ Cell Specification. *Semin Reprod Med* **35**, 139-146 (2017).

54. Gray, S. & Cohen, P.E. Control of Meiotic Crossovers: From Double-Strand Break Formation to Designation. *Annu Rev Genet* **50**, 175-210 (2016).

55. Handel, M.A. & Schimenti, J.C. Genetics of mammalian meiosis: regulation, dynamics and impact on fertility. *Nat Rev Genet* **11**, 124-136 (2010).

56. Hunter, N. Meiotic Recombination: The Essence of Heredity. *Cold Spring Harb Perspect Biol* **7**(2015).

57. Cole, F. *et al.* Homeostatic control of recombination is implemented progressively in mouse meiosis. *Nat Cell Biol* **14**, 424-430 (2012).

58. Barchi, M. *et al.* Surveillance of different recombination defects in mouse spermatocytes yields distinct responses despite elimination at an identical developmental stage. *Mol Cell Biol* **25**, 7203-7215 (2005).

59. Subramanian, V.V. & Hochwagen, A. The meiotic checkpoint network: step-by-step through meiotic prophase. *Cold Spring Harb Perspect Biol* **6**, a016675 (2014).

60. Homolka, D., Ivanek, R., Capkova, J., Jansa, P. & Forejt, J. Chromosomal rearrangement interferes with meiotic X chromosome inactivation. *Genome Res* **17**, 1431-1437 (2007).

61. Odorisio, T., Rodriguez, T.A., Evans, E.P., Clarke, A.R. & Burgoyne, P.S. The meiotic checkpoint monitoring synapsis eliminates spermatocytes via p53-independent apoptosis. *Nat Genet* **18**, 257-261 (1998).

62. Fernandez-Capetillo, O. *et al.* H2AX is required for chromatin remodeling and inactivation of sex chromosomes in male mouse meiosis. *Dev Cell* **4**, 497-508 (2003).

63. Ichijima, Y. *et al.* MDC1 directs chromosome-wide silencing of the sex chromosomes in male germ cells. *Genes Dev* **25**, 959-971 (2011).

64. Ichijima, Y., Sin, H.S. & Namekawa, S.H. Sex chromosome inactivation in germ cells: emerging roles of DNA damage response pathways. *Cell Mol Life Sci* **69**, 2559-2572 (2012).

65. Turner, J.M. Meiotic sex chromosome inactivation. *Development* **134**, 1823-1831 (2007).

66. Yan, W. & McCarrey, J.R. Sex chromosome inactivation in the male. *Epigenetics* **4**, 452-456 (2009).

67. Greaves, I.K., Rangasamy, D., Devoy, M., Marshall Graves, J.A. & Tremethick, D.J. The X and Y chromosomes assemble into H2A.Z-containing [corrected] facultative heterochromatin [corrected] following meiosis. *Mol Cell Biol* **26**, 5394-5405 (2006).

68. Kato, Y. *et al.* FANCB is essential in the male germline and regulates H3K9 methylation on the sex chromosomes during meiosis. *Hum Mol Genet* **24**, 5234-5249 (2015).

69. Namekawa, S.H. *et al.* Postmeiotic sex chromatin in the male germline of mice. *Curr Biol* **16**, 660-667 (2006).

70. Namekawa, S.H., VandeBerg, J.L., McCarrey, J.R. & Lee, J.T. Sex chromosome silencing in the marsupial male germ line. *Proc Natl Acad Sci U S A* **104**, 9730-9735 (2007).

71. Royo, H. *et al.* ATR acts stage specifically to regulate multiple aspects of mammalian meiotic silencing. *Genes Dev* **27**, 1484-1494 (2013).

72. Sin, H.S. *et al.* RNF8 regulates active epigenetic modifications and escape gene activation from inactive sex chromosomes in post-meiotic spermatids. *Genes Dev* **26**, 2737-2748 (2012).

73. Turner, J.M. *et al.* BRCA1, histone H2AX phosphorylation, and male meiotic sex chromosome inactivation. *Curr Biol* **14**, 2135-2142 (2004).

74. Turner, J.M., Mahadevaiah, S.K., Ellis, P.J., Mitchell, M.J. & Burgoyne, P.S. Pachytene asynapsis drives meiotic sex chromosome inactivation and leads to substantial postmeiotic repression in spermatids. *Dev Cell* **10**, 521-529 (2006).

75. van der Heijden, G.W. *et al.* Chromosome-wide nucleosome replacement and H3.3 incorporation during mammalian meiotic sex chromosome inactivation. *Nat Genet* **39**, 251-258 (2007).

76. Broering, T.J. *et al.* BRCA1 establishes DNA damage signaling and pericentric heterochromatin of the X chromosome in male meiosis. *J Cell Biol* **205**, 663-675 (2014).

77. Mahadevaiah, S.K. *et al.* Extensive meiotic asynapsis in mice antagonises meiotic silencing of unsynapsed chromatin and consequently disrupts meiotic sex chromosome inactivation. *J Cell Biol* **182**, 263-276 (2008).

78. Baarends, W.M. *et al.* Silencing of unpaired chromatin and histone H2A ubiquitination in mammalian meiosis. *Mol Cell Biol* **25**, 1041-1053 (2005).

79. Burgoyne, P.S., Mahadevaiah, S.K. & Turner, J.M. The consequences of asynapsis for mammalian meiosis. *Nat Rev Genet* **10**, 207-216 (2009).

80. Schimenti, J. Synapsis or silence. *Nat Genet* **37**, 11-13 (2005).

81. Turner, J.M. *et al.* Silencing of unsynapsed meiotic chromosomes in the mouse. *Nat Genet* **37**, 41-47 (2005).

82. Maezawa, S., Yukawa, M., Alavattam, K.G., Barski, A. & Namekawa, S.H. Dynamic reorganization of open chromatin underlies diverse transcriptomes during spermatogenesis. *Nucleic Acids Res* **46**, 593-608 (2018).

83. Schultz, N., Hamra, F.K. & Garbers, D.L. A multitude of genes expressed solely in meiotic or postmeiotic spermatogenic cells offers a myriad of contraceptive targets. *Proc Natl Acad Sci U S A* **100**, 12201-12206 (2003).

84. Brykczynska, U. *et al.* Repressive and active histone methylation mark distinct promoters in human and mouse spermatozoa. *Nat Struct Mol Biol* **17**, 679-687 (2010).

85. Erkek, S. *et al.* Molecular determinants of nucleosome retention at CpG-rich sequences in mouse spermatozoa. *Nat Struct Mol Biol* **20**, 868-875 (2013).

86. Barral, S. *et al.* Histone Variant H2A.L.2 Guides Transition Protein-Dependent Protamine Assembly in Male Germ Cells. *Mol Cell* **66**, 89-101 e108 (2017).

87. Montellier, E. *et al.* Chromatin-to-nucleoprotamine transition is controlled by the histone H2B variant TH2B. *Genes Dev* **27**, 1680-1692 (2013).

88. Shinagawa, T. *et al.* Disruption of Th2a and Th2b genes causes defects in spermatogenesis. *Development* **142**, 1287-1292 (2015).

89. Ueda, J. *et al.* Testis-Specific Histone Variant H3t Gene Is Essential for Entry into Spermatogenesis. *Cell Rep* **18**, 593-600 (2017).

90. Maezawa, S. *et al.* Polycomb protein SCML2 facilitates H3K27me3 to establish bivalent domains in the male germline. *Proc Natl Acad Sci U S A* **115**, 4957-4962 (2018).

91. Ciccia, A. & Elledge, S.J. The DNA damage response: making it safe to play with knives. *Mol Cell* **40**, 179-204 (2010).

92. Polo, S.E. & Jackson, S.P. Dynamics of DNA damage response proteins at DNA breaks: a focus on protein modifications. *Genes Dev* **25**, 409-433 (2011).

93. Kee, Y. & D'Andrea, A.D. Expanded roles of the Fanconi anemia pathway in preserving genomic stability. *Genes Dev* **24**, 1680-1694 (2010).

94. Kottemann, M.C. & Smogorzewska, A. Fanconi anaemia and the repair of Watson and Crick DNA crosslinks. *Nature* **493**, 356-363 (2013).

95. Bluteau, D. *et al.* Biallelic inactivation of REV7 is associated with Fanconi anemia. *J Clin Invest* **126**, 3580-3584 (2016).

96. Park, J.Y. *et al.* Complementation of hypersensitivity to DNA interstrand crosslinking agents demonstrates that XRCC2 is a Fanconi anaemia gene. *J Med Genet* **53**, 672-680 (2016).

97. Sawyer, S.L. *et al.* Biallelic mutations in BRCA1 cause a new Fanconi anemia subtype. *Cancer Discov* **5**, 135-142 (2015).

98. Wang, A.T. *et al.* A Dominant Mutation in Human RAD51 Reveals Its Function in DNA Interstrand Crosslink Repair Independent of Homologous Recombination. *Mol Cell* **59**, 478-490 (2015).

99. Garcia-Higuera, I. *et al.* Interaction of the Fanconi anemia proteins and BRCA1 in a common pathway. *Mol Cell* **7**, 249-262 (2001).

100. Meetei, A.R. *et al.* A novel ubiquitin ligase is deficient in Fanconi anemia. *Nat Genet* **35**, 165-170 (2003).

101. Sims, A.E. *et al.* FANCI is a second monoubiquitinated member of the Fanconi anemia pathway. *Nat Struct Mol Biol* **14**, 564-567 (2007).

102. Smogorzewska, A. *et al.* Identification of the FANCI protein, a monoubiquitinated FANCD2 paralog required for DNA repair. *Cell* **129**, 289-301 (2007).

103. Howlett, N.G. *et al.* Biallelic inactivation of BRCA2 in Fanconi anemia. *Science* **297**, 606-609 (2002).

104. Park, J.Y., Zhang, F. & Andreassen, P.R. PALB2: the hub of a network of tumor suppressors involved in DNA damage responses. *Biochim Biophys Acta* **1846**, 263-275 (2014).

105. Kim, Y. *et al.* Mutations of the SLX4 gene in Fanconi anemia. *Nat Genet* **43**, 142-146 (2011).

106. Stoepker, C. *et al.* SLX4, a coordinator of structure-specific endonucleases, is mutated in a new Fanconi anemia subtype. *Nat Genet* **43**, 138-141 (2011).

107. Bakker, S.T. *et al.* Fancm-deficient mice reveal unique features of Fanconi anemia complementation group M. *Hum Mol Genet* **18**, 3484-3495 (2009).

108. Taniguchi, T. *et al.* S-phase-specific interaction of the Fanconi anemia protein, FANCD2, with BRCA1 and RAD51. *Blood* **100**, 2414-2420 (2002).

109. An, J.Y. *et al.* UBR2 of the N-end rule pathway is required for chromosome stability via histone ubiquitylation in spermatocytes and somatic cells. *PLoS One* **7**, e37414 (2012).

110. Timmers, C. *et al.* Positional cloning of a novel Fanconi anemia gene, FANCD2. *Mol Cell* **7**, 241-248 (2001).

111. Houghtaling, S. *et al.* Epithelial cancer in Fanconi anemia complementation group D2 (Fancd2) knockout mice. *Genes Dev* **17**, 2021-2035 (2003).

112. Chen, J. *et al.* Stable interaction between the products of the BRCA1 and BRCA2 tumor suppressor genes in mitotic and meiotic cells. *Mol Cell* **2**, 317-328 (1998).

113. Holloway, J.K. *et al.* Mammalian BTBD12 (SLX4) protects against genomic instability during mammalian spermatogenesis. *PLoS Genet* **7**, e1002094 (2011).

114. Moynahan, M.E., Pierce, A.J. & Jasin, M. BRCA2 is required for homology-directed repair of chromosomal breaks. *Mol Cell* **7**, 263-272 (2001).

115. Park, J.Y. *et al.* Breast cancer-associated missense mutants of the PALB2 WD40 domain, which directly binds RAD51C, RAD51 and BRCA2, disrupt DNA repair. *Oncogene* **33**, 4803-4812 (2014).

116. Wang, X., Andreassen, P.R. & D'Andrea, A.D. Functional interaction of monoubiquitinated FANCD2 and BRCA2/FANCD1 in chromatin. *Mol Cell Biol* **24**, 5850-5862 (2004).

117. Yamamoto, K.N. *et al.* Involvement of SLX4 in interstrand cross-link repair is regulated by the Fanconi anemia pathway. *Proc Natl Acad Sci U S A* **108**, 6492-6496 (2011).

118. Folias, A. *et al.* BRCA1 interacts directly with the Fanconi anemia protein FANCA. *Hum Mol Genet* **11**, 2591-2597 (2002).

119. Zhang, F., Fan, Q., Ren, K., Auerbach, A.D. & Andreassen, P.R. FANCJ/BRIP1 recruitment and regulation of FANCD2 in DNA damage responses. *Chromosoma* **119**, 637-649 (2010).

120. Vandenberg, C.J. *et al.* BRCA1-independent ubiquitination of FANCD2. *Mol Cell* **12**, 247-254 (2003).

121. Gallardo, T., Shirley, L., John, G.B. & Castrillon, D.H. Generation of a germ cell-specific mouse transgenic Cre line, Vasa-Cre. *Genesis* **45**, 413-417 (2007).

122. Zhang, F., Fan, Q., Ren, K. & Andreassen, P.R. PALB2 functionally connects the breast cancer susceptibility proteins BRCA1 and BRCA2. *Mol Cancer Res* **7**, 1110-1118 (2009).

123. Zhang, F. *et al.* PALB2 links BRCA1 and BRCA2 in the DNA-damage response. *Curr Biol* **19**, 524-529 (2009).

124. Lachaud, C. *et al.* Distinct functional roles for the two SLX4 ubiquitin-binding UBZ domains mutated in Fanconi anemia. *J Cell Sci* **127**, 2811-2817 (2014).

125. Xu, X., Aprelikova, O., Moens, P., Deng, C.X. & Furth, P.A. Impaired meiotic DNA-damage repair and lack of crossing-over during spermatogenesis in BRCA1 full-length isoform deficient mice. *Development* **130**, 2001-2012 (2003).

126. Goldberg, M. *et al.* MDC1 is required for the intra-S-phase DNA damage checkpoint. *Nature* **421**, 952-956 (2003).

127. Lou, Z., Minter-Dykhouse, K., Wu, X. & Chen, J. MDC1 is coupled to activated CHK2 in mammalian DNA damage response pathways. *Nature* **421**, 957-961 (2003).

128. Stewart, G.S., Wang, B., Bignell, C.R., Taylor, A.M. & Elledge, S.J. MDC1 is a mediator of the mammalian DNA damage checkpoint. *Nature* **421**, 961-966 (2003).

129. Huen, M.S. *et al.* RNF8 transduces the DNA-damage signal via histone ubiquitylation and checkpoint protein assembly. *Cell* **131**, 901-914 (2007).

130. Kolas, N.K. *et al.* Orchestration of the DNA-damage response by the RNF8 ubiquitin ligase. *Science* **318**, 1637-1640 (2007).

131. Mailand, N. *et al.* RNF8 ubiquitylates histones at DNA double-strand breaks and promotes assembly of repair proteins. *Cell* **131**, 887-900 (2007).

132. Zhang, F., Bick, G., Park, J.Y. & Andreassen, P.R. MDC1 and RNF8 function in a pathway that directs BRCA1-dependent localization of PALB2 required for homologous recombination. *J Cell Sci* **125**, 6049-6057 (2012).

133. Bick, G., Zhang, F., Meetei, A.R. & Andreassen, P.R. Coordination of the recruitment of the FANCD2 and PALB2 Fanconi anemia proteins by an ubiquitin signaling network. *Chromosoma* **126**, 417-430 (2017).

134. Yan, Z. *et al.* A ubiquitin-binding protein, FAAP20, links RNF8-mediated ubiquitination to the Fanconi anemia DNA repair network. *Mol Cell* **47**, 61-75 (2012).

135. Lu, L.Y., Xiong, Y., Kuang, H., Korakavi, G. & Yu, X. Regulation of the DNA damage response on male meiotic sex chromosomes. *Nat Commun* **4**, 2105 (2013).

136. Carofiglio, F. *et al.* SPO11-independent DNA repair foci and their role in meiotic silencing. *PLoS Genet* **9**, e1003538 (2013).

137. Inagaki, A., Schoenmakers, S. & Baarends, W.M. DNA double strand break repair, chromosome synapsis and transcriptional silencing in meiosis. *Epigenetics* **5**, 255-266 (2010).

138. Baudat, F., Manova, K., Yuen, J.P., Jasin, M. & Keeney, S. Chromosome synapsis defects and sexually dimorphic meiotic progression in mice lacking Spo11. *Mol Cell* **6**, 989-998 (2000).

139. Romanienko, P.J. & Camerini-Otero, R.D. The mouse Spo11 gene is required for meiotic chromosome synapsis. *Mol Cell* **6**, 975-987 (2000).

140. Bellani, M.A., Romanienko, P.J., Cairatti, D.A. & Camerini-Otero, R.D. SPO11 is required for sex-body formation, and Spo11 heterozygosity rescues the prophase arrest of Atm-/- spermatocytes. *J Cell Sci* **118**, 3233-3245 (2005).

141. Khalil, A.M., Boyar, F.Z. & Driscoll, D.J. Dynamic histone modifications mark sex chromosome inactivation and reactivation during mammalian spermatogenesis. *Proc Natl Acad Sci U S A* **101**, 16583-16587 (2004).

142. Hall, L.L. *et al.* An ectopic human XIST gene can induce chromosome inactivation in postdifferentiation human HT-1080 cells. *Proc Natl Acad Sci U S A* **99**, 8677-8682 (2002).

143. Namekawa, S.H., Payer, B., Huynh, K.D., Jaenisch, R. & Lee, J.T. Two-step imprinted X inactivation: repeat versus genic silencing in the mouse. *Mol Cell Biol* **30**, 3187-3205 (2010).

144. Yata, K. *et al.* Plk1 and CK2 act in concert to regulate Rad51 during DNA double strand break repair. *Mol Cell* **45**, 371-383 (2012).

145. Medhurst, A.L. *et al.* Evidence for subcomplexes in the Fanconi anemia pathway. *Blood* **108**, 2072-2080 (2006).

146. Meetei, A.R. *et al.* A human ortholog of archaeal DNA repair protein Hef is defective in Fanconi anemia complementation group M. *Nat Genet* **37**, 958-963 (2005).

147. Crismani, W. *et al.* FANCM limits meiotic crossovers. *Science* **336**, 1588-1590 (2012).

148. Lorenz, A. *et al.* The fission yeast FANCM ortholog directs non-crossover recombination during meiosis. *Science* **336**, 1585-1588 (2012).

149. Singh, T.R. *et al.* Impaired FANCD2 monoubiquitination and hypersensitivity to camptothecin uniquely characterize Fanconi anemia complementation group M. *Blood* **114**, 174-180 (2009).

150. Raschle, M. *et al.* DNA repair. Proteomics reveals dynamic assembly of repair complexes during bypass of DNA cross-links. *Science* **348**, 1253671 (2015).

151. Whitney, M.A. *et al.* Germ cell defects and hematopoietic hypersensitivity to gamma-interferon in mice with a targeted disruption of the Fanconi anemia C gene. *Blood* **88**, 49-58 (1996).

152. Wong, J.C. *et al.* Targeted disruption of exons 1 to 6 of the Fanconi Anemia group A gene leads to growth retardation, strain-specific microphthalmia, meiotic defects and primordial germ cell hypoplasia. *Hum Mol Genet* **12**, 2063-2076 (2003).

153. Sato, K. *et al.* Histone chaperone activity of Fanconi anemia proteins, FANCD2 and FANCI, is required for DNA crosslink repair. *EMBO J* **31**, 3524-3536 (2012).

154. Chen, M. *et al.* Inactivation of Fac in mice produces inducible chromosomal instability and reduced fertility reminiscent of Fanconi anaemia. *Nat Genet* **12**, 448-451 (1996).

155. Cheng, N.C. *et al.* Mice with a targeted disruption of the Fanconi anemia homolog Fanca. *Hum Mol Genet* **9**, 1805-1811 (2000).

156. Lou, Z. *et al.* MDC1 maintains genomic stability by participating in the amplification of ATM-dependent DNA damage signals. *Mol Cell* **21**, 187-200 (2006).

157. Minter-Dykhouse, K., Ward, I., Huen, M.S., Chen, J. & Lou, Z. Distinct versus overlapping functions of MDC1 and 53BP1 in DNA damage response and tumorigenesis. *J Cell Biol* **181**, 727-735 (2008).

158. Xu, X. *et al.* Conditional mutation of Brca1 in mammary epithelial cells results in blunted ductal morphogenesis and tumour formation. *Nat Genet* **22**, 37-43 (1999).

159. Peters, A.H., Plug, A.W., van Vugt, M.J. & de Boer, P. A drying-down technique for the spreading of mammalian meiocytes from the male and female germline. *Chromosome Res* **5**, 66-68 (1997).

160. Yamane, K., Wu, X. & Chen, J. A DNA damage-regulated BRCT-containing protein, TopBP1, is required for cell survival. *Mol Cell Biol* **22**, 555-566 (2002).

161. Namekawa, S.H. & Lee, J.T. Detection of nascent RNA, single-copy DNA and protein localization by immunoFISH in mouse germ cells and preimplantation embryos. *Nat Protoc* **6**, 270-284 (2011).

162. Namekawa, S.H. Slide preparation method to preserve three-dimensional chromatin architecture of testicular germ cells. *J Vis Exp*, e50819 (2014).

163. Schneider, C.A., Rasband, W.S. & Eliceiri, K.W. NIH Image to ImageJ: 25 years of image analysis. *Nat Methods* **9**, 671-675 (2012).

164. Schindelin, J. *et al.* Fiji: an open-source platform for biological-image analysis. *Nat Methods* **9**, 676-682 (2012).

165. Li, J., Du, W., Maynard, S., Andreassen, P.R. & Pang, Q. Oxidative stress-specific interaction between FANCD2 and FOXO3a. *Blood* **115**, 1545-1548 (2010).

166. Battulin, N. *et al.* Comparison of the three-dimensional organization of sperm and fibroblast genomes using the Hi-C approach. *Genome Biol* **16**, 77 (2015).

167. Jung, Y.H. *et al.* Chromatin States in Mouse Sperm Correlate with Embryonic and Adult Regulatory Landscapes. *Cell Rep* **18**, 1366-1382 (2017).

168. Selvaraj, S., J, R.D., Bansal, V. & Ren, B. Whole-genome haplotype reconstruction using proximity-ligation and shotgun sequencing. *Nat Biotechnol* **31**, 1111-1118 (2013).

169. Dixon, J.R. *et al.* Topological domains in mammalian genomes identified by analysis of chromatin interactions. *Nature* **485**, 376-380 (2012).

170. Nora, E.P. *et al.* Spatial partitioning of the regulatory landscape of the X-inactivation centre. *Nature* **485**, 381-385 (2012).

171. Naumova, N. *et al.* Organization of the mitotic chromosome. *Science* **342**, 948-953 (2013).

172. Fudenberg, G. & Mirny, L.A. Higher-order chromatin structure: bridging physics and biology. *Curr Opin Genet Dev* **22**, 115-124 (2012).

173. Lieberman-Aiden, E. *et al.* Comprehensive mapping of long-range interactions reveals folding principles of the human genome. *Science* **326**, 289-293 (2009).

174. Gibcus, J.H. *et al.* A pathway for mitotic chromosome formation. *Science* **359**(2018).

175. Imakaev, M. *et al.* Iterative correction of Hi-C data reveals hallmarks of chromosome organization. *Nat Methods* **9**, 999-1003 (2012).

176. Lajoie, B.R., Dekker, J. & Kaplan, N. The Hitchhiker's guide to Hi-C analysis: practical guidelines. *Methods* **72**, 65-75 (2015).

177. Flyamer, I.M. *et al.* Single-nucleus Hi-C reveals unique chromatin reorganization at oocyte-to-zygote transition. *Nature* **544**, 110-114 (2017).

178. Nagano, T. *et al.* Cell-cycle dynamics of chromosomal organization at single-cell resolution. *Nature* **547**, 61-67 (2017).

179. Zickler, D. & Kleckner, N. Meiotic chromosomes: integrating structure and function. *Annu Rev Genet* **33**, 603-754 (1999).

180. Scherthan, H. A bouquet makes ends meet. *Nat Rev Mol Cell Biol* **2**, 621-627 (2001).

181. Scherthan, H., Schofisch, K., Dell, T. & Illner, D. Contrasting behavior of heterochromatic and euchromatic chromosome portions and pericentric genome separation in pre-bouquet spermatocytes of hybrid mice. *Chromosoma* **123**, 609-624 (2014).

182. Dixon, J.R. *et al.* Chromatin architecture reorganization during stem cell differentiation. *Nature* **518**, 331-336 (2015).

183. Javierre, B.M. *et al.* Lineage-Specific Genome Architecture Links Enhancers and Non-coding Disease Variants to Target Gene Promoters. *Cell* **167**, 1369-1384 e1319 (2016).

184. Le Dily, F. *et al.* Distinct structural transitions of chromatin topological domains correlate with coordinated hormone-induced gene regulation. *Genes Dev* **28**, 2151-2162 (2014).

185. Ramirez, F. *et al.* High-resolution TADs reveal DNA sequences underlying genome organization in flies. *Nat Commun* **9**, 189 (2018).

186. Wolff, J. *et al.* Galaxy HiCExplorer: a web server for reproducible Hi-C data analysis, quality control and visualization. *Nucleic Acids Res* **46**, W11-W16 (2018).

187. Rao, S.S. *et al.* A 3D map of the human genome at kilobase resolution reveals principles of chromatin looping. *Cell* **159**, 1665-1680 (2014).

188. Cao, Y. *et al.* Accurate loop calling for 3D genomic data with cLoops. *bioRxiv*, 465849 (2018).

189. Deng, X. *et al.* Bipartite structure of the inactive mouse X chromosome. *Genome Biol* **16**, 152 (2015).

190. Giorgetti, L. *et al.* Structural organization of the inactive X chromosome in the mouse. *Nature* **535**, 575-579 (2016).

191. Minajigi, A. *et al.* Chromosomes. A comprehensive Xist interactome reveals cohesin repulsion and an RNA-directed chromosome conformation. *Science* **349**(2015).

192. Wang, C.Y., Jegu, T., Chu, H.P., Oh, H.J. & Lee, J.T. SMCHD1 Merges Chromosome Compartments and Assists Formation of Super-Structures on the Inactive X. *Cell* **174**, 406-421 e425 (2018).

193. Liang, Z. *et al.* Chromosomes Progress to Metaphase in Multiple Discrete Steps via Global Compaction/Expansion Cycles. *Cell* **161**, 1124-1137 (2015).

194. Dekker, J., Rippe, K., Dekker, M. & Kleckner, N. Capturing chromosome conformation. *Science* **295**, 1306-1311 (2002).

195. Muller, H. *et al.* Characterizing meiotic chromosomes' structure and pairing using a designer sequence optimized for Hi-C. *Mol Syst Biol* **14**, e8293 (2018).

196. Schalbetter, S.A., Fudenberg, G., Baxter, J., Pollard, K.S. & Neale, M.J. Principles of Meiotic Chromosome Assembly. *bioRxiv*, 442038 (2019).

197. Duan, Z. *et al.* A three-dimensional model of the yeast genome. *Nature* **465**, 363-367 (2010).

198. Mizuguchi, T. *et al.* Cohesin-dependent globules and heterochromatin shape 3D genome architecture in S. pombe. *Nature* **516**, 432-435 (2014).

199. Tjong, H., Gong, K., Chen, L. & Alber, F. Physical tethering and volume exclusion determine higher-order genome organization in budding yeast. *Genome Res* **22**, 1295-1305 (2012).

200. Busslinger, G.A. *et al.* Cohesin is positioned in mammalian genomes by transcription, CTCF and Wapl. *Nature* **544**, 503-507 (2017).

201. Haarhuis, J.H.I. *et al.* The Cohesin Release Factor WAPL Restricts Chromatin Loop Extension. *Cell* **169**, 693-707 e614 (2017).

202. Rao, S.S.P. *et al.* Cohesin Loss Eliminates All Loop Domains. *Cell* **171**, 305-320 e324 (2017).

203. McNicoll, F., Stevense, M. & Jessberger, R. Cohesin in gametogenesis. *Curr Top Dev Biol* **102**, 1-34 (2013).

204. Loukinov, D.I. *et al.* BORIS, a novel male germ-line-specific protein associated with epigenetic reprogramming events, shares the same 11-zinc-finger domain with CTCF, the insulator protein involved in reading imprinting marks in the soma. *Proc Natl Acad Sci U S A* **99**, 6806-6811 (2002).

205. Banani, S.F., Lee, H.O., Hyman, A.A. & Rosen, M.K. Biomolecular condensates: organizers of cellular biochemistry. *Nat Rev Mol Cell Biol* **18**, 285-298 (2017).

206. Bergeron-Sandoval, L.P., Safaee, N. & Michnick, S.W. Mechanisms and Consequences of Macromolecular Phase Separation. *Cell* **165**, 1067-1079 (2016).

207. Larson, A.G. *et al.* Liquid droplet formation by HP1alpha suggests a role for phase separation in heterochromatin. *Nature* **547**, 236-240 (2017).

208. Strom, A.R. *et al.* Phase separation drives heterochromatin domain formation. *Nature* **547**, 241-245 (2017).

209. Hnisz, D., Shrinivas, K., Young, R.A., Chakraborty, A.K. & Sharp, P.A. A Phase Separation Model for Transcriptional Control. *Cell* **169**, 13-23 (2017).

210. Bellve, A.R. Purification, culture, and fractionation of spermatogenic cells. *Methods Enzymol* **225**, 84-113 (1993).

211. Belaghzal, H., Dekker, J. & Gibcus, J.H. Hi-C 2.0: An optimized Hi-C procedure for high-resolution genome-wide mapping of chromosome conformation. *Methods* **123**, 56-65 (2017).

212. Abdennur, N. & Mirny, L. Cooler: scalable storage for Hi-C data and other genomically-labeled arrays. *bioRxiv*, 557660 (2019).

213. Langmead, B. & Salzberg, S.L. Fast gapped-read alignment with Bowtie 2. *Nat Methods* **9**, 357-359 (2012).

214. Kaplan, N. & Dekker, J. High-throughput genome scaffolding from in vivo DNA interaction frequency. *Nat Biotechnol* **31**, 1143-1147 (2013).

215. Virkar, Y. & Clauset, A. Power-Law Distributions in Binned Empirical Data. *Annals of Applied Statistics* **8**, 89-119 (2014).

216. Oliphant, T.E. Python for scientific computing. *Computing in Science & Engineering* **9**, 10-20 (2007).

217. Crane, E. *et al.* Condensin-driven remodelling of X chromosome topology during dosage compensation. *Nature* **523**, 240-U299 (2015).

218. Zhang, Y. *et al.* Spatial Organization of the Mouse Genome and Its Role in Recurrent Chromosomal Translocations. *Cell* **148**, 908-921 (2012).

219. Ramirez, F. *et al.* High-Affinity Sites Form an Interaction Network to Facilitate Spreading of the MSL Complex across the X Chromosome in Drosophila. *Molecular Cell* **60**, 146-162 (2015).

220. Khan, A. & Mathelier, A. Intervene: a tool for intersection and visualization of multiple gene or genomic region sets. *Bmc Bioinformatics* **18**(2017).

221. Conway, J.R., Lex, A. & Gehlenborg, N. UpSetR: an R package for the visualization of intersecting sets and their properties. *Bioinformatics* **33**, 2938-2940 (2017).

222. Kobayashi, H. *et al.* Contribution of intragenic DNA methylation in mouse gametic DNA methylomes to establish oocyte-specific heritable marks. *PLoS Genet* **8**, e1002440 (2012).

223. Adams, S.R. *et al.* RNF8 and SCML2 cooperate to regulate ubiquitination and H3K27 acetylation for escape gene activation on the sex chromosomes. *PLoS Genet* **14**, e1007233 (2018).

224. Shen, Y. *et al.* A map of the cis-regulatory sequences in the mouse genome. *Nature* **488**, 116-120 (2012).

225. Dowen, J.M. *et al.* Control of cell identity genes occurs in insulated neighborhoods in mammalian chromosomes. *Cell* **159**, 374-387 (2014).

226. Dobin, A. *et al.* STAR: ultrafast universal RNA-seq aligner. *Bioinformatics* **29**, 15-21 (2013).

227. Langmead, B., Trapnell, C., Pop, M. & Salzberg, S.L. Ultrafast and memory-efficient alignment of short DNA sequences to the human genome. *Genome Biol* **10**, R25 (2009).

228. Zhang, Y. *et al.* Model-based analysis of ChIP-Seq (MACS). *Genome Biol* **9**, R137 (2008).

229. Kartashov, A.V. & Barski, A. BioWardrobe: an integrated platform for analysis of epigenomics and transcriptomics data. *Genome Biol* **16**, 158 (2015).

230. Kent, W.J. *et al.* The human genome browser at UCSC. *Genome Res* **12**, 996-1006 (2002).

231. Ramirez, F. *et al.* deepTools2: a next generation web server for deep-sequencing data analysis. *Nucleic Acids Res* **44**, W160-165 (2016).

232. Shen, L., Shao, N., Liu, X. & Nestler, E. ngs.plot: Quick mining and visualization of next-generation sequencing data by integrating genomic databases. *BMC Genomics* **15**, 284 (2014).

233. Quinlan, A.R. BEDTools: The Swiss-Army Tool for Genome Feature Analysis. *Curr Protoc Bioinformatics* **47**, 11 12 11-34 (2014).

234. Wickham, H. *Ggplot2*, pages cm (Springer Science+Business Media, LLC, New York, NY, 2016).

235. Feynman, R.P. *The character of physical law*, 173 p. (M.I.T. Press, Cambridge,, 1965).

236. Kurosawa, A. *et al.* Rashomon. 9 reels of 9 (ca. 7920 ft.) (s.n. RKO Radio Pictures, Japan; United States, 1952).

237. Davis, B., Anderson, R. & Walls, J. *Rashomon effects : Kurosawa, Rashomon and their legacies*, xviii, 178 pages (Routledge, Milton Park, Abingdon, Oxon ; New York, NY, 2015).

238. Hogarth, C.A. *et al.* Turning a spermatogenic wave into a tsunami: synchronizing murine spermatogenesis using WIN 18,446. *Biol Reprod* **88**, 40 (2013).

239. Hogarth, C.A. & Griswold, M.D. The key role of vitamin A in spermatogenesis. *J Clin Invest* **120**, 956-962 (2010).

240. Cole, F. *et al.* Mouse tetrad analysis provides insights into recombination mechanisms and hotspot evolutionary dynamics. *Nat Genet* **46**, 1072-1080 (2014).

241. Bryant, J.M., Meyer-Ficca, M.L., Dang, V.M., Berger, S.L. & Meyer, R.G. Separation of spermatogenic cell types using STA-PUT velocity sedimentation. *J Vis Exp* (2013).

242. Bryant, J.M. *et al.* Characterization of BRD4 during mammalian postmeiotic sperm development. *Mol Cell Biol* **35**, 1433-1448 (2015).

243. Hur, S.K. *et al.* Humanized H19/Igf2 locus reveals diverged imprinting mechanism between mouse and human and reflects Silver-Russell syndrome phenotypes. *Proc Natl Acad Sci U S A* **113**, 10938-10943 (2016).

244. Korhonen, H.M. *et al.* DICER Regulates the Formation and Maintenance of Cell-Cell Junctions in the Mouse Seminiferous Epithelium. *Biol Reprod* **93**, 139 (2015).

245. Liu, Y. *et al.* Fractionation of human spermatogenic cells using STA-PUT gravity sedimentation and their miRNA profiling. *Sci Rep* **5**, 8084 (2015).

246. Luense, L.J. *et al.* Comprehensive analysis of histone post-translational modifications in mouse and human male germ cells. *Epigenetics Chromatin* **9**, 24 (2016).

247. Gribnau, J., Hochedlinger, K., Hata, K., Li, E. & Jaenisch, R. Asynchronous replication timing of imprinted loci is independent of DNA methylation, but consistent with differential subnuclear localization. *Genes Dev* **17**, 759-773 (2003).

248. Sakashita, A. *et al.* XY oocytes of sex-reversed females with a Sry mutation deviate from the normal developmental process beyond the mitotic stagedagger. *Biol Reprod* **100**, 697-710 (2019).

249. Sexton, T. *et al.* Three-dimensional folding and functional organization principles of the Drosophila genome. *Cell* **148**, 458-472 (2012).

250. Alipour, E. & Marko, J.F. Self-organization of domain structures by DNA-loop-extruding enzymes. *Nucleic Acids Res* **40**, 11202-11212 (2012).

251. Fudenberg, G. *et al.* Formation of Chromosomal Domains by Loop Extrusion. *Cell Rep* **15**, 2038-2049 (2016).

252. Nasmyth, K. Disseminating the genome: joining, resolving, and separating sister chromatids during mitosis and meiosis. *Annu Rev Genet* **35**, 673-745 (2001).

253. Nuebler, J., Fudenberg, G., Imakaev, M., Abdennur, N. & Mirny, L.A. Chromatin organization by an interplay of loop extrusion and compartmental segregation. *Proc Natl Acad Sci U S A* **115**, E6697-E6706 (2018).

254. Sanborn, A.L. *et al.* Chromatin extrusion explains key features of loop and domain formation in wild-type and engineered genomes. *Proc Natl Acad Sci U S A* **112**, E6456-6465 (2015).

255. Guacci, V., Koshland, D. & Strunnikov, A. A direct link between sister chromatid cohesion and chromosome condensation revealed through the analysis of MCD1 in S. cerevisiae. *Cell* **91**, 47-57 (1997).

256. Michaelis, C., Ciosk, R. & Nasmyth, K. Cohesins: chromosomal proteins that prevent premature separation of sister chromatids. *Cell* **91**, 35-45 (1997).

257. Pauli, A. *et al.* Cell-type-specific TEV protease cleavage reveals cohesin functions in Drosophila neurons. *Dev Cell* **14**, 239-251 (2008).

258. Rollins, R.A., Morcillo, P. & Dorsett, D. Nipped-B, a Drosophila homologue of chromosomal adherins, participates in activation by remote enhancers in the cut and Ultrabithorax genes. *Genetics* **152**, 577-593 (1999).

259. Ganji, M. *et al.* Real-time imaging of DNA loop extrusion by condensin. *Science* **360**, 102-105 (2018).

260. Hansen, A.S., Pustova, I., Cattoglio, C., Tjian, R. & Darzacq, X. CTCF and cohesin regulate chromatin loop stability with distinct dynamics. *Elife* **6**(2017).

261. Nora, E.P. *et al.* Targeted Degradation of CTCF Decouples Local Insulation of Chromosome Domains from Genomic Compartmentalization. *Cell* **169**, 930-944 e922 (2017).

262. Rowley, M.J. & Corces, V.G. Organizational principles of 3D genome architecture. *Nat Rev Genet* **19**, 789-800 (2018).

263. Hou, C., Li, L., Qin, Z.S. & Corces, V.G. Gene density, transcription, and insulators contribute to the partition of the Drosophila genome into physical domains. *Mol Cell* **48**, 471-484 (2012).

264. Vietri Rudan, M. *et al.* Comparative Hi-C reveals that CTCF underlies evolution of chromosomal domain architecture. *Cell Rep* **10**, 1297-1309 (2015).

265. de Wit, E. *et al.* CTCF Binding Polarity Determines Chromatin Looping. *Mol Cell* **60**, 676-684 (2015).

266. Guo, Y. *et al.* CRISPR Inversion of CTCF Sites Alters Genome Topology and Enhancer/Promoter Function. *Cell* **162**, 900-910 (2015).

267. Phillips-Cremins, J.E. *et al.* Architectural protein subclasses shape 3D organization of genomes during lineage commitment. *Cell* **153**, 1281-1295 (2013).

268. Seitan, V.C. *et al.* Cohesin-based chromatin interactions enable regulated gene expression within preexisting architectural compartments. *Genome Res* **23**, 2066-2077 (2013).

269. Sofueva, S. *et al.* Cohesin-mediated interactions organize chromosomal domain architecture. *EMBO J* **32**, 3119-3129 (2013).

270. Zuin, J. *et al.* Cohesin and CTCF differentially affect chromatin architecture and gene expression in human cells. *Proc Natl Acad Sci U S A* **111**, 996-1001 (2014).

271. Flavahan, W.A. *et al.* Insulator dysfunction and oncogene activation in IDH mutant gliomas. *Nature* **529**, 110-114 (2016).

272. Narendra, V. *et al.* CTCF establishes discrete functional chromatin domains at the Hox clusters during differentiation. *Science* **347**, 1017-1021 (2015).

273. Schwarzer, W. *et al.* Two independent modes of chromatin organization revealed by cohesin removal. *Nature* **551**, 51-56 (2017).

274. Tedeschi, A. *et al.* Wapl is an essential regulator of chromatin structure and chromosome segregation. *Nature* **501**, 564-568 (2013).

275. Gassler, J. *et al.* A mechanism of cohesin-dependent loop extrusion organizes zygotic genome architecture. *EMBO J* **36**, 3600-3618 (2017).

276. Ellnati, E. *et al.* DNA damage response protein TOPBP1 regulates X chromosome silencing in the mammalian germ line. *Proc Natl Acad Sci U S A* **114**, 12536-12541 (2017).

277. Mahadevaiah, S.K. *et al.* Recombinational DNA double-strand breaks in mice precede synapsis. *Nat Genet* **27**, 271-276 (2001).

278. Widger, A. *et al.* ATR is a multifunctional regulator of male mouse meiosis. *Nat Commun* **9**, 2621 (2018).

279. Mitrea, D.M. & Kriwacki, R.W. Phase separation in biology; functional organization of a higher order. *Cell Commun Signal* **14**, 1 (2016).

280. Aymard, F. *et al.* Genome-wide mapping of long-range contacts unveils clustering of DNA double-strand breaks at damaged active genes. *Nat Struct Mol Biol* **24**, 353-361 (2017).

281. Aymard, F. *et al.* Transcriptionally active chromatin recruits homologous recombination at DNA double-strand breaks. *Nat Struct Mol Biol* **21**, 366-374 (2014).

282. Guenole, A. & Legube, G. A meeting at risk: Unrepaired DSBs go for broke. *Nucleus* **8**, 589-599 (2017).

283. Marnef, A., Cohen, S. & Legube, G. Transcription-Coupled DNA Double-Strand Break Repair: Active Genes Need Special Care. *J Mol Biol* **429**, 1277-1288 (2017).

284. Essers, J. *et al.* Dynamics of relative chromosome position during the cell cycle. *Mol Biol Cell* **16**, 769-775 (2005).

285. Thomson, I., Gilchrist, S., Bickmore, W.A. & Chubb, J.R. The radial positioning of chromatin is not inherited through mitosis but is established de novo in early G1. *Curr Biol* **14**, 166-172 (2004).

286. Walter, J., Schermelleh, L., Cremer, M., Tashiro, S. & Cremer, T. Chromosome order in HeLa cells changes during mitosis and early G1, but is stably maintained during subsequent interphase stages. *J Cell Biol* **160**, 685-697 (2003).

287. Dekker, J. Two ways to fold the genome during the cell cycle: insights obtained with chromosome conformation capture. *Epigenetics Chromatin* **7**, 25 (2014).

288. Ambrosio, S. *et al.* Cell cycle-dependent resolution of DNA double-strand breaks. *Oncotarget* **7**, 4949-4960 (2016).

289. Orthwein, A. *et al.* A mechanism for the suppression of homologous recombination in G1 cells. *Nature* **528**, 422-426 (2015).

290. Kalocsay, M., Hiller, N.J. & Jentsch, S. Chromosome-wide Rad51 spreading and SUMO-H2A.Z-dependent chromosome fixation in response to a persistent DNA double-strand break. *Mol Cell* **33**, 335-343 (2009).

291. Altmeyer, M. *et al.* Liquid demixing of intrinsically disordered proteins is seeded by poly(ADP-ribose). *Nat Commun* **6**, 8088 (2015).

292. Huynh, K.D. & Lee, J.T. Inheritance of a pre-inactivated paternal X chromosome in early mouse embryos. *Nature* **426**, 857-862 (2003).